Development of natural seabed forms and their interaction with off shore wind farms

Margalit, Jonatan

Publication date:
2017

Document Version
Publisher's PDF, also known as Version of record

Development of natural seabed forms and their interaction with offshore wind farms

PhD Thesis

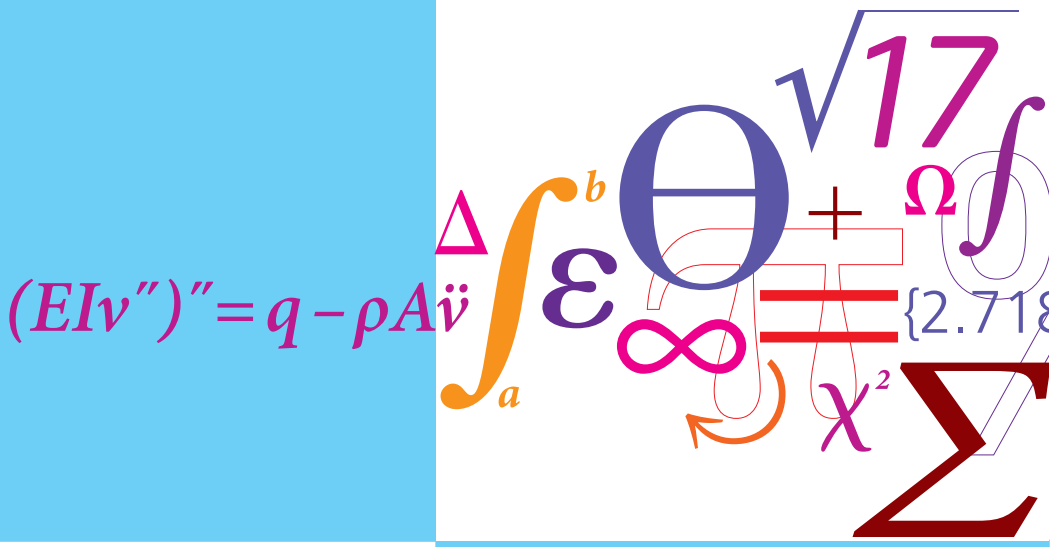

Jonatan Margalit
December 2017

DTU Mechanical Engineering
Department of Mechanical Engineering

Jonatan Margalit

Development of natural seabed forms and their interaction with offshore wind farms

PhD Thesis

Supervisors:
David R. Fuhrman
Jacob Hjelmager Jensen

DTU - Technical University of Denmark, Kgs. Lyngby - 2017

DTU Mechanical Engineering
Section of Fluid Mechanics, Coastal and Maritime Engineering
Technical University of Denmark

Nils Koppels Allé, Bld. 403
DK-2800 Kgs. Lyngby
Denmark
Phone (+45) 4525 1360
Fax (+45) 4588 4325

www.mek.dtu.dk

Abstract

Large, coherent bedforms are often found in the sea, straits and along coasts. The bedforms are generated by sediments, accumulated by a continuous deposition of sand, which is transported by tides, surges and waves. Areas with large bedforms are a favorite target for extraction of sand, gravel and stone for use in construction. Elevated bedforms and reefs are also attractive in the construction of offshore wind farms.

The formation of large, sandy bedforms on the sea floor has been studied in the past using linear stability analyses. These analyses are commonly conducted analytically and therefore require simplifications in the governing equations. This thesis presents a two-dimensional horizontal Matlab model that can simulate the morphodynamics of large-scale bedforms. The model was used to conduct a numerical linear stability analysis, intended to identify the likely emergence of dominant finite sized bedforms, as a function of governing parameters. The model includes separate formulations for bed load, featuring bed load correction due to a sloping bed and modeled helical flow effects as well as suspended load in a pseudo-3D description. Horizontal gradients are computed with spectral accuracy, which proves to be highly efficient for the analysis. The flow velocity, resistance and sediment grain size were varied in a parametric study.

The simulations yielded the emergence of bedforms due to an intrinsic instability of the morphodynamic system. The results support the importance of bed load correction due to bed slope, and also the role that the helical flow has on the characteristics of bedform growth rates, orientation, and in particular its balance with the Coriolis effect, in line with previous analytical studies. Moreover, the results suggest that the inclusion of suspended transport increases, rather than decreases, the unstable growth rate. This outcome stands in contrast to previ-

ous studies utilizing simpler suspended transport descriptions and suggests that suspended transport should be included when looking for quantitative accuracy.

The linear stability analysis gave both quantitative and qualitative predictions, which served as inputs in a morphologic study of large-scale bedforms and helped with the interpretation of its results. The morphologic study shows that the linear growth rate is predicted accurately in the early development stages, but the migration rate is overestimated. One of the theories behind a linear stability analysis is to associate the wavelength of the fastest growing bedform with the final wavelength of bedforms kept in maintenance. This study shows that by using doubly periodic boundaries, resembling far offshore situations, the final bedform can attain a different final form due to non-linear interaction of all the resolved wavelengths within the domain. Comparing the outcome of the bed morphology between a steady current and a tidal flow showed that differences were predominantly quantitative. Offshore wind farms were then added to the morphological study as subgrid elements in order to simulate their interaction with the bedforms. This addition showed that the wind farms could affect the bedforms by increasing their height and slowing their migration rate. However, for large-scale sandbanks in the order of kilometers, the time scale of the changes is very slow and spans over centuries. The morphological development over time scales with the water depth. Thus, a conceptual simulation at very shallow waters indicated that a wind farm turbine could perturb a stable bed and cause the formation of new bedforms developing over timescales comparable to the designed lifespan of offshore wind farms.

Finally, a developer version of MIKE 3 by DHI was modified and used to simulate various cases in 3D. MIKE 3 is a shallow water model that uses σ-coordinates to resolve the water vertically, and the used version includes non-hydrostatic pressure terms. It is crucial to use vertical resolution to simulate bedforms like sandwaves, which are perpendicular to the flow direction and are of shorter wavelengths than sandbanks. Sandwaves are migrating at faster rates than sandbanks and can pose a great nuisance for the structural integrity of offshore structures and cables by migrating and altering the seabed levels up to several meters. The model successfully simulated the full-scale morphological development of sandwaves, the scouring process around a monopile and the interaction between the migrating sandwaves and a monopile. Time limitations did not allow for a thorough analysis of these, but the model provided results that are generally of comparable nature to the literature on the subject and hence look promising for future studies.

Dansk Resumé

I havet, stræder og langs kyster finder man ofte store kohærente bundformer. Bundformerne er opbygget af sedimenter akkumuleret ved en kontinuerlig tilførelse af sand bragt i transport af havstrømninger og bølger. Områder med store bundformer er et yndet mål for indvinding af sand, ral og sten til brug i byggeri. Opgrundede bundformer og rev er tillige attraktive ved anlæggelsen af offshore havvindmølleparker.

Dannelsen af store bundformer på havbunden er over tiden blevet undersøgt ved hjælp af lineære stabilitetsanalyser. Disse analyser udføres ofte analytisk og kræver derfor forenklinger i de styrende ligninger. Denne afhandling præsenterer en todimensional horisontal Matlab-model, som kan simulere morfodynamikken af storskala bundformer. Modellen blev brugt til at foretage en numerisk lineær stabilitetsanalyse, der var beregnet til at identificere fremkomsten af dominerende endelige bundformer, som en funktion af et sæt styrende parametre. Modellen indeholder separate formuleringer for bundtransport, med korrektion på grund af en skrånende bund og modellerede spiralformede strømningseffekter, såvel som suspenderet transport i en pseudo 3D-beskrivelse. Horisontale gradienter beregnes med spektralnøjagtighed, hvilket viser sig at være yderst effektiv til analysen. Strømhastighed, modstands- og sedimentkornstørrelse er blevet varieret i et parametrisk studie. Simulationerne giver fremkomsten af bundformer på grund af en intern ustabilitet i det morfoldynamiske system, og resultaterne understøtter vigtigheden af korrektionen på grund af bundens hældning og også den afgørende rolle, som den spiralformede strøm har på karakteristikaene af bundformernes væksthastigheder, orientering, såvel som balancen med Coriolis-effekten, i overensstemmelse med tidligere analyseresultater. De foreliggende resultater tyder også på, at inddragelse af suspenderet transport øger, snarere end reducerer, den ustabile vækst i modsætning til tidligere undersøgelser, der

udnytter enklere suspenderede transportbeskrivelser. Dette resultat er vigtigt og foreslår, at suspenderet transport skal inddrages, når der søges kvantitativ nøjagtighed.

Den lineære stabilitetsanalyse gav både kvantitative og kvalitative forudsigelser, der tjente som input og sammenligning i en morfologisk undersøgelse af storskala bundformer. Dette har vist, at den lineære væksthastighed forudsiges nogenlunde nøjagtigt i de tidlige udviklingsfaser, men migrationsraten overvurderes. En af teorierne bag en lineær stabilitetsanalyse er at forbinde bølgelængden af den hurtigst voksende bundform med den endelige bølgelængde af fuldtudviklede bundformer, der holdes under vedligeholdelse. Denne undersøgelse har vist, at med dobbelt periodiske randbetingelse, der forestiller situationer langt til havs, kan opnå en anden endelig bølgelængde på grund af ikke-lineær interaktion mellem alle de opløste bølgelængder inden for domænet. Sammenligning af udfaldet af bundmorfologien mellem en stabil strøm og en tidevandsstrøm viste, at forskellene var overvejende kvantitative. Offshore vindmølleparker blev derefter tilføjet til den morfologiske undersøgelse som undergitterelementer for at simulere deres interaktion med bundformerne. Dette viste, at vindmølleparkerne i princippet kunne påvirke bundformerne ved at øge deres højde og sænke deres migrationsrate, men for storskala sandbanker i størrelsesordenen kilometer, er tidsskalaerne for ændringerne meget langsomme og spænder over århundreder. Evolutionstiden skalerer med vanddybden, så en konceptuel simulering ved meget lavt farvande viste, at en vindmølleturbine kunne forstyrre en stabil bund og påvirke dannelsen af bundformer udviklet over tidskalaer, der kan sammenlignes med den designede levetid for havvindmølleparker.

Endelig blev en udviklerversion af MIKE 3 af DHI modificeret og brugt til at simulere forskellige scenarier i 3D. MIKE 3 er en lavvandsmodel, der bruger σ-koordinater til at opløse vandet lodret, og den anvendte version indeholder ikke-hydrostatiske udtryk. Det er afgørende at bruge lodret opløsning til at simulere bundformer som sandbølger, der er vinkelret på strømningsretningen og har kortere bølgelængder end sandbanker. Sandbølger vandrer hurtigere end sandbanker og kan påføre store gener for den strukturelle integritet af marine konstruktioner og kabler ved at vandre og ændre havbunden op til flere meter. Modellen simulerede med succes den morfologiske udvikling af sandbølger, erosionsprocessen omkring en monopæl og samspillet mellem de vandrende sandbølger og en monopæl, i fuld skala. Tidsbegrænsninger tillod ikke en grundig analyse af disse, men modellen gav resultater, som generelt er af sammenlignelig karakter til litteraturen om emnet, og ser derfor lovende ud til fremtidige studier.

Preface

This thesis is submitted in partial fulfillment of the requirements for a Ph.D. degree from the Technical University of Denmark. The work was conducted at the Department of Mechanical Engineering, Section of Fluid Mechanics, Coastal and Maritime Engineering, Technical University of Denmark. It lays out the research conducted in the period July 2014 December 2017, on large-scale bedforms and their interaction with offshore wind farms. The Ph.D. study has been part of ForskEL project 2013-1-68012: Management of seabed and wind farm interaction, which was managed by Anders Wedel Nielsen and funded by Energinet.dk, whom I wish to acknowledge for the financial support.

I would like to send a special thanks to my supervisors David R. Fuhrman and Jacob Hjelmager Jensen who initiated the project and provided solid support and shared their knowledge on the subject. Another special thanks is directed towards Kasper Kærgaard and Danish Hydraulic Institute (DHI) for their great support and access to the commercial software MIKE3/21, and for allowing me to spend two months in their office at Gold Coast, Australia, and six months in the main headquarters at Hørsholm, Denmark. I would also like to thank my colleagues at DTU for being part of a positive environment providing moral support when needed. In this regard a thanks should also be sent to Joe Rogan and the many interesting guests on his podcast, for a great enrichment during many tedious moments. Lastly, I want to thank my girlfriend Anna and dog Max for the great support on the home front.

Jonatan Margalit
Kgs. Lyngby
December 2017

List of Symbols

A	Perturbation amplitude
C'_D	Skin friction drag coefficient
C_D	Total frcition drag coefficient
C_M	Monopile drag coefficient
C_{D0}	Unperturbed bed resistance drag coefficient
D^*	Dimensionless grain size
D_M	Monopile diameter
E	Entrainment rate
E_v	Stokes number
Fr	Froude number
G	Bed load slope correction constant
H	Still water depth
I	Energy gradient
$L_{As/n}$	Suspended load adaption length in s/n
N	Grid points per bedform
P	Probability
R_s	Streamline curvature radius

Re	Reynolds number
Re_d	Grain Reynolds number
Ro	Rossby number
$\boldsymbol{S}$	Source vector
$S_{x/y}$	Source component in x/y
T_A	Suspended load adaption time
$\tilde{U}$	Velocity perturbation
U_0	Unperturbed mean velocity
U_c	Current velocity
U_w	Tidal velocity amplitude
Z	Rouse parameter
Z_g	Modified Rouse parameter
$\hat{S}$	Non-dimensional resistance parameter
a	Calibration constant
a_r	Ripples calibration coefficient
a_{ref}	Suspended load reference level
b	Calibration constant
c	Volumetric sediment concentration in equilibrium
$\bar{c}$	Mean volumetric sediment concentration
c_b	Suspended load reference concentration
c_e	Volumetric sediment concentration
$\bar{c}_e$	Mean volumetric sediment concentration in equilibrium
d_{50}	Mean grain diameter
d_{90}	Grain diameter of the 90th percentile
f_A	Morphological amplification factor
f_c	Coriolis frequency
g	Gravitational acceleration

h	Water depth
$\tilde{h}$	Depth perturbation
h_0	Unperturbed water depth
h_b	Bed elevation
$\tilde{h}_b$	Bed level perturbation
i_s	Helical flow intensity
k_N	Nikuradse equivalent roughness
k_s	Total roughness parameter
k_x	Wavenumber in x
k_y	Wavenumber in y
m	Integer
n	Horizontal streamline normal coordinate
$n_{x/y}$	Grid points in x/y
p_s/n	Velocity unit profile in s/n
$\boldsymbol{q}_b$	Bed load vector
$\boldsymbol{q}_s$	Suspended load vector
$q_{bx/y/s/n}$	Bed load component in $x/y/s/n$
q_{se}	Suspended load in equilibrium
$q_{sx/y/s/n}$	Suspended load component in $x/y/s/n$
s	Horizontal streamline coordinate
t	Time
u	Velocity component in x
$\bar{u}$	Depth-averaged velocity component in x
$\boldsymbol{u}$	Depth-averaged velocity vector
u'_f	Skin friction component of friction velocity
$\boldsymbol{u}_b$	Near bed velocity vector
u_f	Friction velocity

$\boldsymbol{v}_p$	Sediment particle velocity vector
$\boldsymbol{u}_r$	Relative velocity vector
u_s	Velocity component in s
v	Velocity component in y
$\bar{v}$	Depth-averaged velocity component in y
v_n	Velocity component in n
w	Velocity component in z
w_s	Sediment fall velocity
x	Horizontal Cartesian coordinate
y	Horizontal Cartesian coordinate
z	Vertical Cartesian coordinate
z_0''	Form drag roughness height
z_0'	Skin friction roughness height
z_0	Total roughness height
ΔM	Monopile spacing
Δx	Grid spacing in x
Δy	Grid spacing in y
Δ_r	Ripple height
Ω	Growth rate
Ω^*	Non-dimensional growth rate
$\Phi_{0/t/s/n}$	Concentration unit profiles
$\boldsymbol{\Phi}_{b0}$	Non-dimensional bed load rate
$\boldsymbol{\Phi}_{s0}$	Non-dimensional suspended load rate
α	Bed slope calibration coefficient
α_s	Helical flow adaption length calibration constant
β	Helical flow resistance parameter
δ	Boundary layer thickness

δ_s	Angle between mean flow and bed shear stress
ε_p	Bed porosity
η	Surface elevation
κ	Von Karman constant
λ_r	Ripple length
λ_s	Helical flow adaption length
μ_d	Dynamic coefficient of motion of sediment
ν	Kinematic viscosity
ν_T	Eddy viscosity
ω_b	Migration rate
ϕ	Phase
ρ	Water density
ϱ	Relative density of sand
σ	Vertical normalized coordinate
σ_2	Tidal frequency
$\boldsymbol{\tau}_b$	Bed shear stress vector
$\tau_{bx/y}$	Bed shear stress component in x/y
θ	Shields parameter
θ'	Skin friction component of Shields parameter
θ_c	Shields parameter value at incipient particle motion
ζ	Vertical normalized coordinate
ζ_0	Vertical normalized coordinate no-slip level

Contents

Chapter 1

Introduction

The increased activity in offshore wind farms construction has driven the industry to require a better understanding of the surrounding seabed morphodynamics. In this chapter, a brief overview of the historical development of the offshore wind market is laid out, followed by a presentation of some of the challenges and questions that this thesis addresses.

1.1 Background and motivation

After roughly a century of relying heavily on fossil fuels, countries around the world have started to push for policies that encourage energy production from renewable sources, mainly in the form of solar and wind power. For the past 15 years, wind power installations in Europe increased steadily at a compound annual growth rate of 9%. The European Union (EU) has set a target that 20% of the total consumed energy within the EU is to be generated by renewable sources by 2020, and 27% by 2030. As of 2014 the actual energy consumed from renewable resources was 15.3%, EUC (2017). In Denmark, 39% of the consumed electricity in 2014 came from wind power, in contrast to only 2% in 1990. Furthermore, Denmark has set a target of increasing that number to at least 50% by 2020. Denmark, which is located in a region with year-round favorable wind conditions for electric power generation, was able to achieve this

increase due to large investments in wind installations at an early stage. For additional information see Energinet.dk (2016).

The wind power market was initially based exclusively on onshore installations. Then, in the 1990s companies started to experiment and develop coastal and offshore wind installations. Nowadays these installations have matured and commercialized such that they accounted for 24% of the European wind energy market in 2015. Within the European offshore wind market, the North Sea accounted for nearly 70% of the installed offshore wind power capacity in 2015, EWEA (2015). Among the reasons for the increase in offshore locations are the favorable wind conditions that are found offshore compared to onshore. Additionally, logistics and regulations allow for much larger wind installations in the offshore environment.

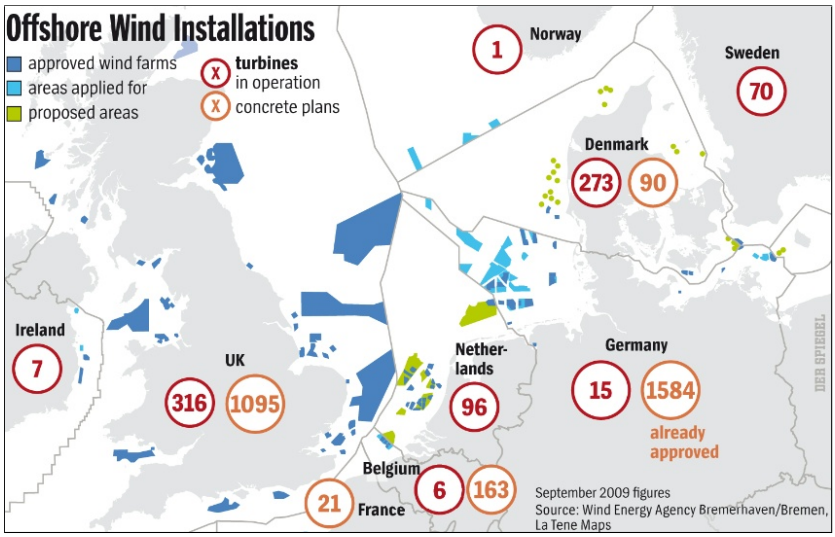

Figure 1.1: Offshore wind installations in the Baltic, Irish and North Seas. Credit: Der Spiegel.

Fig. 1.1 shows locations of offshore wind installations in the Baltic, the Irish and the North seas. These locations have moved further offshore over the years, such that at the end of 2015, the average water depth of grid-connected wind farms was 27.1 m and the average distance to shore was 43.3 km. In the future, these numbers are expected to increase, as well as the size and capacity of each farm. Currently, more than 95% of the wind turbines are mounted on cylindrical foundations called monopiles, for which diameters are typically 4-8 m. Monopiles are considered cost-effective for depths up to 30 m, so it is expected

that other forms of foundations (e.g., jacket) will increase their market share as the farms move into deeper areas, EWEA (2015).

The water depth at the location largely influences the cost of constructing an offshore wind farm. As a result, developers seek shallow regions for these wind farms. In the North Sea, besides near-shore locations, shallow regions are mainly located where large sandbanks are present. These sandbanks are morphodynamically active, and therefore it is important to locate sites that are expected to remain stable within the operation period of the wind farm. These sandbanks are also a source of sand for use in construction.

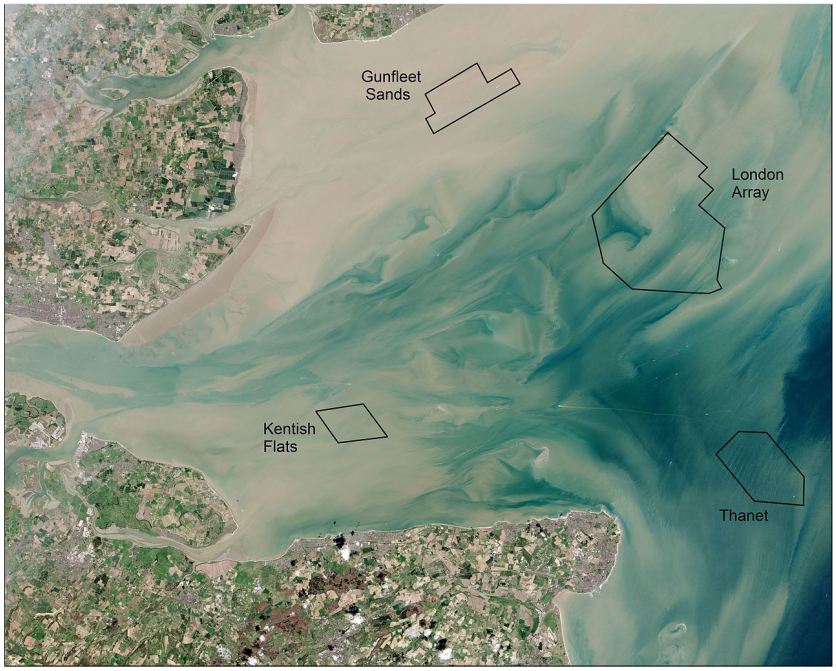

Figure 1.2: Thames estuary and marked location of offshore wind farms.

Fig. 1.2 shows an example of the morphodynamic activity of the sandbanks at the Thames estuary in South-East England. The locations of four offshore wind farms are marked within the black polygons. The seabed in this region is visibly affected by the water motion. First and foremost, this poses a risk for the structural integrity of the wind turbines due to scour around the monopiles. Another problem occurs when migrating large-scale sandwaves encounter the wind farm, as they can alter the seabed elevation by several meters. Consequently, this poses a challenge from the structural point of view and can become a particular

nuisance for the power cables laid on the seabed.

In a broader perspective, construction of large wind farms alters the hydrographic conditions. The turbines alter wind conditions, thus affecting the driving forces of both waves and currents (in the lee side of the wind turbines). Furthermore, the foundations may impose an effect on current and wave conditions. Roughly speaking, the mosaic of foundations increases the flow resistance and causes blockage and scattering of the waves. These effects produce changes in the local natural hydrographic conditions, and thereby shift the natural equilibrium of the system and its morphology. The stability of bedforms, in their natural (original) and imposed (new) states, as well as the time scale and transitional stages between these two equilibrium states, are of major importance and interest to investors. An example of the influence of wind farms on the seabed can be seen in Fig. 1.3, which shows the Thanet wind farm, located in the Thames estuary. The pictures show that each monopile generates a plume of suspended sediments, which are transported away by the currents.

The morphology of bedforms consists of various features, i.e., their shape, mobility and surface characteristics (grain size and smaller superimposed bedforms). Bedforms vary in morphology, and very different mechanisms drive their creation and maintenance. These processes depend on the local wave-current conditions, namely, the flow, wave height and wave periods, and of equal importance, their directions and scattering. Sedimentary conditions also come into play, especially for the mobility of the bedforms. Additionally, locality plays a role as well, mainly in the form of the nearby boundary conditions (land) and the magnitude of, e.g. the Coriolis force. The construction of offshore wind farms requires huge investments, so bedform stability is a decisive factor in the selection of suitable sites and for the implementation of projects. We know that many of these bedforms are very stable, by comparing records and old nautical charts with recent measurements of bathymetry. However, we know less about their morphological DNA and sensitivity to changes in the hydrographic climate.

1.2 Objective and methodology

This thesis seeks to understand the stability of various types of large-scale bedforms using stability analysis. These analyses provide a deeper understanding of the livelihood of bedforms, i.e., whether they are created due to an instability of the system governed by its intrinsic parameters, or due to other (imposed) mechanisms. Furthermore, the thesis investigates and describes the various processes that are important for the creation and maintenance of bedforms, i.e. their morphological evolution from the moment they emerge and until they

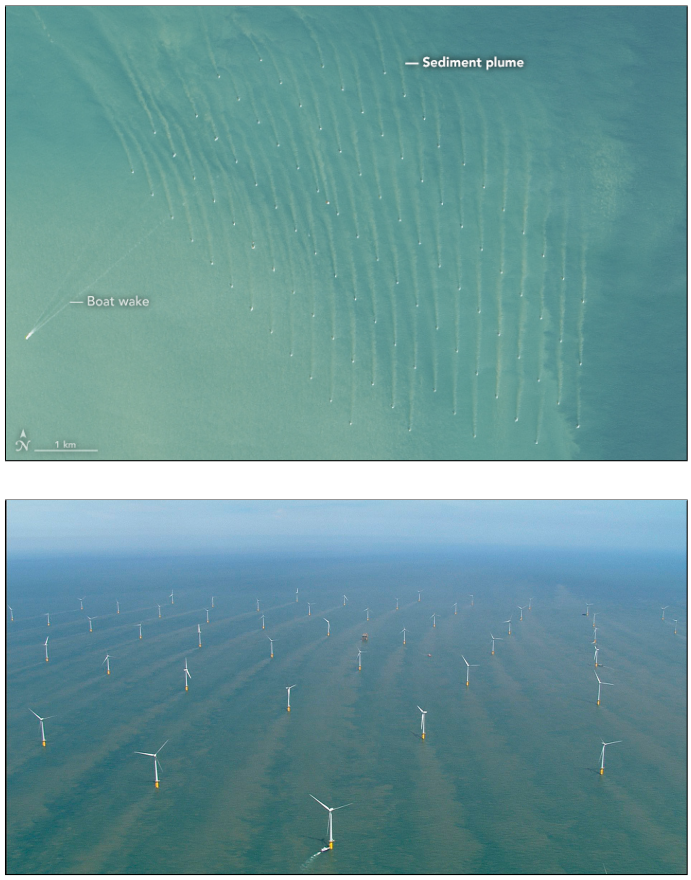

Figure 1.3: Thanet wind farm generating suspended sediment plumes. Credit: Top NASA (2015), bottom Vattenfall (b).

reach a stable stage. Lastly, this thesis examines whether sediment transport processes are strengthened or weakened by the construction of large offshore wind farms, that is, whether transport patterns and deposition/erosion of sediments change the physical characteristics of bedforms and over what time scales the changes take place. Other factors such as climate changes are not directly concerned.

The flow and transport fields were calculated using a two-dimensional depth-averaged model developed in the commercial software Matlab for this purpose. This model is used to conduct the linear stability analysis as well as the morphological study on the large-scale seabed forms resembling sandbanks. The offshore wind farm turbines are modeled as subgrid structures to investigate the

large-scale effect on the bedforms. For three-dimensional simulations, a modification of DHIs commercial software MIKE 3 was used to simulate full-scale sandwave morphodynamics as well as scour around a monopile using a body fitted grid.

1.3 Thesis outline

Chapter 2 introduces the characteristics of various types of bedforms and reviews some of the relevant literature on the subject.

Chapter 3 presents the governing equations of the 2D horizontal (2DH) model coded in Matlab. The description goes into the hydrodynamics, sediment transport and briefly mentions the numerical model aspects.

Chapter 4 presents a validation of the 2DH model with measurements from a backfilling trench experiment as well as a flume experiment, where alternating bars were formed.

Chapter 5 establishes the mathematical background and presents a linear stability analysis conducted with the 2DH model on large-scale bedforms. Many cases were simulated to provide an insight into the effects of various parameters.

Chapter 6 builds on the results of the linear stability analysis and investigates the morphological, nonlinear evolution of the large-scale bedforms while considering different scenarios including interaction with modeled offshore wind farms.

Chapter 7 shows simulation results where a modified version of MIKE 3 is used to explore the three-dimensional modeling possibilities with regards to sandwaves morphology and monopile interaction.

Chapter 8 presents the conclusions of the thesis and includes recommendations for further work.

Chapter 2

Bedform nomenclature and review

This chapter goes through the basic concepts of sediment transport and the physics of sandy bedforms including a review of the available literature on the subject. The chapter is intended to be self-explanatory, leaving the mathematics for following chapters.

2.1 Sediment transport

Sediment transport is a field studying the movement of solid particles due to interaction with fluid motions. Among many applications, it is used to study the bed morphodynamics of rivers, coastal and offshore processes, with a particular interest in the interaction with marine and maritime human-related activities. Within the scope of this thesis, the considered sediment material is non-cohesive sand, which covers grain diameters in the range 0.06 – 2 mm. Two transport modes of the sediments are defined:

1. **Bed load**, describes the transport of sediments which remain in contact with the bed by rolling, sliding or jumping.

2. **Suspended load**, describes the transport of sediments which are not in continuous contact with the bed as a result of fluid turbulence.

The mechanisms behind sediment transport are quite complicated and not all fully understood. The established theory relates the shear stress exerted by the fluid flow on the bed, to individual particles becoming mobile once a threshold of motion is passed. The threshold is reached once the driving force on a particle overcomes the stabilizing force due to gravity. Many of the underlying equations are based on empirics and statistics, thus model calibration is a common practice and accuracy may vary by high factors. The simplest sediment transport models directly relate the mean flow velocity to a transported quantity, while more advanced models account for the transport modes separately and attempt to break down the fluid physics and obtain the bed load and the distribution of suspended sediments in the water column.

Observations have shown that sandy beds tend to produce coherent bedforms, which may emerge when a plane bed is exposed to a fluid flow. This phenomenon has been addressed extensively with stability analyses that attempt to predict and explain the parameters that govern the formation and maintenance of bedforms.

2.2 Bedform classification

The following describes the most common bed features that are relevant for the numerical modeling and the characteristics used to distinguish between bedform types.

2.2.1 Ripples

Ripples are small bedforms of sizes that are on the scale of centimeters. Two sub-categories (visualized in Fig. 2.1) are typically used to classify ripples: 1) current- and 2) wave generated ripples. The first type is forming on beds with fine sediments at flow speed slightly above the threshold of motion. They commonly emerge in natural streams and tidal dominated flows, as three-dimensional asymmetrical features, with crest-lines perpendicular to the current direction and downstream migration. The second type emerge due to an oscillatory flow such as under waves. Also here the crest-lines are perpendicular to the flow direction, but these ripples are generally symmetrical or changing polarity with the water motion.

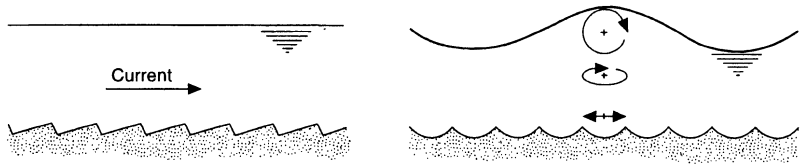

Figure 2.1: Cross-section of ripples. Left: current generated ripples, Right: wave generated ripples. Credit: Soulsby (1997).

Ripples add resistance to the flow and particularly in waves increase the amount of suspended sediments. The size of ripples is independent of the water depth but correlates with the sediment grain diameters. An empirical estimation of their height and wavelength can be found in Soulsby (1997); Grant and Madsen (1982); Nielsen (1979), for both types.

2.2.2 Dunes and sandwaves

Dunes are bedforms of sizes that are on the scale of meters. They are usually found under unidirectional flows such as in rivers and in some cases in sea regions with strong currents, e.g. flood and ebb tides (dunes in the sea are generally referred to as sandwaves). River dunes usually emerge with courser sediments and at flow velocities higher than those generating ripples. The cross-sectional shape of a dune is roughly triangular with a moderately sloped upstream (stoss) side and a steep downstream (lee) side approximately equal to the angle of repose of the sand, see Fig. 2.2. Dunes are slowly migrating in the current direction as the sediment particles forming the dunes are transported up the stoss side by the flow, and past the crest to eventually deposit in the trough. The boundary layer that forms on the stoss side, separates at the crest and reattaches at the lower stoss side of the leading dune, whereby a vortex is formed over the dune front in the trough. At an intermediate flow stage, dunes can have ripples superimposed. If the current speed is continuously increased, more sediments go into suspension instead of being deposited in the trough, which leads to elongation and flattening of the dunes, eventually leading to a plane bed with sediments transported intensely in a so-called sheet flow.

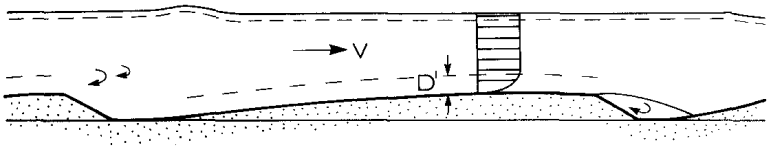

Figure 2.2: Cross-section of dunes. Credit: Fredsøe and Deigaard (1992).

In spite of the difference in environments, much of the theory of dunes has been carried over to sandwaves, as they share similar characteristics. Even in nearly symmetrical unidirectional tides, sandwaves may be asymmetrically skewed towards the mean flow direction like dunes, and have crest-lines perpendicular to the mean current direction. Based on empirical data, Stride (1982) states that dune lengths in rivers is in the order 4–8 times the water depth, while sandwaves shaped by a unidirectional tidal current are of lengths in the broader range of 2–18 times the water depth. In both cases the dune/sandwave height (trough to crest) is up to a third of the water depth. Large sand waves are also likely to have smaller bedforms superimposed (e.g. megaripples).

A good reference for the estimation of dune/sandwave height and length as well as migration rate can be found in Fredsøe and Deigaard (1992) and van Rijn (1984b), which relate these quantities to the flow depth and bed shear stress.

2.2.3 Sand bars/banks/ridges (Large-scale bedforms)

This category includes the largest coherent bedforms occurring naturally both in rivers (sandbars) and in the sea environment (sandbanks and ridges). In rivers, sandbars usually appear when the river width becomes much larger than the depth. Over time, this may lead to river meandering or braiding as the analysis of Fredsøe (1978) suggests, and discussed further in the validation in Chapter 4. In the sea environment, sandbanks are sandy bedforms in shallow seas with wavelength in the order of kilometers and wave height in the order of tens of meters. That is, the wavelengths are several orders of magnitude longer than the depth, and the wave height is in the order of the depth. The orientation of the crest-lines is oblique to the mean current direction. Sandbanks are formed by sea currents, and are considered very stable, with a barely noticeable migration speed. The slopes of sand banks are gentle so boundary layer separation is not an issue, which is among the reasons they can be modeled in a depth-averaged model, as discussed later.

The stable nature of sandbanks has directed most of the engineering related research to look at the more active sandwaves and ripples. However, it is still justified to do sandbank studies when the problem is of a large-scale nature. For example, in cases where big amounts of sand are extracted over a large area, or as in the present case, the overall effect caused by the mosaic of turbines forming a wind farm.

2.3 Bedform instability mechanisms

The bedform instability mechanism is explained in Fig. 2.3, which depicts a bedform (denoted by h_b) exposed to a flow from left to right and as a result, sediments are transported (denoted by q) in the direction of the flow. The key to understanding the instability lies in the crest of the bedform. Simply put, if the transport towards the crest is larger than the transport away from the crest, the bedform will grow, while it will decay if the opposite occurs. In case the two transports are in equilibrium, the bedform remains stable and could potentially migrate. In other words, the phase difference between the bedform and the sediment transport field expresses whether the bedform grows, decays or remains stable. Engelund (1970) and Fredsøe (1974) are among the pioneering work that laid the basis for the modern physical understanding of the processes related to the stability of sandy beds.

Figure 2.3: Instability mechanism of a bedform.

The flow over low amplitude bedforms is usually of low sub-critical Froude number values, which means that the above surface would be nearly flat and approximately 180° out of phase with the bed. Hence, the flow will be converging (with favorable pressure gradient) in the upstream side of the bedform and diverging (with adverse pressure gradient) in the downstream side. An adverse pressure gradient can lead to boundary layer separation as described previously for the dunes. As mentioned in the beginning of the chapter, the sediment transport is usually modeled from the shear stress that the fluid exerts on the bed. Thus, the bed shear stress would theoretically be higher on the upstream side due to flow acceleration and lower on the downstream side due to deceleration. This shear

stress difference and a possible pressure gradient due to bed curvature generates a phase lag between the bed shear stress and the bedform, which would lead to growth. Without any other mechanisms, this would make the bedforms with the shortest lengths (read steepest bedforms), grow fastest. However, this is countered (for bed load) by gravity which naturally enhances downstream sediment transport and retards upstream transport, eventually leading to a stable bedform in equilibrium. Some sediments may also come into suspension as the flow accelerates towards the crest. These sediments will need time to settle back on the bed, and hence increase erosion, i.e. decay the bedform.

The description above was applied for a bedform assumed to be uniform in the lateral direction. In case the bedform has variations in three-dimensional space (in reality all bedforms would come under this category), the flow pattern could differ in that the streamlines would curve around the crest and hence the upstream acceleration would be reduced or not occur. In this case other three-dimensional flow phenomena occur which would drive sediments towards the crest, while gravity drives the sediment transport laterally downslope. However, while these considerations complicate the physics, the main principle regarding the balance of sediments going towards and away from the crest is still valid.

Regarding the oblique orientation of sandbanks, Zimmerman (1981) explained this by circulating residual flow cells around the crests, as a result of a bed slope friction torque and Coriolis torque. When the flow crosses the sandbank, it is accelerated upstream and decelerated downstream, as mentioned previously. This generates a net transport of sediments from troughs to crests in both the flood and ebb tide, which results in growth of the sandbank. In the northern hemisphere, a sandbank inclined counter-clockwise to the mean flow direction, will experience both friction and Coriolis torques rotating clockwise on the upstream side and counter-clockwise downstream, whereby the sandbank growth is enhanced. On the other hand, the friction torque on a sandbank inclined clockwise in the same location, would counter the Coriolis torque, and hence suppress growth. This counter-reaction is the reason sandbanks are usually oriented counter-clockwise to the mean flow direction in the northern hemisphere, while the opposite applies in the southern hemisphere.

Some of the mathematical principles of the instabilities discussed above, are described in Chapter 5.

2.4 Review

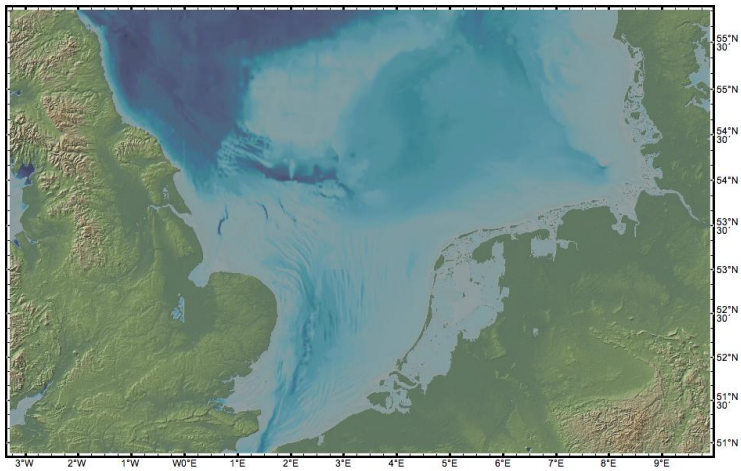

Figure 2.4: Southern part of the North Sea.

This thesis focuses on the study of large-scale bedforms in the sea. Consider Fig. 2.4, which shows the southern part of the North Sea confined by the surrounding land mass. The brighter areas in the sea are relatively shallow and contain large sandy bed features, which are typically categorized as sandwaves and sandbank. Some of these bedforms have repetitive patterns and seem to be actively interacting with the sea flows over a time scale measured in years. Field studies indicate that these large-scale bedforms are primarily morphologically active due to tidal currents and during storms. Sandwaves have shown a tendency to migrate at a rate of several meters per year, while sandbanks appear to be more stable with much lower migration rates. These kinds of bedforms can be observed in seas all over the world, and have therefore given rise to extensive studies. Human-related activity in the offshore environment has increased steadily over the years; hence, from an engineering point of view, it is important to understand the morphological nature of the seabed. The question of how the bedforms emerged in the first place has been the subject of various theories. Research indicates that, although some bedforms may be relics from another geological period, and some formed due to restraining boundary conditions (e.g. the land), there are also bed forms that can be explained as a pure instability phenomena of the water-bed system, as described in the previous section.

In the past most research was conducted by means of a linear or weakly nonlinear stability analysis, which helped understanding the early stages of bedform generation and some of the physics. For a complete description of bedform

evolution a fully nonlinear morphological model is necessary. To date, the computational power is still not sufficient for a detailed three-dimensional modeling of large-scale bedform morphology. The traditional modeling methodologies approaching the subject have therefore been: 1) a 2D horizontal (2DH) (depth-averaged) shallow water model, and 2) a 2D vertical (2DV) model which assumes uniformity in the lateral direction, thus solving for the flow in the stream-wise and vertical directions. Large-scale bedforms will often have smaller bedforms superimposed. In both modeling techniques the smaller scale bedforms would likely be incorporated as an additional flow resistance on the bed (see e.g. Engelund and Hansen (1967)), rather than resolving each of them.

Huthnance (1982) is considered to be the first to show that a linear perturbation analysis of the depth-averaged shallow water equations, 2DH, could reasonably predict sandbank characteristics. Huthnance included the Coriolis effect at a North Sea latitude and was able to determine a dominate wavelength and bedform orientation towards the mean flow direction, which was modeled as a unidirectional tide. because the timescale of variations in the flow is much smaller than the bed evolution, the growth rate was calculated based on the averaged tidal cycle flow, a practice that has been followed in many subsequent studies. The sediment transport was modeled using a total load equation with gravity correction (such that sediment is transported easier downslope and harder upslope). Thereby, Huthnance predicted the sandbanks, with crest-lines oriented counter-clockwise relative to the mean current direction, due to the Coriolis effect.

de Vriend (1986) did a stability analysis in 2DH for both pure current and combined waves-plus-current environments and found that without bottom slope effects the system is completely unstable for all modes (wavenumber combinations). The inclusion of bottom slope effects means that vertical near-bed accelerations are present and hence the flow should truly be modeled in three dimensions. These near-bed accelerations were studied further by de Vriend (1987), in an attempt to determine their effect on the morphodynamics, and asses their incorporation in the morphological model. Helical flow effects (also mentioned as secondary flow in literature, i.e. flow deviating from the primary flow direction) could be modeled separately, to account for the flow variations throughout the water column within a 2DH model. de Vriend (1990) subsequently made an extensive study where he, in addition to bed load, included a separate formulation for suspended load and investigated the response in both unidirectional and elliptical tide environments combined with currents as well as waves. de Vriend (1990) found that elliptical tides and suspended load tended to suppress the growth, especially for shorter bedform wavelengths. Additionally, he showed that in addition to Coriolis effects, other effects such as wind, density gradients and wave streaming could influence the orientation of the bed forms, as these make the transport direction deviate from the mean current direction.

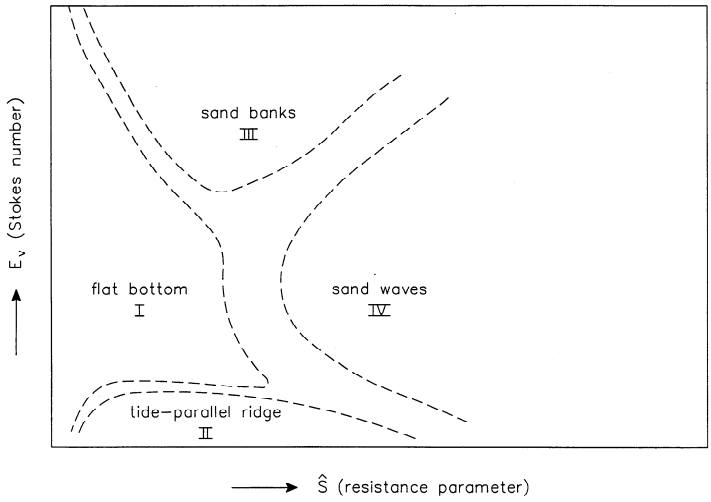

Figure 2.5: Characteristic bed forms predicted by the three-dimensional shallow water model as a function of $\hat{S}$ and E_v. Credit: Hulscher (1996).

Hulscher et al. (1993) expanded Huthnance's model with the option of allowing elliptical tides and helical flow effects on the sediment transport. This study showed that an elliptic tide can suppress the growth of bed forms, in some cases only the longest wavelengths and in other cases all wavelengths, depending on a critical parameter setting. The inclusion of the helical flow effects conceptually yielded the growth of bedforms categorized as sandwaves due to their orientation and wavelength. This work was extended by de Swart and Hulscher (1995) and applied for coastal seas, which reinforced the previous findings. Hulscher (1996) used a three-dimensional shallow water model, i.e. with vertical variations of the velocities, for a linear stability analysis. The current was induced by a unidirectional tide and the shear stress at the bottom boundary was given by a partial slip formulation

$$\left.\frac{E_v}{2}\frac{\partial \boldsymbol{u}}{\partial z}\right|_{bottom} = \hat{S}\boldsymbol{u} \tag{2.1}$$

where $\boldsymbol{u}$ is the horizontal velocity vector, E_v is the Stokes number, which relates the part of the water column where viscous effects influence the tidal motion significantly and $\hat{S}$ is a non-dimensional resistance parameter. The bed shear stress was used to estimate the bed load including slope effects. The model yielded four bedform regimes as a function of E_v and $\hat{S}$, depicted in Fig. 2.5: I) flat bed, II) tide-parallel ridges, III) sandbanks and IV) sandwaves. The sandbanks appeared at high values of E_v, i.e. fully developed boundary layer

over the water column, and low-intermediate values of $\hat{S}$. Their wavelengths matched the theory and was in the order of kilometers. The Coriolis effect (through so-called Ekman spiraling) influenced the orientation of the sandbank crest-lines to be in the range 30°–60° counter-clockwise to the mean current direction. On the other hand, the sandwaves emerged at intermediate values of E_v and high $\hat{S}$ values. Their wavelengths in the order of hundreds of meters and the crest-lines were nearly perpendicular to the mean flow direction. Sandwaves appeared to be generated by large veering of the horizontal velocities from the mean current direction, an effect attributed to the higher resistance and shorter bedform wavelengths, which enhanced advective effects. Essentially for both types of large-scale bedforms the growth was driven by residual recirculation cells from bottom to surface, yielding a net sediment transport from troughs to crests during both flood and ebb tides. The factor determining whether a sandbank or sandwave was to emerge, was the bed slope effect on the transport. When this effect was countered by the tide-topography interaction among others, steeper slopes could be established (i.e. shorter wavelengths), while an increasing effect of the bed slope pushed towards longer wavelength, whereby Coriolis effects become more significant. This work by Hulscher (1996) was the first to propose this mechanism leading to the generation of sandwaves in a tidal environment. Hulscher and van den Brink (2001) related E_v and $\hat{S}$ to a parabolic eddy viscosity and a friction height in order to estimate realistic values. The model was then tested for data of the southern part of the North Sea, and it showed a partial ability to predict the observed type of bedforms by size and orientation. This work was extended by Van Der Veen et al. (2006) to include grain size dependency on the formation of sandwaves and in Van Der Veen and Hulscher (2009) a parametrization of the eddy viscosity was used to improve the prediction of sandbanks in the North Sea. Further studies on sand waves in depth-averaged models were conducted by Carbajal et al. (2005), which showed that a Kelvin wave diffracted in a limiting geometry can lead to the formation of sandwaves.

The work of Stride (1982) and later Fredsøe and Deigaard (1992) mention no mechanism for sandwave generation, but hypothesize that sandwaves in the sea share many similarities with dunes, with differences caused mainly by tidal flow reversal and surface waves. Fredsøe and Deigaard (1992) apply the dune theory and obtain reasonable predictions of sandwave heights and lengths, and show the suppressing effects of surface waves on these bedforms, especially in shallow waters, due to increased near-bed oscillatory motion and suspended sediment.

Considering the above, it is not a surprise that it is common practice to use 2DH models to simulate length-scales associated with sandbanks, while sandwaves are modeled in 2DV models due to the importance of resolving vertical variations in the water column. Niemann (2003) used the 2DV model developed by Tjerry (1995) to simulate dune morphology in a unidirectional steady current, tidal

current as well as the two combined, and obtained results that are very much in line with the work of Fredsøe and Deigaard (1992). Although it is outside the scope of this thesis, it is also worth mentioning Komarova and Hulscher (2000); Gerkema (2000); Németh et al. (2002); Besio et al. (2003, 2006); Németh et al. (2006); Meer et al. (2007); Roos et al. (2008); van den Berg et al. (2012); Borsje et al. (2013, 2014) who facilitated the 2DV approach to conduct stability analyses to predict the early stages of sandwaves migration and final amplitude estimation, and parametrization to study the importance of various aspects such as turbulence formulation, grain size and sorting, and the role of suspended load.

The work of Nelson (1990) inspired Madsen (2001) to use a finite volume 2DH model to do a linear stability analysis and morphological study of large-scale bedforms, in steady current as well as in wave-current environment. The model included separate bed load and suspended load modeling, as well as helical flow effects. The approach of Madsen (2001) to morphological modeling is adopted in this thesis to a large extent.

In some literature pseudo-3D models are used and include both bed and suspended loads. They focus on more specific studies such as Walgreen et al. (2002), that investigated the development of shoreface-connected bed forms in tidal and storm conditions. Roos (2003) studied initial responses to arbitrary topographies with small amplitudes, and Besio et al. (2008) attempted to improve the quantitative prediction of a model based on Hulscher (1996) and, in addition, study nonlinear bedform behavior. Blondeaux and Vittori (2005a,b) presented a three-dimensional model with Boussinesq assumption for the turbulent Reynold stresses and include eddy viscosity modeling, bed load and suspended load with effects of wind waves. The model has shown that for a certain set of parameters, a sand pit in a tidal environment can trigger the formation of large-scale bedforms. Lastly, Blondeaux and Vittori (2011) made a comparison between three-dimensional and shallow water models in an attempt to quantify the parameters that determine which model is necessary to obtain reliable predictions. Blondeaux and Vittori (2011) suggested using shallow water models for cases where the depth-to-bedform wavelength ratio is less than 0.05, while three-dimensional models should be preferred in strong tides, coarser sediment grain diameters and small water depths.

Many studies of local bed effects from flow around monopiles can be found in literature, but information regarding the large-scale effects is scarce. To the authors knowledge, van der Veen et al. (2007) is the only to address the large-scale effects by using Hulscher's (1996) model to conduct a linear stability analysis in a domain with a wind farm in the center. The wind farm was simulated as added flow resistance, and different parameters where varied to investigate the extent to which the wind farm affected the surrounding area.

Chapter 3

Governing equations: Depth-averaged model

3.1 Introductory remarks

As discussed in the introduction, this thesis deals with large-scale bedforms and their interaction with offshore wind farms (which span over several kilometers). Hence, variations in both horizontal dimensions have to be resolved and therefore a 2DV model would not suffice. Based on the matters presented in the previous chapter, it was decided to address the topic with a depth-averaged model (2DH). The use of such a model would allow the modeling of sandbanks, and it was expected that inclusion of helical flow, as demonstrated by Hulscher et al. (1993), would allow a limited modeling of sandwaves. Naturally, a depth-averaged model is unable to capture all the physical processes of a fully developed sandwave due to lack of vertical resolution. However, it could serve as the first step in a comparative study of the overall effects with regards to wind farm interaction.

Three MSc projects Fianchisti (2015); Hansen (2015); Sørensen (2016) investigated the matter using the depth-averaged model MIKE 21 by DHI (2013a,b), with varying degree of success. MIKE 21 is oriented towards commercial uses, so while being extremely capable, it needed several modifications in order to

be adapted to the academic study of this thesis. Therefore, it was decided to develop a depth-averaged model (with sediment transport and bed morphology) from scratch. After first considering the open source CFD code OpenFOAM for the purpose, the final choice landed on the programming language Matlab by Mathworks, due to its coding flexibility.

A description of the model equations is presented in the following. As will be seen, the developed model is of comparable complexity to modern commercial codes, bearing similarity in many features to MIKE 21.

3.2 Hydrodynamics

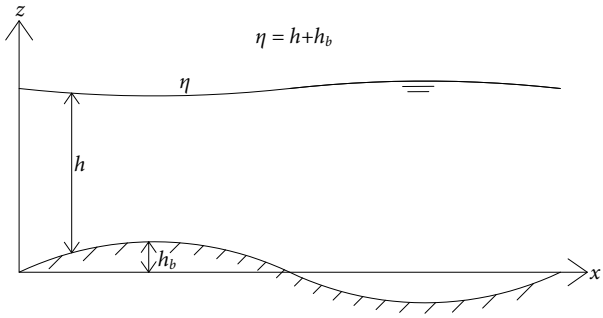

Figure 3.1: Definition sketch

The hydrodynamics are described by the nonlinear shallow water equations. The wavelengths of the bedforms that can be modeled in a 2DH model are several orders of magnitude larger than the depth, hence assuming shallow water conditions with only the gravitational acceleration in the vertical direction is reasonable. The governing equations for the hydrodynamics in conservative form are thus given by the depth-averaged continuity equation (see comment regarding this form in Sec. 3.4)

$$\frac{\partial \eta}{\partial t} + \frac{\partial h\bar{u}}{\partial x} + \frac{\partial h\bar{v}}{\partial y} = 0 \tag{3.1}$$

and the depth-averaged momentum equations

$$\frac{\partial h\bar{u}}{\partial t} + \frac{\partial h\bar{u}^2}{\partial x} + \frac{\partial h\bar{v}\bar{u}}{\partial y} = -gh\frac{\partial \eta}{\partial x} + f_c h\bar{v} - \frac{\tau_{bx}}{\rho} + S_x h \tag{3.2}$$

$$\frac{\partial h\bar{v}}{\partial t} + \frac{\partial h\bar{u}\bar{v}}{\partial x} + \frac{\partial h\bar{v}^2}{\partial y} = -gh\frac{\partial \eta}{\partial y} - f_c h\bar{u} - \frac{\tau_{by}}{\rho} + S_y h \tag{3.3}$$

where $\boldsymbol{u} = [\bar{u}\ \bar{v}]^T$ is the depth averaged horizontal fluid velocity vector, h is the water depth, g is the gravitational acceleration, $\eta = h + h_b$ is the height of the water above $z = 0$, h_b is the bed elevation, f_c is the Coriolis frequency, $\boldsymbol{\tau}_b = [\tau_{bx}\ \tau_{by}]^T$ is the bed shear stress vector, ρ is the water density and $\boldsymbol{S} = [S_x\ S_y]^T$ is a source term vector, which will be specified later. Horizontal stress terms have been ignored. See Fig. 3.1 for a definition sketch.

The bed shear stress is modelled using a drag coefficient C_D such that

$$\frac{\boldsymbol{\tau}_b}{\rho} = C_D \boldsymbol{u}|\boldsymbol{u}| \tag{3.4}$$

3.2.1 Helical flow

When the streamline of the depth-averaged flow curves, then a spiraling motion known as helical flow is induced, well explained by Engelund (1974) in channel bends. Water near the surface will tend to move outwards to a curve with larger radius relative to the depth-averaged flow, while the opposite occurs for the smaller near bed velocities. The resulting motion can be considered as a spiral, hence the name helical flow. The motion can be considered as the sum of the stream-wise mean flow and lateral secondary flow. This effect is not implicitly included in virtue of the depth-averaging, and thus has to be accounted for separately. Although not significant for the hydrodynamics, it has a crucial impact on the sediment transport, as the bed shear stress will then be directed at an angle δ_s relative to the streamline of the mean flow. The helical flow model has been developed for river engineering, so how well it performs in the offshore environment is less known. It is however included in the present model since the primary flow is driven by a tide, i.e. quasi-steady current and also based on Hulscher et al. (1993) and Hulscher (1996) work, which demonstrated the crucial role of secondary current effects on the generation of bedforms in the offshore environment.

de Vriend (1981) defined the helical flow intensity i_s as

$$i_s = |\boldsymbol{u}| \frac{h}{R_s} \tag{3.5}$$

where R_s is the local radius of the streamline curvature. For quasi-steady conditions it can be obtained by calculating the cross product between the velocity and acceleration vectors, yielding

$$\frac{1}{R_s} = -\frac{\bar{u}^2 \frac{\partial \bar{v}}{\partial x} + \bar{u}\bar{v}\left(\frac{\partial \bar{v}}{\partial y} - \frac{\partial \bar{u}}{\partial x}\right) - \bar{v}^2 \frac{\partial \bar{u}}{\partial y}}{|\boldsymbol{u}|^3} \tag{3.6}$$

From the above it can be seen that when the streamline is curving to the left R_s is negative and positive when curving to the right. Rozovskii (1961) used a mixing length model that yields logarithmic flow profiles to obtain a bed shear stress angle given by

$$\tan \delta_s = -\beta \frac{h}{R_s} \tag{3.7}$$

where the parameter β can be related to flow resistance. For logarithmic flow profiles β is either set to a fixed value in the range 7-11, or alternatively calculated, as implemented in the present model, by

$$\beta = \frac{2}{\kappa^2}\left(1 - \frac{\sqrt{C_D}}{\kappa}\right) \tag{3.8}$$

where $\kappa = 0.4$ is the Von Karman constant.

Inertial effects play a role on the intensity of the helical flow and are therefore accounted for by introducing the adaption length λ_s, defined as

$$\lambda_s = \alpha_s \frac{h}{\sqrt{C_D}} \tag{3.9}$$

where α_s is a calibration constant. de Vriend (1981) suggests a value of $\alpha_s = 1.3$ for helical flow intensity, however, the bed shear stress has a faster adaption and it is therefore sometimes recommended to use a value of $\alpha_s = 0.6$, in that case. A value of $\alpha_s = 0$ means instantaneous adaption, which Olesen (1987) mentions to be valid for the bed shear stress in most cases, however, it may cause stability problems in the morphological model.

By introducing a right-handed streamline coordinate system, the angle δ_s including inertia effects is thus obtained from

$$\lambda_s \frac{\partial \tan \delta_s}{\partial s} + \tan \delta_s = -\beta \frac{h}{R_s} \tag{3.10}$$

Eq. (3.10) is projected into the Cartesian coordinate system and supplemented with an unsteady term giving

$$\frac{\partial \tan \delta_s}{\partial t} + \bar{u}\frac{\partial \tan \delta_s}{\partial x} + \bar{v}\frac{\partial \tan \delta_s}{\partial y} = -\frac{\lambda_s}{|\boldsymbol{u}|}\left(\beta \frac{h}{R_s} + \tan \delta_s\right) \tag{3.11}$$

where projection from streamline (s, n) coordinates to Cartesian (x, y) coordinates is achieved via the following relations:

$$\frac{\partial}{\partial s} = \frac{\bar{u}}{|\boldsymbol{u}|}\frac{\partial}{\partial x} + \frac{\bar{v}}{|\boldsymbol{u}|}\frac{\partial}{\partial y} \tag{3.12}$$

$$\frac{\partial}{\partial n} = \frac{\bar{u}}{|\boldsymbol{u}|}\frac{\partial}{\partial y} - \frac{\bar{v}}{|\boldsymbol{u}|}\frac{\partial}{\partial x} \tag{3.13}$$

The bed shear stress correction due to helical motion described above is only applied passively for the sediment transport module (described later), and not in the nonlinear shallow water equations.

3.3 Sediment transport

The sediment transport is modeled using separate formulations for bed load and suspended load. The Shields parameter,

$$\theta = \frac{u_f^2}{(\varrho - 1)g d_{50}} \tag{3.14}$$

is used as the main parameter for quantifying the sediment transport. Here $\varrho = 2.65$ is the relative density of sand, d_{50} is the mean grain diameter and the friction velocity u_f is defined as

$$u_f = \sqrt{\frac{|\boldsymbol{\tau}_b|}{\rho}} \tag{3.15}$$

The sediment transport is calculated in the streamline coordinate system (s, n) and later projected into the (x, y) Cartesian coordinate system, as described above.

3.3.1 Bed load

The bed load transport is modeled through its relation to the bed shear stress. The total bed shear stress which acts as the total flow resistance is comprised from two contributions. As suggested by Einstein (1950): $\tau_b = \tau' + \tau''$, where the single prime accounts for skin friction on the grains and double prime accounts for bluff body form drag due to small scale unresolved bedforms such as dunes and ripples. The bed load is assumed to be driven only by the part of the bed shear stress related to skin friction, hence it is modeled from the single prime component.

Engelund and Fredsøe (1976) derived a bed load equation from a balance between the agitating and stabilizing forces on a sediment particle laying on the bed. This balance yields the following relation for bed load transport

$$q_b = a\frac{\pi}{6}P\left(\sqrt{\theta'} - 0.7\sqrt{\theta_c}\right)\sqrt{(\varrho-1)gd_{50}^3} \tag{3.16}$$

where $a \simeq 10$, θ' is the Shields parameter value associated with skin friction, θ_c is the Shields parameter value of incipient bed particle motion, and P is representing the probability between zero and unity, that a certain fraction of particles in a single layer are in motion. The probability P is found by

$$P = \left(1 + \left(\frac{\frac{\pi}{6}\mu_d}{\theta' - \theta_c}\right)^4\right)^{-\frac{1}{4}} \tag{3.17}$$

where μ_d is the dynamic coefficient of motion of the sediment, estimated at 0.51.

3.3.1.1 Incipient motion - Critical Shields value

The Shields parameter value at incipient motion over a flat bed can be determined in one of the following ways:

The modified Shields diagram (Sumer and Fredsøe, 2002, Fig 1.2) in terms of grain diameter, can be approximated by the expression

$$\theta_{c0} = 0.17\left(Re_d + 0.6\right)^{-0.8} + 0.045\exp\left(-40Re_d^{-1.3}\right) \tag{3.18}$$

where the grain Reynolds number is defined as

$$Re_d = \frac{u'_f d_{50}}{\nu} \tag{3.19}$$

where ν is the kinematic viscosity. This expression is valid approximately for $Re_d \geq 1$.

Alternatively Soulsby and Whitehouse (1997) give the following expression for determination of the critical Shield stress

$$\theta_{c0} = \frac{0.3}{1 + 1.2D_*} + 0.055\left(1 - e^{-0.02D_*}\right) \tag{3.20}$$

where the dimensionless grain size is defined as

$$D_* = \left(\frac{g(\varrho-1)}{\nu^2}\right)^{\frac{1}{3}} d_{50} \tag{3.21}$$

The latter approach (Eq. 3.20) yields a constant θ_{c0} in the domain, while the former (Eq. 3.18) allows it to vary as a function of the flow. Both are implemented in the model and can be selected by an input switch.

3.3.1.2 Skin friction

To estimate the skin friction component of the bed shear stress τ_b', Einstein (1950) suggested that the converging flow above the stoss side of bed dunes, would have the characteristics of a turbulent boundary layer. Above that layer, in the rest of the water column, a uniform profile would exist. The boundary layer profile is given by

$$\frac{|\boldsymbol{u}|}{u_f'} = 6 + 2.5 \ln\left(\frac{\delta}{k_N}\right) \tag{3.22}$$

where $k_N = 2.5 d_{50}$ is the Nikuradse equivalent roughness related to the grain diameter and δ is the thickness of the boundary layer. Since the equation includes two unknowns (u_f' and δ), a second equation is introduced

$$u_f' = \sqrt{g \delta I} \tag{3.23}$$

where I is the energy gradient given by

$$I = \frac{|\boldsymbol{u}|^2}{gh} C_D \tag{3.24}$$

Inserting Eqs. (3.4, 3.15, 3.24) in Eq. (3.23) gives the following relation

$$\frac{u_f'^2}{u_f^2} = \frac{\delta}{h} \tag{3.25}$$

which is then inserted in Eq. (3.22) to yield

$$\frac{|\boldsymbol{u}|}{u_f'} = 6 + 2.5 \ln\left(\frac{h}{k_N} \frac{u_f'^2}{u_f^2}\right) \tag{3.26}$$

whereby u_f' is found by iteration. When u_f' is found, it is inserted in an equation identical to Eq. (3.14), but with prime superscripts, to find θ'. One of the shortcomings of this method is that it uses the mean flow velocity of the total depth, while other parameters are for the near-bed boundary layer only. Einstein developed this concept for straight current dominated channels such as rivers, where many measurements are available, the flow is friction controlled and a surface slope known. In the sea such measurements are much more difficult to obtain and estimation of bed resistance still presents a major challenge in the modeling of offshore environments. As an alternative, Soulsby (1997) suggested a similar method which does not require an iteration and uses the total water depth.

First, it is assumed that a sea current may be described by a rough turbulent logarithmic profile, which yields the following expression for the drag coefficient:

$$C_D = \left[\frac{\kappa}{1 + \ln\left(\frac{z_0}{h}\right)} \right]^2 \tag{3.27}$$

in which z_0 represents the total roughness height given by

$$z_0 = z_0' + z_0'' \tag{3.28}$$

thus combining the roughness height from skin friction and form drag. The skin friction roughness height is estimated to be directly related to the bed's mean grain diameter yielding

$$z_0' = \frac{k_N}{30} \tag{3.29}$$

as is the case of a plane bed. Solving Eq. (3.27) using $z_0 = z_0'$, yields $C_D = C_D'$, which is then used to calculate the skin friction velocity u_f' through a combination of Eqs. (3.4) and (3.15), yielding

$$u_f' = \sqrt{C_D'}|\boldsymbol{u}| \tag{3.30}$$

Then the skin friction Shields parameter θ' can be found, and the bed load calculated from Eq. (3.16).

Soulsby (1997) also suggested empirical relations to estimate the equivalent roughness height z_0'' due to bedforms, based on the grain size and flow conditions. For example, current generated ripples have a roughness height estimated by

$$z_0'' = a_r \frac{\Delta_r^2}{\lambda_r}, \quad \theta' \leq 0.8 \tag{3.31}$$

where a_r is a calibration coefficient, λ_r is the ripple length given by

$$\lambda_r = 1000 d_{50}; \tag{3.32}$$

and Δ_r is the ripples height given by

$$\Delta_r = \frac{\lambda_r}{7} \tag{3.33}$$

Similarly, for sandwaves van Rijn (1984b) suggests

$$k_s = 1.1\Delta_{sw}\left(1 - e^{-25\frac{\Delta_{sw}}{\lambda_{sw}}}\right) + 3d_{90} \tag{3.34}$$

which is inserted in a Chezy equation similar to Eq. (3.27). Here d_{90} is the diameter of the 90's percentile of the sediment grains in the bed,

$$\lambda_{sw} = 7.3h \tag{3.35}$$

and

$$\Delta_{sw} = \begin{cases} 0.11h\left(\frac{d_{50}}{h}\right)^{0.3}\left(1-e^{-0.5T_s}\right)(25-T_s) & \text{for } \theta_c < \theta' < 26\theta_c \\ 0 & \text{otherwise} \end{cases} \tag{3.36}$$

where $T_s = (\theta' - \theta_c)/\theta_c$. Similar expressions exist for wave-generated ripples.

Calculating the total roughness height using this approach, will implicitly fix the value of z_0 and limit a parametric study. Instead, in the present work z_0 is maintained as a free parameter, calculated by Eq. (3.27) from a mean value of C_D, which is specified as an input for the simulation. This means that the value of z_0'' does not need to be specified, as the important roughness height quantities are only z_0' (for the bed load calculation) and z_0 (for the total resistance, which affects the flow and the suspended sediment transport). This approach implies that various values of z_0'' can be studied, which may not fit with an empirically based value. However, the uncertainty on the direct estimation of z_0'' in the sea is so large, that the chosen approach is arguably as good if not better. In any event, this approach allows a full physical range of possibilities to be studied, without reliance on any particular form drag model.

Another very straightforward option for direct estimation of the skin friction Shields parameter (in straight alluvial channels), was suggested by Engelund and Fredsøe (1982) through the empirical relation

$$\theta' = 0.06 + 0.03\theta^{3/2} \quad \text{for } \theta' \leq 0.55 \tag{3.37}$$

All of the above-mentioned three methods, Einstein (1950); Soulsby (1997); Engelund and Fredsøe (1982), are implemented in the model and can be selected by an input switch.

3.3.1.3 Bed load transport over a sloping bed

As mentioned in chapter 2, a sloping bed affects the bed load transport since the grains are more easily transported downhill than uphill. Additionally, a transverse slope will divert the transport direction from the flow direction. For small bed slopes, Olesen (1987) shows that the effect can be accounted for with a modification of the bed load found by Eq. (3.16) in the following way:

$$q_{bs} = q_b\left(1 - \alpha\frac{\partial h_b}{\partial s}\right) \tag{3.38}$$

where s represents the horizontal coordinates along a streamline and α is a coefficient estimated from

$$\alpha = \frac{3}{2}\frac{\theta_c}{\theta' - \theta_c} \tag{3.39}$$

The transverse bed slope effect is similarly accounted for by the equation

$$q_{bn} = q_b \left(\tan \delta_s - \frac{1}{f(\theta)} \frac{\partial h_b}{\partial n} \right) \tag{3.40}$$

which also includes the deviation of the bed shear stress direction due to helical motion. The function $f(\theta) = 0.8\sqrt{\theta}$ is estimated based on experimental data compiled from many experiments by Talmon et al. (1995). In Eq. (3.40), n represents the horizontal coordinates normal to the streamline. Lastly, the bed load transport in the Cartesian coordinates is found by

$$q_{bx} = q_{bs} \frac{\bar{u}}{|\boldsymbol{u}|} - q_{bn} \frac{\bar{v}}{|\boldsymbol{u}|} \tag{3.41}$$

$$q_{by} = q_{bn} \frac{\bar{u}}{|\boldsymbol{u}|} + q_{bs} \frac{\bar{v}}{|\boldsymbol{u}|} \tag{3.42}$$

One of the shortcomings of this method that Talmon et al. (1995) mentions, is that there is a large degree of uncertainty in the estimation of $f(\theta)$ when it comes to a model that includes suspended load.

Kovacs and Parker (1994) suggested a vectorial way to calculate the direction and magnitude of the bed load transport over an arbitrarily sloped bed. Using a three dimensional vector space in Cartesian coordinates, a unit vector

$$\hat{\boldsymbol{n}} = \begin{bmatrix} -\frac{\partial h_b}{\partial x} \\ -\frac{\partial h_b}{\partial y} \\ \sqrt{1 - \left(-\frac{\partial h_b}{\partial x}\right)^2 - \left(-\frac{\partial h_b}{\partial y}\right)^2} \end{bmatrix} \tag{3.43}$$

normal to the bed surface, and a unit downward vertical vector

$$-\hat{\boldsymbol{k}} = -\begin{bmatrix} 0 \\ 0 \\ 1 \end{bmatrix} \tag{3.44}$$

are defined. Thereby the components normal ($\boldsymbol{k}_n$) and tangential ($\boldsymbol{k}_t$) to the plane of the bed can be found by

$$\boldsymbol{k}_n = -(\hat{\boldsymbol{k}} \cdot \hat{\boldsymbol{n}})\hat{\boldsymbol{n}} \tag{3.45}$$

and

$$\boldsymbol{k}_t = \hat{\boldsymbol{k}} + (\hat{\boldsymbol{k}} \cdot \hat{\boldsymbol{n}})\hat{\boldsymbol{n}} \tag{3.46}$$

Kovacs and Parker show that a force balance on a bed particle between the agitating and stabilizing forces reduces to

$$|\boldsymbol{u}_r|\boldsymbol{u}_r = G \left(|\boldsymbol{k}_n| \frac{\boldsymbol{v}_p}{|\boldsymbol{v}_p|} - \frac{\boldsymbol{k}_t}{\mu_d} \right) \tag{3.47}$$

where G is a constant defined later and $\boldsymbol{u}_r$ is the relative velocity between the near bed velocity $\boldsymbol{u}_b$, and the sediment particle velocity $\boldsymbol{v}_p$, expressed as

$$\boldsymbol{u}_r = \boldsymbol{u}_b - \boldsymbol{v}_p \tag{3.48}$$

The near bed velocity vector can deviate from the mean current direction due to the helical flow, thus in a depth-averaged model the orientation of it can be found by

$$\boldsymbol{u}_\delta = \begin{bmatrix} \bar{u}\cos\delta_s - \bar{v}\sin\delta_s \\ \bar{u}\sin\delta_s + \bar{v}\cos\delta_s \\ |\boldsymbol{u}|\frac{\partial h_b}{\partial s} \end{bmatrix} \tag{3.49}$$

whereby a unit vector tangent to the surface in the direction of the bed shear stress can be defined as

$$\hat{\boldsymbol{s}} = \frac{\boldsymbol{u}_\delta}{|\boldsymbol{u}_\delta|} \tag{3.50}$$

The near bed velocity acting on a sediment particle can then be calculated from

$$\boldsymbol{u}_b = u_b \hat{\boldsymbol{s}} \tag{3.51}$$

where a common estimation used is $u_b = au'_f$. The value of a is evaluated by a log law estimation whereby it could be estimated as $a = 1/\sqrt{C_D}$ and be in the range 8-14. Engelund and Fredsøe (1976) derived their bed load formula (Eq. 3.16) using a similar force balance as in Eq. (3.47) over a horizontal bed. Therefore, $a = 10$ is also set here, to obtain an expression which is consistent with Engelund and Fredsøe's bed load formula.

The constant in Eq. (3.47) is given by

$$G = (\varrho - 1)gd_{50}a^2\frac{\theta_{c0}}{2} \tag{3.52}$$

The division of the critical Shields θ_{c0} by 2 is not included in Kovacs and Parker's model, but Engelund and Fredsøe found it to yield better results with their formula based on Luque's (1974) work.

Eq. (3.47) is rewritten to set an iteration scheme whereby the particle velocity $\boldsymbol{v}_p$ can be obtained from

$$\boldsymbol{v}_p = \frac{|\boldsymbol{u}_r|\boldsymbol{u}_b + G\boldsymbol{k}_t}{\mu_d G\frac{\boldsymbol{v}_p}{|\boldsymbol{v}_p|}|\boldsymbol{u}_r|} \tag{3.53}$$

The critical Shields parameter is also modified by the bed slope such that incipient motion occurs at lower values downslope and higher values upslope. Kovacs and Parker express this as

$$\left|\frac{\theta_c}{\theta_{c0}}\hat{\boldsymbol{s}} + \frac{\boldsymbol{k}_t}{\mu_d}\right| = |\boldsymbol{k}_n| \tag{3.54}$$

Note that this slope adjusted critical Shields is used when calculating the probability in Eq. (3.17).

Lastly, after obtaining $\boldsymbol{v}_p$ and P, the bed load can be calculated from

$$\boldsymbol{q}_b = \frac{1}{6}\pi d P \boldsymbol{v}_p; \tag{3.55}$$

The bed load would be identical to Eq. 3.16 for a horizontal flat bed.

Both of the above approaches for accounting for bed slope effects (Olesen, 1987) and (Kovacs and Parker, 1994) are implemented in the model and can be selected by an input switch.

3.3.2 Suspended load

The determination of suspended load in depth averaged-models poses a major challenge. The approaches available are either using a bulk total load formula or utilizing more detailed assumed vertical profiles, as done in this work. The suspended load is modeled using a pseudo-3D assumption of the vertical velocity profiles with a full first order unsteady flow calculation. Thereby an estimation of the mean volumetric concentration of sediments $\bar{c}$ is obtained, and used to find the suspended load transport by

$$q_s = |\boldsymbol{u}| h \bar{c} \tag{3.56}$$

3.3.2.1 Velocity profiles

Since the model is depth-averaged, information about the vertical variations in the velocities has to be assumed. First, a vertical coordinate $\zeta = z/h$ is introduced, in which the level $\zeta_0 = z_0/h$ represents the no-slip level of the velocity profile, see Figure 3.2. Above this level all transport is considered to be in suspension and below it is conceptually accounted for as bed load.

The stream-wise velocity profile u_s is assumed to be fully developed and turbulent, described as the product of the mean velocity $|\boldsymbol{u}|$ and a unit profile $p_s(\zeta)$,

$$u_s = |\boldsymbol{u}| p_s(\zeta) \tag{3.57}$$

where

$$p_s(\zeta) = \frac{\sqrt{C_D}}{\kappa} \ln\left(\frac{\zeta}{\zeta_0}\right), \quad \int_{\zeta_0}^{1} p_s(\zeta) d\zeta = 1 \tag{3.58}$$

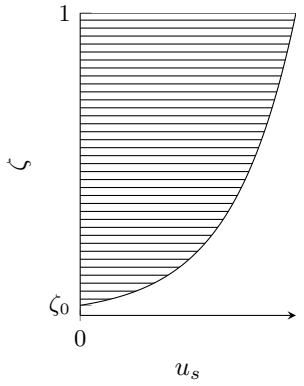

Figure 3.2: Velocity profile in ζ coordinates.

It follows from Eq. (3.58) that the reference level ζ_0 can be calculated iteratively from

$$\zeta_0 = e^{\zeta_0 - 1 - \kappa/\sqrt{C_D}} \tag{3.59}$$

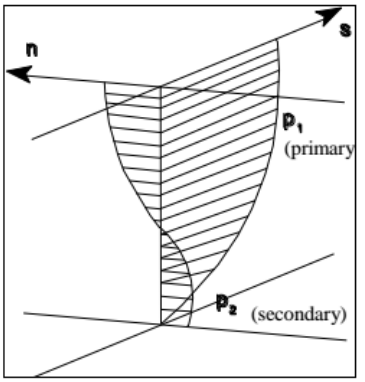

Figure 3.3: Stream-wise (p_1) and lateral (p_2) velocity profiles. Credit DHI (2013b)

The curvature of the streamlines which causes the previously discussed helical flow induces a lateral velocity profile (secondary flow), described using the helical flow intensity from Eq. (3.5) by

$$v_n = i_s p_n(\zeta) = \frac{|\boldsymbol{u}|h}{R} p_n(\zeta), \quad \int_{\zeta_0}^{1} p_n(\zeta) d\zeta = 0 \tag{3.60}$$

The exhaustive derivation of $p_n(\zeta)$ is not included here but can be found in

DHI (2013b). As can be seen, there is no net flow in the lateral direction. However, there will be a net flux of suspended sediments, due to the nature of the concentration to be largest close to the bed. Figure 3.3 illustrates the vertical profiles of the horizontal velocities in the streamline coordinate system.

3.3.2.2 First order solution

The governing equation for the suspended sediment is a transport equation for the volumetric concentration c,

$$\frac{\partial c}{\partial t} + u\frac{\partial c}{\partial x} + v\frac{\partial c}{\partial y} + (w - w_s)\frac{\partial c}{\partial z} = \frac{\partial}{\partial x}\left(\nu_T \frac{\partial c}{\partial x}\right) + \frac{\partial}{\partial y}\left(\nu_T \frac{\partial c}{\partial y}\right) + \frac{\partial}{\partial z}\left(\nu_T \frac{\partial c}{\partial z}\right) \tag{3.61}$$

where ν_T is the eddy viscosity, w the vertical velocity component and w_s is the fall velocity of sediments, which can either be input explicitly in the model or calculated from Rubey (1933)

$$w_s = \sqrt{(\varrho - 1)gd}\left(\left(\frac{2}{3} + \frac{36\nu^2}{(\varrho - 1)gd^3}\right)^{\frac{1}{2}} - \left(\frac{36\nu^2}{(\varrho - 1)gd^3}\right)^{\frac{1}{2}}\right) \tag{3.62}$$

or from Soulsby (1997)

$$w_s = \frac{\nu}{d}\left(\sqrt{10.36^2 + 1.049D_*^3} - 10.36\right) \tag{3.63}$$

which uses the non-dimensional grain diameter D_* from Eq. (3.21).

The solution to Eq. (3.61) is found using Galappatti's (1983) model for suspended sediment in depth-averaged flows. Galappatti used an asymptotic technique to obtain approximate solutions to the concentration profile. This approach is suitable for situations where the vertical diffusion and fall velocity dominate the transport equation (i.e. the terms on the right hand side of Eq. (3.61)). Galappatti's (1983) model has been expanded by DHI (2013b) to include the helical flow effects, where a detailed description of the model is also found. In the following the key points of the model are presented.

Similarly to the assumed velocity profiles, the zeroth-order concentration profile is defined as the product of the depth-averaged concentration $\bar{c}$ and a unit profile Φ_0, defined by

$$\Phi_0(\zeta) = e^{Z_g f(\zeta)} \tag{3.64}$$

in which

$$f(\zeta) = \begin{cases} \ln\left(\frac{1-\zeta}{\zeta}\right) & \text{for } \zeta < \frac{1}{2} \\ -4\zeta + 2 & \text{for } \zeta \geq \frac{1}{2} \end{cases} \tag{3.65}$$

and using a modified Rouse parameter

$$Z_g = \frac{w_s}{4u_f} \frac{1}{0.13 + 0.2\left(\frac{w_s}{u_f}\right)^{2.12}} \tag{3.66}$$

Assuming spatial variations in Φ to be negligible, the first-order concentration profile is given by

$$c(\zeta) = \Phi_0(\zeta)\bar{c} + \Phi_t(\zeta)\frac{h}{w_s}\frac{\partial \bar{c}}{\partial t} + \Phi_s(\zeta)\frac{|\boldsymbol{u}|h}{w_s}\frac{\partial \bar{c}}{\partial s} + \Phi_n(\zeta)\frac{|\boldsymbol{u}|h^2}{R_s w_s}\frac{\partial \bar{c}}{\partial n} \tag{3.67}$$

where

$$\begin{aligned} \Phi_t(\zeta) &= f(\Phi_0(\zeta)) \\ \Phi_s(\zeta) &= f(\Phi_0(\zeta)p_s(\zeta)) \\ \Phi_n(\zeta) &= f(\Phi_0(\zeta)p_n(\zeta)) \end{aligned} \tag{3.68}$$

The evaluation of the functions in Eq. (3.68) are for simplicity not included here, but can be seen in the referenced literature Galappatti (1983); DHI (2013b).

Due to the sediment fall velocity, w_s, usually being much smaller than the flow velocity, a phase lag in the suspended load in changing flow conditions will occur as the concentration needs to adapt. However, at the no-slip level $\zeta = \zeta_0$, it is assumed that the concentration has instantaneous adaption, and will therefore be in phase with the bed shear stress, as is the case with bed load transport. When no phase lag exists in the suspended load, it can be considered being in equilibrium, whereby it can be deduced that for the equilibrium concentration c_e the following holds

$$c(\zeta_0) = c_e(\zeta_0) = \bar{c}_e\Phi_0(\zeta_0) \tag{3.69}$$

Inserting this as a bottom boundary condition into Eq. (3.67) yields

$$\bar{c}_e\Phi_0(\zeta_0) = \Phi_0(\zeta_0)\bar{c} + \Phi_t(\zeta_0)\frac{h}{w_s}\frac{\partial \bar{c}}{\partial t} + \Phi_s(\zeta_0)\frac{|\boldsymbol{u}|h}{w_s}\frac{\partial \bar{c}}{\partial s} + \Phi_n(\zeta_0)\frac{|\boldsymbol{u}|h^2}{R_s w_s}\frac{\partial \bar{c}}{\partial n} \tag{3.70}$$

which can be rearranged into

$$\frac{\partial \bar{c}}{\partial t} = \frac{\bar{c}_e - \bar{c} - L_{As}\frac{\partial \bar{c}}{\partial s} - L_{An}\frac{\partial \bar{c}}{\partial n}}{T_A} \tag{3.71}$$

In Cartesian coordinates this translates to

$$\frac{\partial \bar{c}}{\partial t} = \frac{\bar{c}_e - \bar{c} - \frac{\partial \bar{c}}{\partial x}\left(\frac{\bar{u}}{|\boldsymbol{u}|}L_{As} - \frac{\bar{v}}{|\boldsymbol{u}|}L_{An}\right) - \frac{\partial \bar{c}}{\partial y}\left(\frac{\bar{u}}{|\boldsymbol{u}|}L_{An} + \frac{\bar{v}}{|\boldsymbol{u}|}L_{As}\right)}{T_A} \tag{3.72}$$

where an adaption time can be identified as

$$T_A = \frac{\Phi_t(\zeta_0)}{\Phi_0(\zeta_0)}\frac{h}{w_s} \tag{3.73}$$

and two adaption lengths given by

$$L_{As} = \frac{\Phi_s(\zeta_0)}{\Phi_0(\zeta_0)} \frac{|\boldsymbol{u}|h}{w_s} \tag{3.74}$$

$$L_{An} = \frac{\Phi_n(\zeta_0)}{\Phi_0(\zeta_0)} \frac{|\boldsymbol{u}|h^2}{R_s w_s} \tag{3.75}$$

Eq. 3.72 is solved in the model in order to obtain the depth-averaged concentration $\bar{c}$. The value of $\bar{c}_e$ is estimated based on an equilibrium conditions calculation, described later.

The suspended transport in the stream-wise direction can then be calculated by

$$q_{ss} = \int_{\zeta_0}^{1} h u_s c d\zeta = |\boldsymbol{u}|h \left(\alpha_{0s}\bar{c} + \alpha_{ts} \frac{h}{w_s} \frac{\partial \bar{c}}{\partial t} + \alpha_{ss} \frac{|\boldsymbol{u}|h}{w_s} \frac{\partial \bar{c}}{\partial s} + \alpha_{ns} \frac{|\boldsymbol{u}|h^2}{w_s R_s} \frac{\partial \bar{c}}{\partial n} \right) \tag{3.76}$$

and in the lateral direction by

$$q_{sn} = \int_{\zeta_0}^{1} h v_n c d\zeta = \frac{|\boldsymbol{u}|h^2}{R_s} \left(\alpha_{0n}\bar{c} + \alpha_{tn} \frac{h}{w_s} \frac{\partial \bar{c}}{\partial t} + \alpha_{sn} \frac{|\boldsymbol{u}|h}{w_s} \frac{\partial \bar{c}}{\partial s} + \alpha_{nn} \frac{|\boldsymbol{u}|h^2}{w_s R_s} \frac{\partial \bar{c}}{\partial n} \right) \tag{3.77}$$

where

$$\alpha_{ij} = \int_{\zeta_0}^{1} \Phi_i(\zeta) p_j(\zeta) d\zeta \quad \text{for} \quad i = \{0, t, s, n\} \text{ and } j = \{s, n\} \tag{3.78}$$

Eqs. (3.76) and (3.77) are then projected into Cartesian coordinates to yield the suspended load transport rates

$$q_{sx} = q_{ss} \frac{\bar{u}}{|\boldsymbol{u}|} - q_{sn} \frac{\bar{v}}{|\boldsymbol{u}|} \tag{3.79}$$

$$q_{sy} = q_{sn} \frac{\bar{u}}{|\boldsymbol{u}|} + q_{ss} \frac{\bar{v}}{|\boldsymbol{u}|} \tag{3.80}$$

3.3.2.3 Equilibrium conditions

The equilibrium transport rate of suspended sediment can be expressed as

$$q_{se} = |\boldsymbol{u}|h\bar{c}_e \tag{3.81}$$

In order to estimate the value of q_{se}, consider that in equilibrium conditions Eq. (3.61) may be reduced to

$$\frac{\partial}{\partial \zeta} \left(\nu_T \frac{\partial c}{\partial \zeta} \right) + w_s \frac{\partial c}{\partial \zeta} = 0 \tag{3.82}$$

Assuming a parabolic distribution of the eddy viscosity

$$\nu_T = \kappa u_f \zeta (1 - \zeta) \tag{3.83}$$

leads to the well known Rouse profile given by

$$c_e = c_b \left(\frac{1 - \zeta}{\zeta} \frac{a_{ref}}{1 - a_{ref}} \right)^Z \tag{3.84}$$

where $a_{ref} = 2d/h$ is the so-called reference level,

$$Z = \frac{w_s}{\kappa u_f} \tag{3.85}$$

is the Rouse parameter, and

$$c_b = \frac{0.331(\theta' - \theta_c)^{1.75}}{1 + \frac{0.331}{0.46}(\theta' - \theta_c)^{1.75}} \tag{3.86}$$

is the reference concentration of the suspended load profile at the level a_{ref}, calculated by the Zyserman and Fredsøe (1994) equation. The suspended load transport rate in equilibrium conditions is given by

$$q_{se} = |\boldsymbol{u}| h \int_{\max(\zeta_0, a_{ref})}^{1} p_s c_e d\zeta \tag{3.87}$$

When q_{se} has been obtained, it is used in Eq. (3.81) to calculate the mean volumetric concentration

$$\bar{c}_e = \frac{q_{se}}{|\boldsymbol{u}| h} \tag{3.88}$$

which is then used in Eq. (3.72).

Soulsby (1997) argues that the parabolic eddy viscosity which leads to $c_e = 0$ at the surface may underestimate the concentration values near the surface and therefore suggests the use of van Rijn (1984a) or a power law to describe the eddy viscosity in the sea. However, since the concentration of suspended sediments in this work is mainly near the bed, it is estimated that the Rouse profile is sufficient for estimation of the equilibrium conditions.

3.3.3 Bed morphology

When sediment transport processes are active, the bed becomes mobile and begins to morph. As explained in Chapter 2, the bed load accounts for the transported sediments that remain in contact with the bed and the suspended

load accounts for the sediments carried by the flow in suspension. The latter results in erosion when sediments are suspended and deposition when the sediments settle back on the bed. The rate of bed level change can be determined by the sediment transport mass conservation equation, also called the Exner equation

$$\frac{\partial h_b}{\partial t} = -\frac{1}{1-\varepsilon_p} f_A \left(\frac{\partial q_{bx}}{\partial x} + \frac{\partial q_{by}}{\partial y} + E \right) \tag{3.89}$$

where $\varepsilon_p = 0.4$ is the bed porosity and f_A is a speed up factor to amplify the rate of bed level change. The last term on the right hand side, E, is the entrainment rate associated with suspended load. E is generally a function of $(\bar{c}_e - \bar{c})$, in which deposition is occurring when $\bar{c}_e < \bar{c}$, i.e. the system is overloaded, and erosion when $\bar{c}_e > \bar{c}$, i.e the system is underloaded.

Going back to the suspended load model of Galappatti (1983), the depth-averaged transport in suspension can be expressed by considering a mass balance of suspended sediment in a vertical water column

$$\frac{\partial h\bar{c}}{\partial t} + \frac{\partial q_{sx}}{\partial x} + \frac{\partial q_{sy}}{\partial y} = E \tag{3.90}$$

where the left-hand-side represents the temporal change of sediment volume in suspension and the spatial variation of depth-averaged sediment fluxes through the water column, while the term on the right-hand-side is the previously mentioned entrainment term, which accounts for fluxes through the bottom of the water column.

Combining Eqs. (3.89) and (3.90) yields

$$\frac{\partial h_b}{\partial t} = -\frac{f_A}{1-\varepsilon_p} \left(\frac{\partial (q_{bx} + q_{sx})}{\partial x} + \frac{\partial (q_{by} + q_{sy})}{\partial y} \right) \tag{3.91}$$

In quasi-steady simulations, the unsteady term $\partial h\bar{c}/\partial t$ is usually negligible and therefore omitted in the above equation.

3.4 Numerical model

The equations presented in the Hydrodynamic and Sediment transport sections are programmed in Matlab, such that Eqs. (3.1), (3.2), (3.3), (3.11), (3.72) and (3.91) form the system of equations. For convenience these are listed below with the time derivatives isolated on the left-hand-side of each equation, whereby the

solved-for variables are η, $h\bar{u}$, $h\bar{v}$, $\tan\delta_s$, $\bar{c}$ and h_b.

$$\frac{\partial \eta}{\partial t} = -\frac{\partial h\bar{u}}{\partial x} - \frac{\partial h\bar{v}}{\partial y} \tag{3.1}$$

$$\frac{\partial h\bar{u}}{\partial t} = -\frac{\partial h\bar{u}^2}{\partial x} - \frac{\partial h\bar{v}\bar{u}}{\partial y} - gh\frac{\partial \eta}{\partial x} + f_c h\bar{v} - \frac{\tau_{bx}}{\rho} + S_x h \tag{3.2}$$

$$\frac{\partial h\bar{v}}{\partial t} = -\frac{\partial h\bar{u}\bar{v}}{\partial x} - \frac{\partial h\bar{v}^2}{\partial y} - gh\frac{\partial \eta}{\partial y} - f_c h\bar{u} - \frac{\tau_{by}}{\rho} + S_y h \tag{3.3}$$

$$\frac{\partial \tan\delta_s}{\partial t} = -\bar{u}\frac{\partial \tan\delta_s}{\partial x} - \bar{v}\frac{\partial \tan\delta_s}{\partial y} - \frac{|\boldsymbol{u}|}{\lambda_s}\left(\beta\frac{h}{R_s} + \tan\delta_s\right) \tag{3.11}$$

$$\frac{\partial \bar{c}}{\partial t} = \frac{\bar{c}_e - \bar{c} - \frac{\partial \bar{c}}{\partial x}\left(\frac{\bar{u}}{|\boldsymbol{u}|}L_{As} - \frac{\bar{v}}{|\boldsymbol{u}|}L_{An}\right) - \frac{\partial \bar{c}}{\partial y}\left(\frac{\bar{u}}{|\boldsymbol{u}|}L_{An} + \frac{\bar{v}}{|\boldsymbol{u}|}L_{As}\right)}{T_A} \tag{3.72}$$

$$\frac{\partial h_b}{\partial t} = -\frac{f_A}{1-\varepsilon_p}\left(\frac{\partial (q_{bx} + q_{sx})}{\partial x} + \frac{\partial (q_{by} + q_{sy})}{\partial y}\right) \tag{3.91}$$

Bed morphology is infamously the source of many stability problems in numerical models, and (although not implemented here) may be treated with separate schemes and filters.

Notice that other shallow water models may use the flow depth h instead of the surface elevation η in the time derivative of Eq. (3.1). The presented model herein couples different time scales of the hydro- and morphodynamics and does not include any external bed changing sources. Hence, bed level changes are exclusively caused by sediment erosion and deposition processes that are contained in the domain. A simple way to validate the use of η rather than h is by imagining a uniform concentration of suspended sediments in the whole domain with still standing water. As the concentration settles to the bottom and causes an increase in the bed elevation, the surface elevation remains unaffected, since no volumetric change has occurred.

3.4.1 Temporal integration

The system of equations is programmed in a way that allows it to be solved using one of Matlab's Ordinary Differential Equation (ODE) solvers. These include Runge-Kutta algorithms, which are all single-step, multi-stage solvers, meaning that new time-step values are estimated in a multi-stage manner, depending only on the previous time-step values. Example of such solvers in Matlab are `ode45`, `ode23`, `ode23s`, `ode23t`, and `ode23tb`. There are also multi-step algorithms available, such as `ode113` and `ode15s`, which use the results of several past steps.

The Matlab solvers feature built-in dynamic time stepping and error control. The naming convention of Matlab's ODE solvers reveals the order of the scheme used to estimate the error, such that e.g. `ode23` compares the result of a 2nd-order Runge-Kutta method and a 3rd-order Runge-Kutta method, and similarly `ode45` compares that of a 4th-order and a 5th-order Runge-Kutta method. Given the input tolerance, the solver then uses the error estimation in order to determine the necessary step size. The solver used throughout the present work is `ode23`, which has been found to attain a good combination of sufficient accuracy and computation time.

3.4.2 Spatial discretization

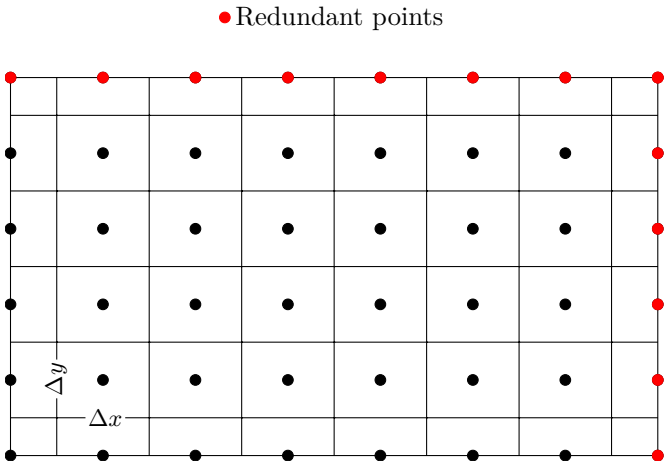

Figure 3.4: Computational domain.

The computational domain on which the model is simulated is a two-dimensional rectangular uniform grid (i.e. constant Δx, Δy) with periodic boundaries, illustrated in Fig. 3.4. Periodic boundaries imply that any modeled bedform within the grid, represents an infinite train of repeated identical bedforms. It is important to mention that the periodicity is implemented such that the horizontal and vertical boundaries cycle the variables, respectively, whereby redundancy should be considered when initial conditions are set.

3.4.2.1 Horizontal differentiation

Horizontal spatial differentiation is performed with spectral accuracy, making wide use of Matlab's 2D Fast Fourier Transformation (FFT) function (`fft2`). The advantage of the spectral method over finite difference/volume methods lies in its high accuracy, hence giving essentially no numerical dissipation. Its favorability in terms of accuracy and time for the present work is demonstrated in Chapter 5, as it is ideal for use in perturbation analyses using basic trigonometric functions. Since the spectral method relies on being able to represent the variables with finite series, the main disadvantage of it is its difficulty dealing with shocks/discontinuities, which pollute the solution. The current application of the spectral method also requires the grid points to be equidistant in each direction. In order to prevent high frequencies from polluting the variables, an Orszag 2/3 dealiasing technique is used for nonlinear operations (Orszag, 1971). For more information on spectral methods and it's application in Matlab see Boyd (2000); Trefethen (2000), where a vast number of examples are shown, including application of non-periodic boundaries using Chebyshev points.

3.4.2.2 Vertical integration

Vertical integration, in cases that include suspended sediment transport, is done with the trapezoidal rule using the Matlab functions `trapz` and `cumtrapz`. Due to the large near bed vertical gradients, the grid points are distributed logarithmically from the bed towards the surface.

Chapter 4

Validation

In this chapter the 2DH model is validated with two different cases. The first validation is a 1D case of a backfilling trench, used by Galappatti (1983) to validate his depth-averaged suspended load model. The second case is a 2D case of alternating bars in a laboratory flume conducted by Fujita and Muramoto (1985). The first case serves as a test of the implementation of the suspended load model, while the second case only includes bed load and serves as a test of the physical mechanisms that generate large-scale bedforms. These cases are of course of a smaller scale than the scales in the offshore environment that this thesis discusses, however, they provide confidence in that the model is able to simulate the physics correctly.

4.1 Backfilling of a trench

In the following, the model is, validated with measurements of a backfilling trench, which was conducted at Delft Hydraulics Laboratory DHL (1980) and used by Galappatti (1983) to validate his depth-averaged model. The experiment is labeled T3 in the referenced report. The setup constituted of a straight channel flume with a flow-through system where discharge was controlled by a circular weir. The dimensions of the flume were approximately 30 m length, 0.5 m width and 0.7 m depth. The flume bed was covered with sand grains of mean

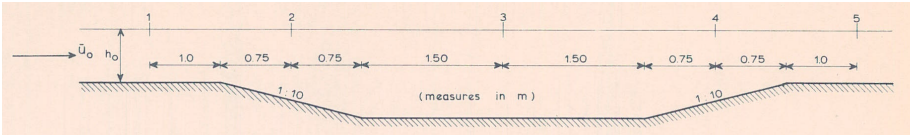

Figure 4.1: Sectional view of the trench used for the backfilling experiment T3 in DHL (1980). The figure includes the five locations where velocity and concentration profiles have been obtained.

diameter $d_{50} = 0.16$ mm and a 6 m wide trench with depth 15 cm and side slopes 1:10 was dug in the sand. This trench geometry yields a depth-to-wavelength ratio $0.39/12 = 0.036$, which is within the coverage of shallow water models. Fig. 4.1 shows a section of the trench in it's initial condition and five locations on the centerline, where velocity and sediment measurements were taken at the initial stage. To ensure equilibrium conditions on the flat bed, a constant nourishment of sediments in the upstream side was provided equal to 0.040 kg/(s·m), from which it was estimated that 0.030 kg/(s·m) was transported in suspension and 0.010 kg/(s·m) as bed load. Bed profiles at the trench were taken during the experiment and are available for the 7.5 and 15 hours timestamps. At no time was there any separation of the incoming flow. The mean grain diameter of the sediments that were transported in suspension was measured to be in the range 0.12–0.15 mm and with a fall velocity of 0.011–0.015 m/s. In the initially flat part of the bed, ripples started forming and reached lengths between 10–25 cm and heights 1.5–3.5 cm. These ripple dimensions led to an estimation of the total roughness height being $k_s = 0.025$. Tab. 4.1 shows the input parameters

Table 4.1: Parameter for T3 trench simulation.

Model	U_0 m/s	h_0 m	d_{50} mm	k_s m	T °C	w_s m/s	q_{b0} kg/(s·m)	q_{s0} kg/(s·m)
DHL1980	0.51	0.39	0.16	0.025	15	0.013	0.010	0.030
Galappatti	0.51	0.39	0.16	0.025	15	0.013	0.018	0.022
Mat2DH	0.56	0.39	0.16	0.025	15	0.017	0.020	0.020

used in the different simulation attempts of the experiment. None of the models account for side wall effects. DHL1980 used a 2DV model, while Galappatti and Mat2DH (the model used here) are depth-averaged models. Galappatti modelled the sediment transport with a simple relation of the form $q = a\bar{u}^b$, in which a and b are calibration constants. He found it necessary to adjust the incoming transport modes so that $q_{b0} = 0.018$ kg/(s·m) and $q_{s0} = 0.022$ kg/(s·m). The bottom boundary condition for the concentration equation (3.72) was applied at $z/h = 0.02667$. Galappatti simulated the backfilling using a quasi-steady model, which included consideration of the spatial gradients of Φ_0 and u_f, and

another simulation using a simpler restricted model. In the presented Mat2DH

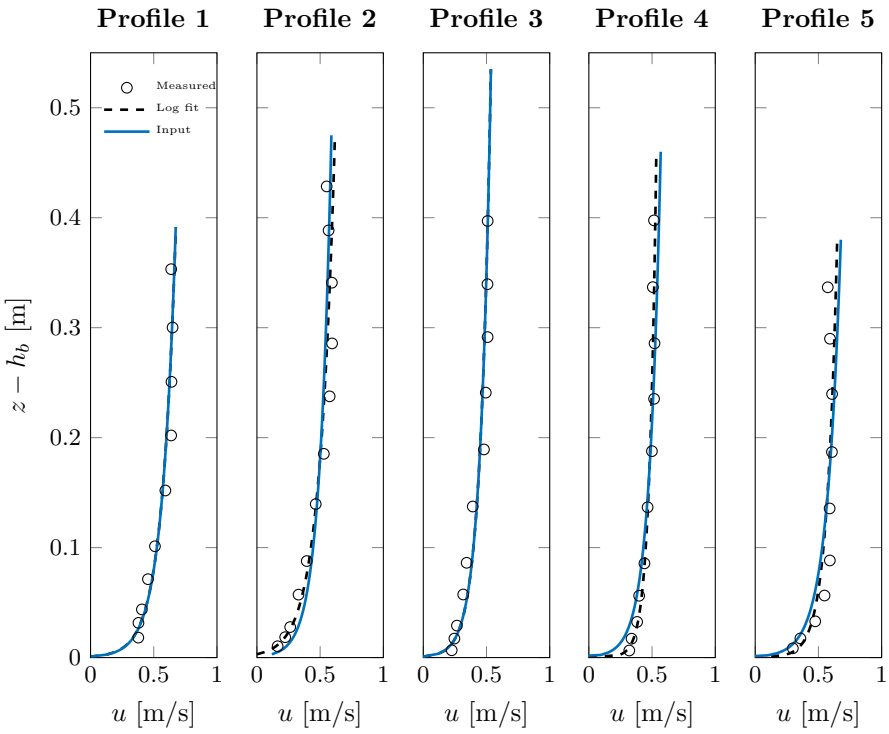

Figure 4.2: Velocity profiles in the five locations.

model more systematic approaches are used to estimate the sediment transport. Fig. 4.2 shows the measured velocity profiles at the initialization of the experiment. The profiles are fit using a log law expression (Eq. 3.27) through all measured points, whereby the input depth-averaged velocity is found to be approximately $U_0 = 0.56$ m/s. The roughness height k_s is set constant throughout the entire domain to match the velocity at of the incoming flow. Thus profiles further downstream may deviate from the fitted ones as seen in profiles 2, 4 and 5. The difference in the fall velocity w_s from the other cases, is due to it being calculated using Eq. (3.62) for the mean grain diameter of the bed and with viscosity $\nu = 1.135 \cdot 10^{-6}$ m^2/s corresponding to the reported water temperature of 15 °C. The critical Shields parameter is calculated using Eq. 3.20 to $\theta_c = 0.059$ in the equilibrium part (incoming flow), while θ' is estimated using Soulsby's approach (Eqs. 3.27–3.30). A test using the skin friction method of Einstein made it necessary to reduce the incoming velocity substantially. The reference value of the suspended load concentration c_b,is calculated explicitly at $2d_{50}$ above the bed, which is then projected to the no-slip level ζ_0 using a

Rouse profile. This leads to the equilibrium transport modes being $q_{b0} = 0.020$ kg/(s·m) and $q_{s0} = 0.020$ kg/(s·m). The justification for the adjustment of the incoming transport rates relative to the reported transports, can be explained as follows: The suspended load transport is based on an assumed velocity profile, which in the depth-averaged model has a no-slip level $\zeta_0 h$ that might be above $2d_{50}$. Hence, the suspended load does not get a contribution from between $2d_{50}$ and $\zeta_0 h$, where the concentrations are typically the highest. Therefore the bed load transport is increased to account for that missing part.

Since the model has periodic boundaries, the simulated stretch used is 256 m to ensure the flow and transports return to equilibrium in front of the trench. A uniform grid spacing $\Delta x = 0.25$ m is used. The results shown are with Kovacs & Parker's vectorial bed load correction over sloping beds, which gave a slightly better match than with Olesen's empirical correction. The flow is driven by a body force given by

$$S_x = \frac{C_{D0}}{h_0} U_o |U_o|, \quad S_y = 0 \tag{4.1}$$

where C_{D0} is calculated from Eq. (3.27) with $z_0 = k_s/30$. A hot-start was used in the simulation in order to bring the flow and transport fields to a steady state, where-after the bed was allowed to develop. The morphological evolution was sped up by amplifying the rate of bed level change by a factor $f_A = 100$. Fig. 4.3 shows the state of the flow and transport fields in the trench region just before the bed morphology is initialized. With a Froude number $U_0/\sqrt{gh_0} = 0.29$, the fluid velocity and surface elevation match the input values and the flow shows correct sub-critical characteristics above the trench. In the upstream side, the bed load and suspended load transport also match the inputs of q_{b0} and q_{s0}. It can be seen that the equilibrium concentration $\bar{c}_e$ and the instantaneous $\bar{c}$ match in the upstream side, which indicates that the boundary conditions of the concentration adapts correctly. The measured suspended load (uhc_{T3}) is also included at the five profile locations, marked with an $\times$. At the position of profile 1, the measured suspended load is as mentioned above $q_{b0} = 0.030$ kg/(s·m) which means that the bed load has to be $q_{b0} = 0.010$ kg/(s·m), to match the total load of 0.040 kg/(s·m). At the location of profiles 2–4, the measured suspended transport lays close to the simulated total load, from which it can be deduced that the bed load is most likely close to zero, in reality. At the position of the last profile 5, the simulation is missing the measured value by a great degree. The reason for the mismatch in profile 5 will be explained after examination of the following bed evolution figures. Fig. 4.4 shows the bed profiles after 7.5 hours and 15 hours. It can be seen that the model predicts the overall backfilling rate at a satisfactory manner. The upstream slope is predicted very accurately, while the model underestimates the erosion on the downstream slope. The reason for this is very clear when comparing the computed gradient of the sediment transport (and thereby $\partial h_b/\partial t$) with the gradient between the

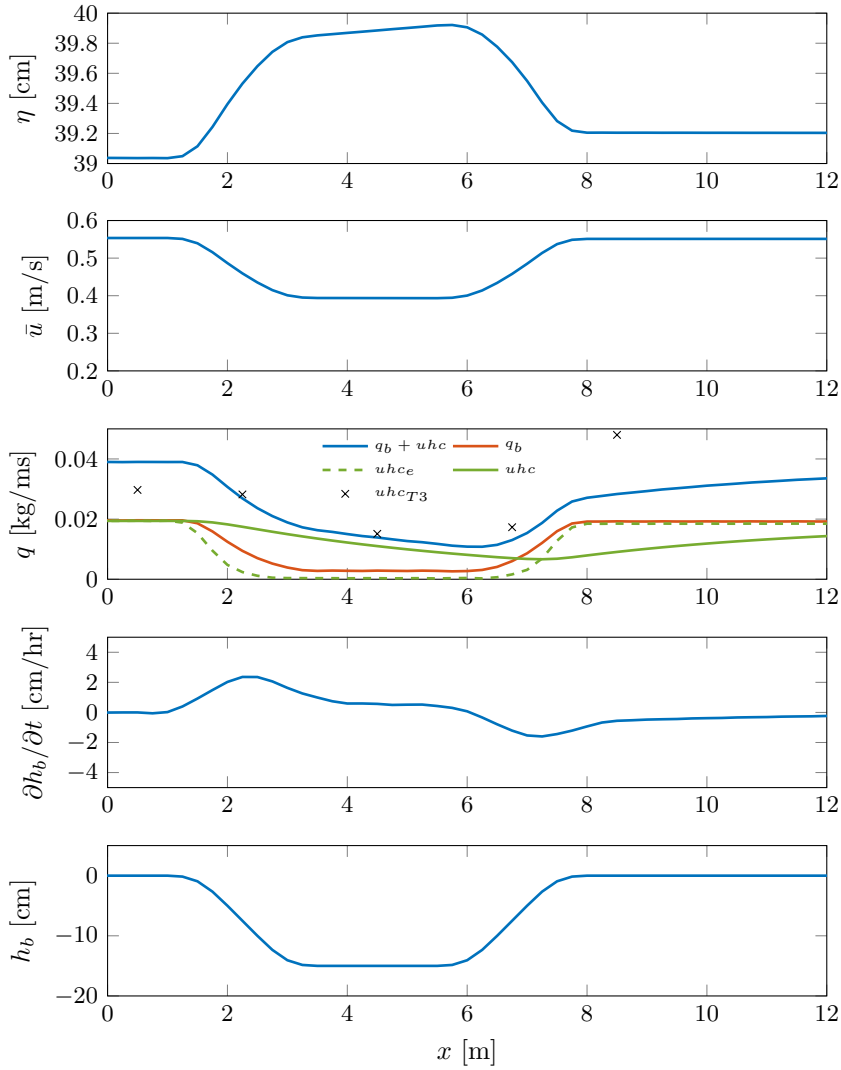

Figure 4.3: Initial state in the simulation before the trench backfilling begins.

measured transports at profiles 4 and 5, shown in Fig. 4.3. The reason for the deviation can be linked to Fig. 4.2, where the model velocities greatly underestimate the near bed velocity at profile 4. This underestimation is caused by the roughness k_s being constant in the domain, thus yielding an excessively high roughness with contracting streamlines, and with a higher no-slip level. Hence, both the concentration and the near bed velocity are greatly underestimated in

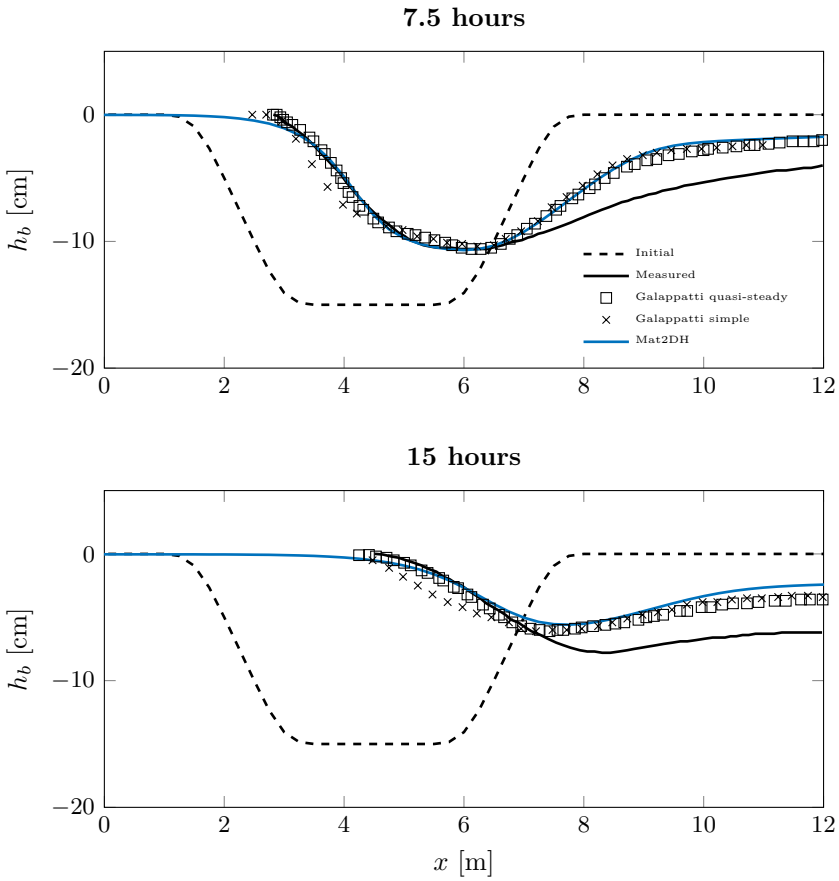

Figure 4.4: State of the trench after 7.5 hours and 15 hours.

the simulation, which then underestimates the suspended load. In reality the downstream side of the trench would experience a great degree of erosion.

Compared to the others, the model shows very similar results to Galappatti's quasi-steady model that includes gradients of Φ_0 and u_f, even though it is closer to Galappatti's restricted model in term of the transport equation. Thus it could suggest that the systematic approach used here for determining the equilibrium sediment transport gives a better result than Galappatti's power formulation, and thus allows neglecting the spatial gradients of Φ_0.

The approach used in this validation has been to minimize calibration of the sediment transports, and instead simply let the model predict the outcome, us-

ing only the parameters of the flow field, which are consistent with the available measurements. This approach is justified because it is nearly impossible to validate with the offshore environment. Therefore it is more methodological to obtain the behavior with a correct flow field in a measurable scale as was done here, and study the outcome without calibration. In conclusion, the implementation of the sediment transport model is robust and gets the overall backfilling rate correctly. The rate of bed level change $\partial h_b/\partial t$ does predict deposition at the upstream side and erosion at the downstream side. For large-scale simulations the slopes over the back of the bed forms are expected to be much gentler than the trench's slope, due to the bed wavelength being several orders of magnitude large than the water depth. Thus, on the basis of these considerations, it can carefully be concluded that for large-scale simulations this kind of accuracy should be sufficient.

4.2 Alternate bars in a flume

Another validation of the model is now conducted in 2D horizontal by simulating the laboratory experiment done by Fujita and Muramoto (1985). This case was also used for validation by Nelson (1990) and Madsen (2001). The experiment is labeled H-2 in the original work and constituted of a flume of approximately 20 m length, 0.5 m width, with a sandy bed which developed bars as a steady current was put through the tilting flume. Sediments were fed at the inlet to provide equilibrium. Tab. 4.2 lists the parameters of the experimental setup and Fig. 4.5 shows the resulting bar patterns at different times given in minutes and heights given in centimeters. The d_{50}/h_0 ratio is rather large in this case

Table 4.2: Parameters for H-2 simulation.

Q	U_0	h_0	d_{50}	u_f	θ	q_b
l/s	m/s	cm	mm	cm/s	–	cm^2/s
4.02	0.38	2.11	0.99	3.26	0.0657	0.021

and is not likely to be relevant other than for laboratory scales. The Froude number $U_0/\sqrt{gh_0} = 0.84$ is as a result also very high which can lead to areas in the flow where it will become supercritical due to the bedforms. The transition from sub- to supercritical flow can be difficult to simulate in numerical models and is the reason that Madsen (2001) ran an up-scaled version of the experiment using a Froude number of 0.084 and a lower d_{50}/h_0 ratio. In the present case however, the model has successfully been able to simulate the experiment using the original parameters. The grain diameter used is on the coarse side and the flow depth so shallow that suspended load is not likely to occur, and therefore

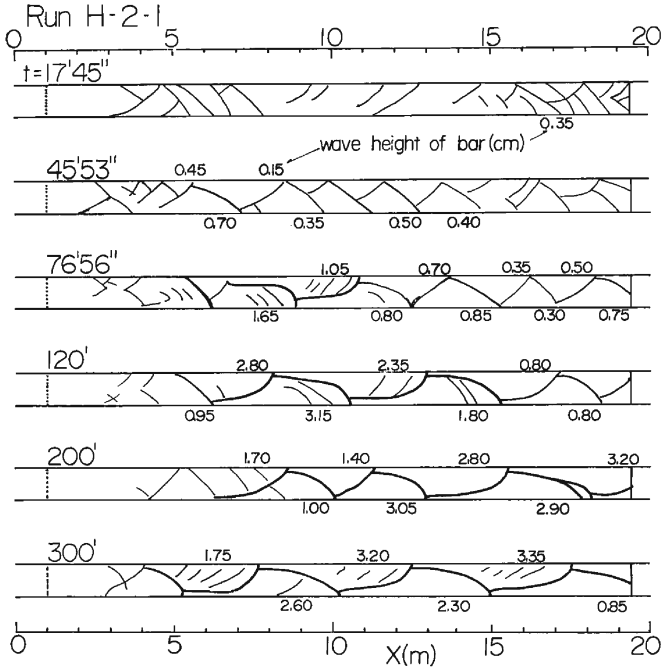

Figure 4.5: Illustration of the sand bars emerging in experiment H-2 from Fujita and Muramoto (1985).

it is not included in the simulation. Furthermore, at this depth the division into skin friction and form drag is not viable, hence the bed load is calculated directly from the total Shields parameter. The experiment measured an initial sediment transport through the outflow of 0.031 cm^2/s and an average of 0.021 cm^2/s for the entire 300 minutes that the experiment lasted.

For straight channels Fredsøe (1978) has shown that there are three possible outcomes with regards to the development of large-scale bedforms. The transverse wavenumber of the bedforms is defined as $k_y = m\pi/W$, where W is the channel width and m is an integer. A linear stability analysis can then be conducted from which if all k_y's are stable, the channel will remain straight. However, if the most unstable mode is found with $m = 1$, the channel generates an alternate bar pattern which may lead to meandering, while most unstable modes with $m \geq 2$ will create a braiding pattern. Fredsøe (1978) found the governing parameters that determine the outcome to be the width-to-depth ratio (W/h) and the Shields parameter θ. In Fujita and Muramoto's (1985) experiment the width-to-depth ratio is 23.7 and the Shield's parameter 0.0657, with the result

of alternate bars, i.e. $m = 1$. Hence, the transverse bedform will constitute of half a wavelength with symmetry at the lateral boundaries. Since the model is built with periodic boundaries and driven with a body force it has to be setup with a different geometry than the experimental. The length of the channel is set to 9.5 m, which is intended to represent the stream-wise stretch between 5.5–15 m as seen in Figure 4.5 and a width of 1 m, since the experiment yielded half a wavelength at 0.5 m. The sediment transport was calibrated to match 0.021 cm^2/s by using a fixed value for the critical Shields parameter of 0.056, rather than calculating it. The helical flow is used with an adaption factor of $a_s = 1.2$, which was found most suitable.

In a numerical simulation such as the present, a completely flat bed will not initiate any growth, so a perturbation of the variables is necessary to "kick-start" the bed development. There can be several ways to achieve this. In the next chapter a linear stability analysis is conducted by perturbing the bed with a doubly periodic sinusoidal function in order to be able to analyze the result and obtain growth and migration rates. This approach prescribes a certain wavenumber set on the flow, thus can have a tendency to make the bed prefer this mode simply because it was introduced to the system. Alternatively, as Madsen did, it is possible to introduce a small hump in the domain and let the bed evolve from that local disturbance. Initially the hump is getting washed away so the bed is stabilized, but enough perturbation has been introduced in the system so the unstable modes start to kick in and the bars develop. This hump method is better than the sinusoidal approach but can still affect the preferred modes as the hump size could effect the unstable growth lengths. The best approach is to have a tiny random noise introduced into the system and then allow it to develop from that into some clear bed features. Such a noise, however, can be very difficult for numerical simulations because it introduces numerical instability but in the present model it is possible with the spectral method. The simulation of the flume was thus initiated with a perturbation of the flat bed consisting of a normal distributed random noise generated with the Matlab function `randn` with amplitude $A/h_0 = 0.001$. The simulation has been run without a morphological speed up factor, i.e. real time.

Figure 4.6 shows the time development of the maximum (max) bed value as well as the root mean square (rms) value of the entire bed. Figures 4.8 and 4.9 show a chronological series of the bed at different times of the simulation, through a longitudinal section and a top view, respectively. The evolution that the bed undergoes in the simulation is as follows: Initially the noisy flat bed forms organized patterns, resembling three doubly periodic sinusoidal shapes, while remaining nearly flat. Next, these shapes grow rapidly and morph into elongated alternate bedforms with a nonlinear shape, and lastly, the growth is tapered and the bedforms primarily migrate down-steam with interactions that cause them to merge and elongate. The bed continues to grow at a lower

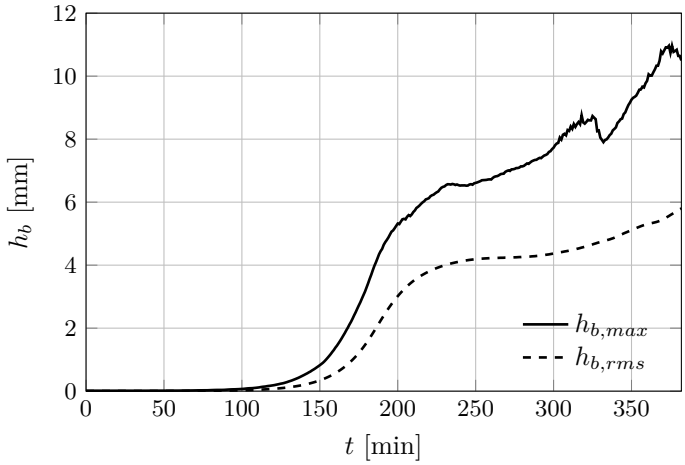

Figure 4.6: Maximum and root mean square bed values during the simulation.

rate until the simulation blows up at 382 minutes, due to the flow becoming critical in some regions. In the end of the simulation the number of streamwise waves in the domain has gone down from three to nearly two, while one wave in the transverse direction is maintained throughout the entire simulation. The evolution can thus be described by three phases: 1) appearance of organized pattern on the bed with minimal growth, 2) exponential growth of linear sinusoidal patterns, and 3) decay of the growth as the bedforms approach equilibrium. Fujita and Muramoto (1985) reported that the bars in the experiment underwent their primary growth up until the 200 minutes timestamp, where after they consolidated and migrated until the experiment was stopped at the 330 minutes timestamp. When comparing the development time between the experiment and the simulation it can be "tricky" to determine the time at which the bed starts growing. $h_{b,max}$ and $h_{b,rms}$ show that the primary growth is decayed at around 250 minutes in the simulation, from which it can be deduced that the first 50 minutes include processes that are not entirely representative of the physical phenomena. The period of rapid growth, on the other hand, seems to have resembled the experiment remarkably well. In the experiment some dry areas emerged, hence, the simulation blow up does not mean that it is wrong, only that it is lacking the ability to incorporate dry areas.

It can be seen that the bars varied their longitudinal length during the experiment, while growing and migrating down-stream. The height of the bars in the experiment along the boundaries is higher than the simulation results and the depth of the troughs is not clear. Part of this deviance can be attributed to the periodic boundaries and their effect on the sediment transport and resulting

morphology, as well as the extreme shallowness of the experiment which cause the bedforms to penetrate through the surface. Thus, to conclude, this validation can be considered successful since other than the difference in the bar heights, the time and length scales as well as the shapes observed on the top view, resemble to a large extent the measurements in the experiment.

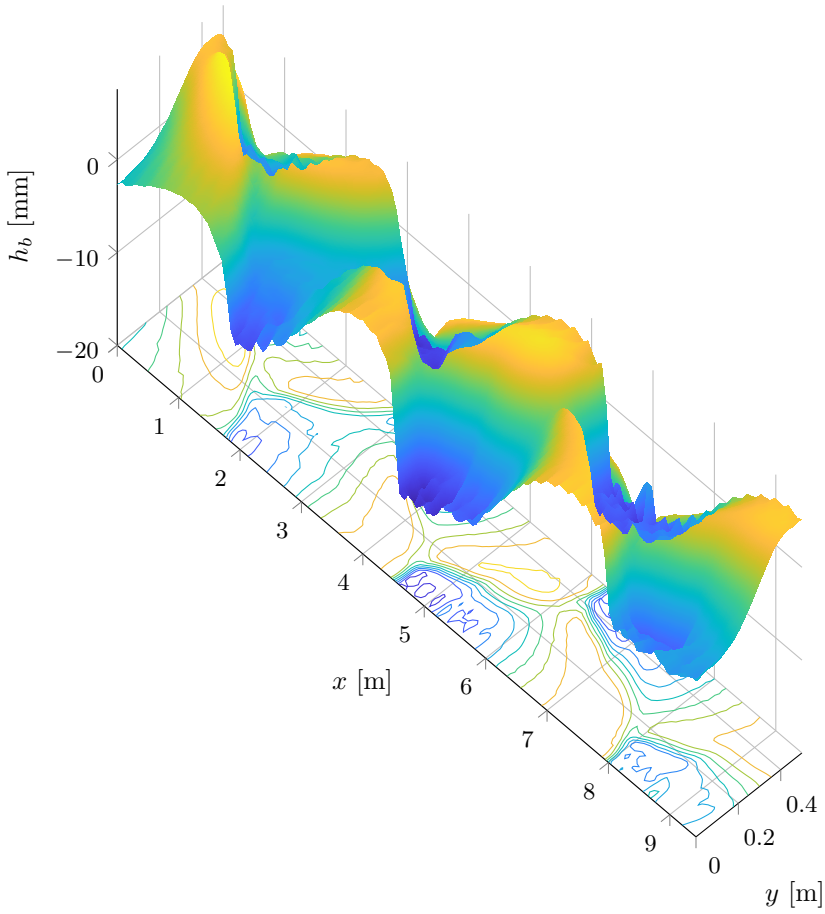

Figure 4.7: 3D view of the bed at $t = 300$ min.

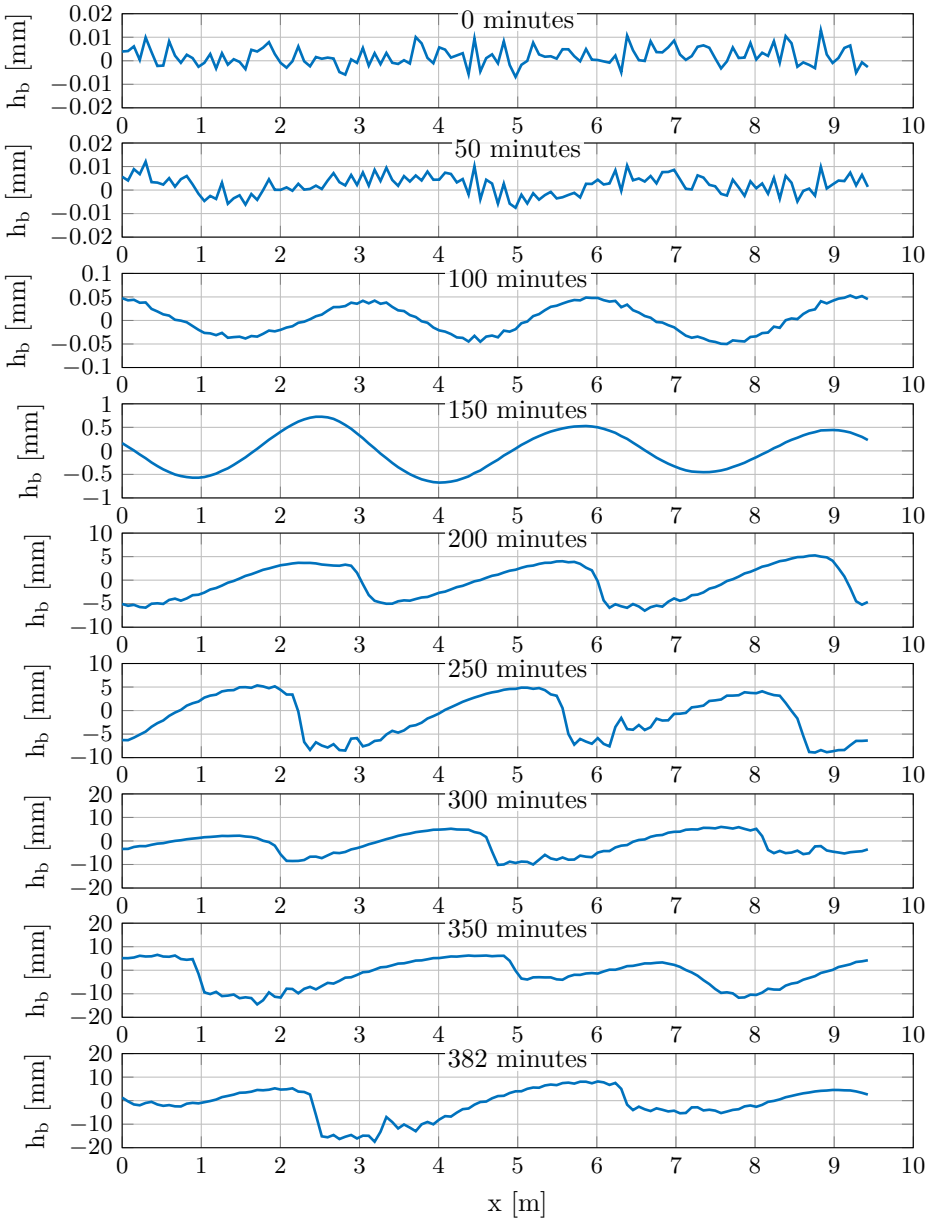

Figure 4.8: Longitudinal section profiles of the bed through the bars peaks.

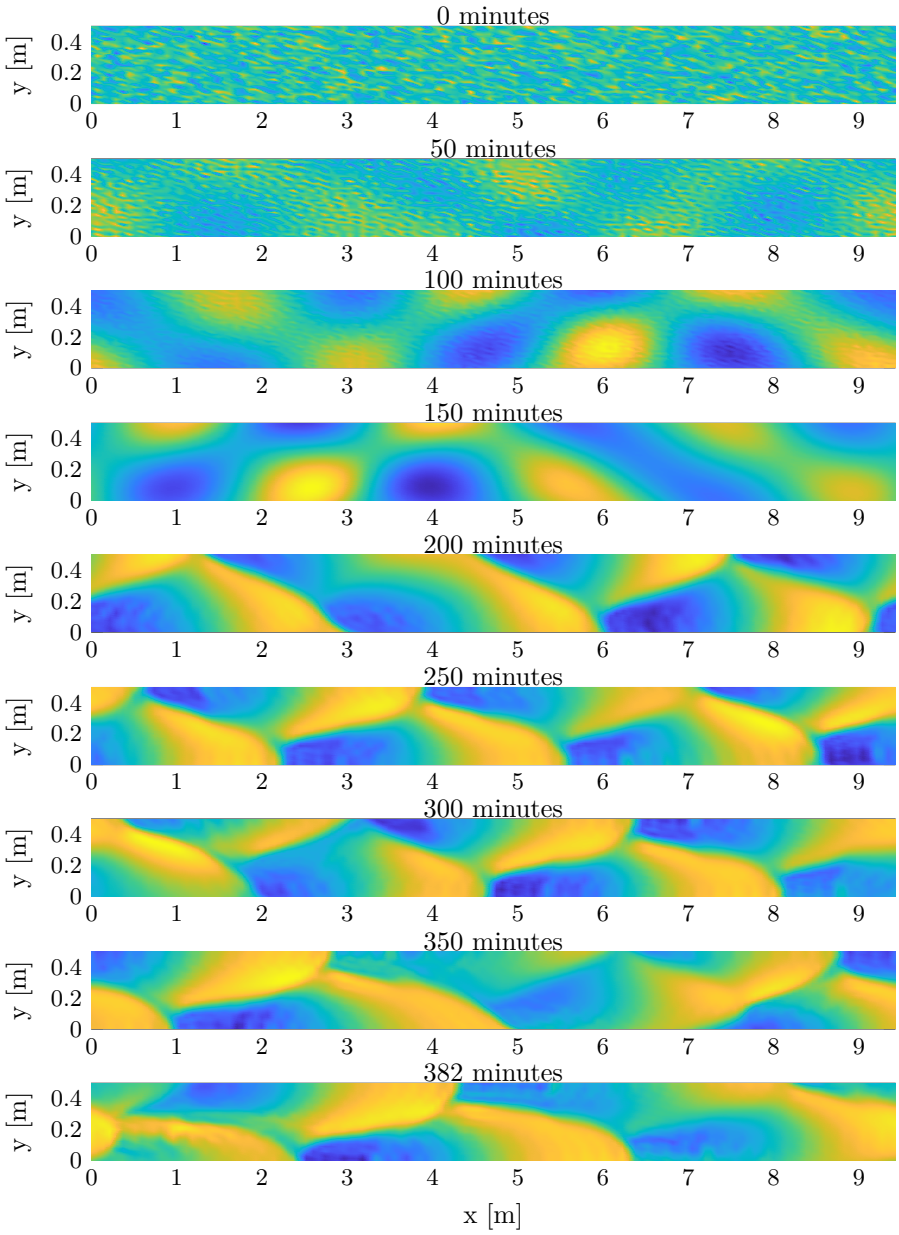

Figure 4.9: Top view of the morphing bed. Blue indicates deeper areas while yellow indicates shallower areas.

Chapter 5

Linear stability analysis

In this chapter a linear stability analysis is conducted in order to study the parameters leading to the development of sandbanks. Most of the reviewed literature included analytical stability analyses, which are considered elegant and fast but usually require the use of linearization and simplifications in the governing equations. Conducting the stability analysis in a numerical model allows maintaining the full set of equations, as they would be used in a morphological model. The disadvantage is that it requires a large number of individual simulations to cover the desired parametric ranges.

The study is done numerically with the 2DH model, hence all effects are included and the equations are not linearized. The sensitivity of the growth rates to the flow velocity and resistance as well as sediment grain size is parametrized. The study is both for bed load alone as well as in combination with suspended load. The results give both quantitative and qualitative predictions, which can serve as inputs and comparison for a morphologic study, as done in the following chapter.

Parts of this chapter have been published as Margalit and Fuhrman (2017) and submitted to a journal as Margalit et al. (2018).

5.1 Mathematical background

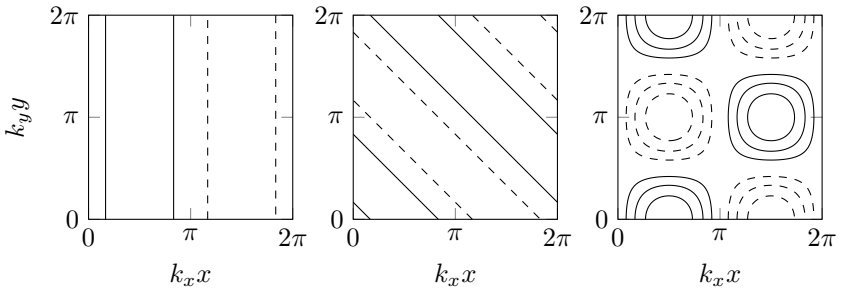

Figure 5.1: Examples of sinusoidal bedform perturbations. Solid line: crest area, Dashed line: trough area. Left: 1D, Center: 1D inclined, Right: 2D

The natural irregularities leading to the generation of bedforms discussed in Chapter 2, need to be forcefully imposed in the model in order to replicate the behavior. The numerical linear stability analysis is done by perturbing the (otherwise flat) bed and studying the response of the flow-bed system. The simplest way to apply the perturbation is by assuming a bed given by a periodic sinusoidal function such as

$$h_b = A\sin(k_x x + k_y y) \tag{5.1}$$

where A is the amplitude of the perturbation and k_x, k_y are the wavenumbers in x and y, respectively. This function is pictured in Fig. 5.1 as the 1D inclined perturbation in the center.

In order to analyze the initial response of the bed to a perturbation, Eq. (5.1) is assumed to result in a time development involving growth and migration given by

$$h_b(x, y, t) = h_{b0} + Ae^{\Omega t}\sin(k_x x + k_y y - \omega_b t) \tag{5.2}$$

where h_{b0} is the unperturbed (flat) bed, Ω is the growth rate and ω_b is the angular migration frequency. Taking the time derivative of Eq. (5.2) yields

$$\frac{\partial h_b}{\partial t} = Ae^{\Omega t}\left(\Omega\sin(k_x x + k_y y - \omega_b t) - \omega_b\cos(k_x x + k_y y - \omega_b t)\right) \tag{5.3}$$

The initial response used in the stability analysis is found at $t = 0$, which yields

$$\left.\frac{\partial h_b}{\partial t}\right|_{t=t_0=0} = A\left(\Omega\sin(k_x x + k_y y) - \omega_b\cos(k_x x + k_y y)\right) \tag{5.4}$$

Bed forms are considered stable when the growth rate $\Omega \leq 0$ (no bedforms emerge) and unstable when $\Omega > 0$ (bedforms emerge). This is determined by perturbing the bed for a large set of wavenumbers k_x, k_y and given flow conditions.

Mathematically from the above, the growth rate can now be found at the peak of the bedform

$$\frac{1}{A}\left.\frac{\partial h_b}{\partial t_0}\right|_{(x,y)=(\frac{\pi}{2k_x},0)} = \Omega \tag{5.5}$$

and the migration rate at the zero crossing

$$-\frac{1}{A}\left.\frac{\partial h_b}{\partial t_0}\right|_{(x,y)=(0,0)} = \omega_b \tag{5.6}$$

To relate the above to the sediment transport, consider an example where the transport is given by

$$q = q_0 + A_q \sin(k_x x + k_y y + \phi) \tag{5.7}$$

where q_0 is the unperturbed transport, A_q is the perturbed transport amplitude and ϕ is a phase. Using trigonometric identities this becomes

$$q = q_0 + A_q \left(\sin\phi\cos(k_x x + k_y y) + \cos\phi\sin(k_x x + k_y y)\right) \tag{5.8}$$

Insertion of the transport into the Exner equation (3.89) yields

$$\begin{aligned}\frac{\partial h_b}{\partial t} &= -\frac{1}{1-\varepsilon_p}\left(\frac{\partial q}{\partial x} + \frac{\partial q}{\partial y}\right) \\ &= \frac{A_q(k_x + k_y)}{1-\varepsilon_p}\left(\sin\phi\sin(k_x x + k_y y) - \cos\phi\cos(k_x x + k_y y)\right)\end{aligned} \tag{5.9}$$

From Eqs. (5.9) and (5.4) it can be recognized that

$$\Omega = \frac{A_q(k_x + k_y)}{A(1-\varepsilon_p)}\sin\phi \tag{5.10}$$

$$\omega_b = \frac{A_q(k_x + k_y)}{A(1-\varepsilon_p)}\cos\phi \tag{5.11}$$

Thus the bedform will grow when there is a positive phase between the transport and the bed $(0 < \phi < \pi) \rightarrow \Omega > 0$, and decay when the phase is negative $(-\pi < \phi < 0) \rightarrow \Omega < 0$, or possibly maintain the level and experience pure migration when $(\phi = 0)$ or $(\phi = \pi) \rightarrow \Omega = 0$. Notice that the migration could also be in the opposite direction of the flow.

Due to numerical uncertainty in using results from a single point on the grid as suggested by Eq. (5.5), the growth and migration rates are found using the results from the entire grid. The problem can be formulated as an overdetermined system of equations, solved by the matrix equation

$$\mathbf{M}\begin{bmatrix}\Omega\\ \omega_b\end{bmatrix} = \boldsymbol{p} \tag{5.12}$$

where

$$\mathbf{M} = A\begin{bmatrix} \sin(k_x x_{1,1} + k_y y_{1,1}) & -\cos(k_x x_{1,1} + k_y y_{1,1}) \\ \sin(k_x x_{2,1} + k_y y_{2,1}) & -\cos(k_x x_{2,1} + k_y y_{2,1}) \\ \vdots & \vdots \\ \sin(k_x x_{1,2} + k_y y_{1,2}) & -\cos(k_x x_{1,2} + k_y y_{1,2}) \\ \sin(k_x x_{2,2} + k_y y_{2,2}) & -\cos(k_x x_{2,2} + k_y y_{2,2}) \\ \vdots & \vdots \\ \sin(k_x x_{n_x,n_y} + k_y y_{n_x,n_y}) & -\cos(k_x x_{n_x,n_y} + k_y y_{n_x,n_y}) \end{bmatrix} \tag{5.13}$$

$$\boldsymbol{p} = \begin{bmatrix} \frac{\partial h_b}{\partial t_0}_{1,1} \\ \frac{\partial h_b}{\partial t_0}_{2,1} \\ \vdots \\ \frac{\partial h_b}{\partial t_0}_{1,2} \\ \frac{\partial h_b}{\partial t_0}_{2,2} \\ \vdots \\ \frac{\partial h_b}{\partial t_0}_{n_x,n_y} \end{bmatrix} \tag{5.14}$$

where n_x,n_y are the number of grid points in x and y, respectively.

The asymmetry that the Coriolis effect introduces, means that each problem has to be simulated with both a positive and a negative wavenumber k_y. Instead of running two separate simulations, a perturbation given by the superposition of two functions given by Eq. (5.1) with an opposite sign of k_y is introduced as

$$h_b = \frac{A}{2}\left(\sin(k_x x + k_y y) + \sin(k_x x - k_y y)\right) \tag{5.15}$$

which is depicted in Fig. 5.1 on the right. Within the linear response regime this superposition is viable and the solution may be decomposed into the two original functions linearly, thus obtaining both solutions from a single simulation (which has been confirmed via independent testing). Additionally, the symmetrical doubly periodic setup has shown to yield greater numerical stability than the asymmetrical option.

In the linear stability analysis, the bed is not allowed to morph and therefore the response of the bed to the flow is found in post-processing by inserting the solution of the sediment transport field into Eq. (3.89). The recipe for determining the growth and migration rates is thus: 1) the bed is perturbed using Eq. (5.15), 2) the flow is simulated over the bed until equilibrium is reached and the initial bed response is determined by Eq. (3.89), 3) $\partial h_b/\partial t$ found previously is inserted in Eq. (5.4), plus it's equivalent with negative k_y, and 4) the system is solved for Ω and ω_b, for each perturbation.

5.2 Dimensional analysis

A dimensional analysis is conducted on the model equations, which identifies the independent variables and reduces the complexity of the physical problem. The aim is to arrive at a smaller set of independent variables, which will be used to parameterize the problem in a global way.

The dimensional analysis is based on the Buckingham-Π theorem, which states that any physical process defined as

$$f(Q_1, Q_2, Q_3, \ldots, Q_m) = 0 \tag{5.16}$$

with Q_i being an m number of physical variables, consisting of j number of units, can be reduced into the set of dimensionless variables given by

$$F(\Pi_1, \Pi_2, \Pi_3, \ldots, \Pi_{m-j}) = 0 \tag{5.17}$$

The independent variables in the model are listed in Tab. 5.1. The density could in principle also be included in the independent variables, however, no density gradients are included in the model and it is implicitly included through the friction velocity u_f and the relative density ϱ. The fall velocity w_s is not independent since it is derived from d_{50}, g, ϱ and ν.

The rate of bed level change is a function of the following independent variables in the governing equations

$$\frac{\partial h_b}{\partial t} = f\left(U_0, h_0, C_{D0}, g, d_{50}, f_c, \nu, \varrho, \alpha_s, A, k_x, k_y\right) \tag{5.18}$$

where the zero subscripts refer to unperturbed values. The variables only include two fundamental dimensions, namely time and length. According to the Buckingham-Π theorem, it is thus possible to reduce the problem of 10 dimensional and 3 non-dimensional variables to 11 non-dimensional variables. The

Table 5.1: Independent variables of the model.

Name	Variable	Unit
Flow velocity	U	m/s
Flow depth	h	m
Bed level	h_b	m
Drag coefficient	C_D	-
Gravitational acceleration	g	m/s^2
Mean grain diameter	d_{50}	m
Coriolis parameter	f_c	rad/s
Kinematic viscosity	ν	m^2/s
Sediment relative density	ϱ	-
Helical adaption length constant	α_{sf}	-
Perturbation amplitude	A	m
Wavenumber in x	k_x	1/m
Wavenumber in y	k_y	1/m

problem may thus be formulated as

$$\frac{1}{\sqrt{gh_0}}\frac{\partial h_b}{\partial t} = F\left(Fr, C_{D0}, \frac{d_{50}}{h_0}, Ro, Re, \varrho, \alpha_s, \frac{A}{h_0}, k_x h_0, k_y h_0\right) \tag{5.19}$$

where $Fr = U_0/\sqrt{gh_0}$ is the Froude number, $Ro = U_0/(h_0 f_c)$ is the Rossby number and $Re = U_0 h_0/\nu$ is the Reynolds number. The assumption of an initially linear bed response, means that the amplitude A can be used as a linear multiplier of the rate of bed level change. Hence Eq. (5.19) is written as

$$\Omega^* = \frac{1}{A}\sqrt{\frac{h_0}{g}}\frac{\partial h_b}{\partial t} = F\left(Fr, C_{D0}, \frac{d_{50}}{h_0}, Ro, Re, \varrho, \alpha_s, k_x h_0, k_y h_0\right) \tag{5.20}$$

Note that this is equal to a non-dimensionalized growth rate as described by Eq. (5.5). It is common to see in literature the use of the unperturbed sediment flux and a separation of various time scales when non-dimensionalizing the growth rates to yield a growth amplification,

$$\Omega^* = \frac{h^2}{Aq_0}\frac{\partial h_b}{\partial t_0} \tag{5.21}$$

Such an approach is suitable for a pure study of the stability mechanisms, while this work is intended to relate realistic sea states to the emergence of large scale bedforms, with all solved in real time. Also note that Fr, C_{D0} and d_{50}/h_0 could be interchanged with θ, yielding

$$Fr^2 = (\varrho - 1)\frac{d_{50}}{h_0}\frac{\theta}{C_{D0}} \tag{5.22}$$

however, the set of parameters in Eq. (5.20) is convenient as it allows the choice of depth, velocity, drag coefficient and grain diameter to be based on field measured values.

5.3 Model configuration and verification

The flow is driven by imposing a body force in the flow Eqs. (3.2)-(3.3), such that the depth averaged velocities yield a flow symmetric around the x axis given by

$$\bar{u} = U_0 = U_c + U_m \sin(\sigma_2 t) \tag{5.23}$$

$$\bar{v} = 0 \tag{5.24}$$

where U_c is the steady current velocity, U_m is the tidal velocity amplitude and σ_2 the tidal frequency. The body force $\boldsymbol{S} = [S_x \ S_y]^T$ is defined by

$$\begin{aligned} S_x =& U_m \sigma_2 \cos(\sigma_2 t) \\ &+ \frac{C_{D0}}{h_0} \left(U_c + U_m \sigma_2 \sin(\sigma_2 t)\right) \sqrt{\left(U_c + U_m \sigma_2 \sin(\sigma_2 t)\right)^2} \end{aligned} \tag{5.25}$$

$$S_y = f_c \left(U_c + U_m \sigma_2 \sin(\sigma_2 t)\right) \tag{5.26}$$

C_{D0}, h_0, f_c, U_c, U_m and σ_2 are given as input parameters for the model. For an M2 tide the radial frequency is $\sigma_2 = 1.4052 \cdot 10^{-4}$ rad/s. The Coriolis frequency is calculated from

$$f_c = 2\Omega_c \sin\varphi \tag{5.27}$$

where φ is the latitude and $\Omega_c = 7.2921 \cdot 10^{-5}$ rad/s is Earth's rotational frequency. Note that the model does not account for varying water depths induced by a real tidal flow.

Soulsby (1997) gives an equation that estimates the boundary layer height in a tidal flow

$$\delta = 0.0038 \left(\frac{U_a \sigma_2 - U_b f_c}{\sigma_2^2 - f_c^2} \right) \tag{5.28}$$

where U_a and U_b are values of the depth-averaged current speed through a tidal cycle, with U_b being negative in a clockwise tide and zero at a rectilinear tide. This is though not utilized in the model, whereby the current profile is assumed fully developed at all times.

In the following the convergence of the growth rate (with grid refinement) and the additional assumption of an initially linear growth rate with amplitude A/h_0 are studied. The parameters selected for consideration are $Fr = 0.06$, $C_{D0} = 0.00459$, $d/h_0 = 8.33 \cdot 10^{-6}$, $k_x h_0 = 0.01$, $k_y h_0 = 0.01$.

5.3.1 Convergence

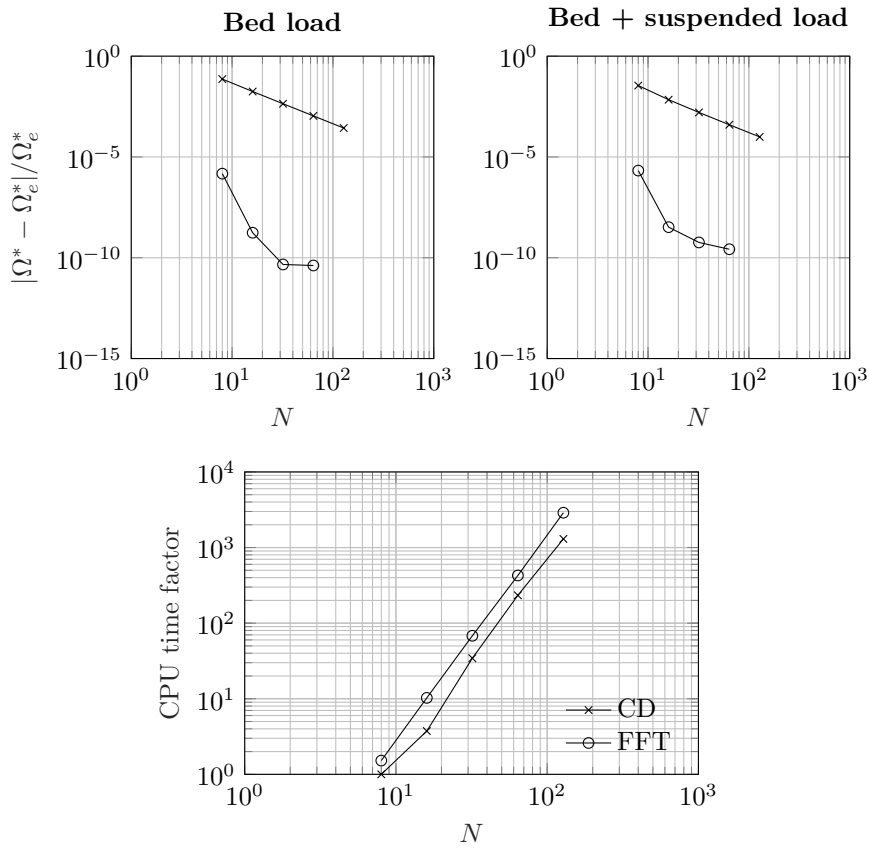

Figure 5.2: Comparison between the Finite difference central difference scheme (CD) and the spectral method (FFT). The absolute error of the non-dimensional growth rate and computational time. Left: Bed load alone, Center: Bed load and suspension load. Right: Computation times. The absolute error is relative to Ω_e^*, which is the non-dimensional growth rate found using the spectral method with $N = 128$. ($Fr = 0.06$, $C_{D0} = 0.00459$, $d/h_0 = 8.33 \cdot 10^{-6}$, $k_x h_0 = 0.01$, $k_y h_0 = 0.01$)

The rate of convergence due to grid size is checked. The spectral scheme is compared with a second-order finite difference central difference scheme. Fig. 5.2 shows the non-dimensional growth rate and computational time factor vs. the number of grid points N used for discetization in each horizontal dimension, i.e. number of grid points per bed wavelength. The absolute error is relative to the

error found having the spectral method with the highest number of grid points $N = 128$. The spectral method demonstrates its large advantage over the finite difference scheme as the solution is fairly accurate with as few as eight grid points resolving the bedform. The computation time spent using the spectral method is higher than the central difference for a given domain size, however the superior accuracy of the solution with a small number of elements outweighs it. It can be seen that when suspended sediment transport is included, the accuracy is reduced compared to the bed load alone. This is due to the vertical integration of the concentration profiles, which is only accurate up to second order, thus limiting the efficiency of the spectral method. It is however substantially better than all the results produced by the finite difference scheme. Based on this analysis it is justified to conduct all further linear stability simulations with the spectral method using $N = 16$ grid points to resolve the bed wave in each direction.

5.3.2 Linear behaviour

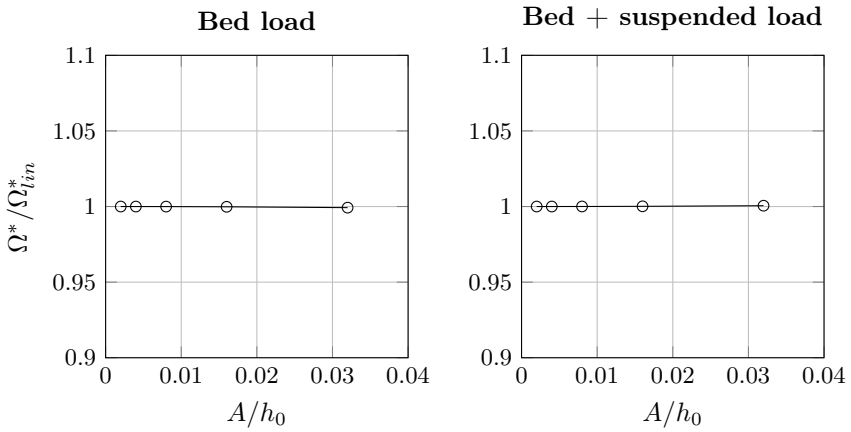

Figure 5.3: Growth rate normalized by growth rate Ω_{lin} (i.e. Ω with $A/h_0 = 0.001$). Left: Bed load only, Right: Bed load and suspended load. ($Fr = 0.06$, $C_{D0} = 0.00459$, $d/h_0 = 8.33 \cdot 10^{-6}$, $k_x h_0 = 0.01$, $k_y h_0 = 0.01$)

The linear assumption of the stability analysis on Ω^* is now validated for a range of small amplitudes A/h_0. Fig. 5.3 shows the non-dimensional growth rate when the perturbation amplitude is varied in the range $0.001 \leq A/h_0 \leq 0.032$. Both the bed load alone and the combined bed and suspended load models appear to yield linear responses up to roughly $A/h_0 = 0.016$. In literature a common linear

perturbation amplitude in analytical stability analyses is chosen as $A/h_0 = 0.01$. Based on the literature and the present results a perturbation amplitude of $A/h_0 = 0.01$ is used in further simulations in this chapter, as it gives a margin of safety to be within the linear response regime, while not being so low that numerical uncertainties might interfere with the solution. As another check, Fig. 5.4 shows the difference between the input unperturbed Froude number Fr_{in} and the actual Froude number during a simulation $Fr(t)$, divided by the square of A/h_0, for a steady current and a tidal flow. It can be seen that after a short warm-up period the perturbed field in the steady current case attains a constant value and differences are of higher order, thus negligible for the linear stability analysis. The tidal current, having the same initial conditions as the steady current, needs to run for two periods before the results can confidently be considered in the linear regime. The convergence and linearity verifications have been conducted using a steady current flow. A comparison between the effects of a steady current and a tidal flow is discussed in the next section.

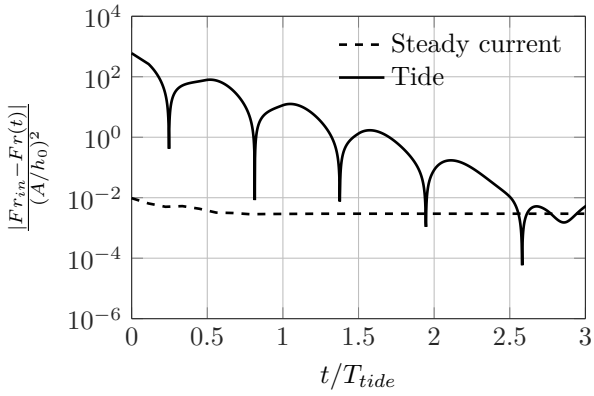

Figure 5.4: Ratio of the perturbed Froude number and the squared non-dimensionalized perturbation amplitude, during simulation.

5.4 Parametric study

The results of a parametric study are presented in this section. Based on the dimensional analysis, a parameter space defined in Tab. 5.2 is generated with different values of the unperturbed Froude number Fr, drag coefficient C_{D0} and non-dimensionalized grain diameter d/h_0. Fr is chosen such that the flow velocities resemble the amplitude of a unidirectional principal lunar semi-diurnal constituent (M2 tide), using a steady current, i.e. $U_m = 0$, $U_c = 0.5 - 1.5$ m/s.

The consequences of this simplification are studied in the following subsection. C_{D0} is based on empirical values in the range 0.001-0.01, where the lower limit resembles an almost plane bed. The input value of C_{D0} is used to calculate a z_0 roughness height through Eq. (3.27), which then serves as a constant input to the model, while a perturbed C_D emerges due to the variations in h. d_{50}/h_0 is based on sediment sizes within the range of very fine to coarse sand, corresponding to $d_{50} = 0.125$ mm, $d_{50} = 0.250$ mm and $d_{50} = 0.500$ mm. The friction Shields parameter θ'_0, Rouse number Z_0 and non-dimensional sediment transports

$$\Phi_{b0} = \frac{|q_{b0}|}{\sqrt{(\varrho - 1)g d_{50}^3}} \quad , \quad \Phi_{s0} = \frac{|q_{s0}|}{\sqrt{(\varrho - 1)g d_{50}^3}} \tag{5.29}$$

of the equivalent unperturbed case are also listed for each case for completeness and repeatability. Cases A1,B1 and C1 represent the lowest possible Φ_{s0}/Φ_{b0} ratios for each group. For each case an array of the wavenumbers have been simulated and contour plots of the growth rate generated. In order to ensure that the non-dimensional parameters resemble values of realistic ranges, all cases have been run with the viscosity $\nu = 1.3 \cdot 10^{-6}$ m^2/s, the mean depth $h_0 = 30$ m, the gravitational acceleration $g = 9.81$ m/s^2, the relative density $\varrho = 2.65$ and Coriolis frequency $f_c = 1.1947 \cdot 10^{-4}$ rad/s corresponding to latitude 55°. The helical flow adaption length coefficient is $\alpha_s = 1.2$ for all cases unless otherwise specified. The critical Shields parameter is calculated using Eq. (3.18) and the skin friction velocity is calculated using Soulsby's method, unless specified otherwise. In order to generate smooth growth rate contours in the wavenumber space, 400 wavenumber combinations were simulated for each tested case. This was achieved by the use of a HPC cluster, where each simulation was allocated to a single core, totaling more than 10,000 simulations for the generation of the results presented herein.

In the following five subsections, a single parametric setup, based on case B3 and listed in Tab. 5.3, has been used to preliminarily study isolated effects: 1) using a steady current vs. a tidal current, 2) the bed slope effect, 3) the helical flow effect, 4) the skin friction model effect, and 5) the type of suspended sediment module used (Equilibrium/Non-equilibrium). Lastly, subsection 6) present the results combined for all cases listed in Tab 5.2.

5.4.1 Steady current vs. tidal current

To recap from Chapter 2, bedforms emerging due to an interaction with a tidal current, are in the literature (Huthnance, 1982; de Vriend, 1990; Hulscher, 1996) studied by averaging the sediment transport over a full tidal cycle to yield the growth rate in a linear stability analysis. The Coriolis effect creates an

Table 5.2: Parameter list.

Case	d_{50}/h_0 ($\times 10^{-6}$)	Fr	C_{D0} ($\times 10^{-3}$)	θ_0'	Z_0	Φ_{b0}	Φ_{s0}	Φ_{s0}/Φ_{b0}
A1	4.17	0.03	0.850	0.11	1.66	0.025	0.002	0.07
A2	4.17	0.03	2.284	0.11	1.01	0.025	0.013	0.50
A3	4.17	0.03	2.760	0.11	0.92	0.025	0.025	1.00
A4	4.17	0.03	3.338	0.11	0.84	0.025	0.050	2.00
A5	4.17	0.06	0.857	0.44	0.83	2.28	57	25
A6	4.17	0.06	1.065	0.44	0.74	2.28	114	50
A7	4.17	0.06	1.333	0.44	0.66	2.28	228	100
A8	4.17	0.06	1.691	0.44	0.59	2.28	456	200
B1	8.33	0.06	1.781	0.24	1.69	1.25	0.10	0.08
B2	8.33	0.06	3.821	0.24	1.15	1.25	0.63	0.50
B3	8.33	0.06	4.590	0.24	1.05	1.25	1.25	1.00
B4	8.33	0.06	5.511	0.24	0.96	1.25	2.50	2.00
B5	8.33	0.09	3.505	0.54	0.80	3.00	74	25
B6	8.33	0.09	4.357	0.54	0.72	3.00	149	50
B7	8.33	0.09	5.490	0.54	0.64	3.00	299	100
B8	8.33	0.09	7.051	0.54	0.57	3.00	599	200
C1	16.7	0.09	2.486	0.30	1.93	1.77	0.05	0.03
C2	16.7	0.09	7.196	0.30	1.13	1.77	0.88	0.50
C3	16.7	0.09	8.616	0.30	1.04	1.77	1.77	1.00
C4	16.7	0.09	10.365	0.30	0.95	1.77	3.54	2.00

Table 5.3: Parameter list for cases based on B3.

Case	Flow type	Bed slope	Helical flow	α_s	Skin friction
F1	Current	Kovacs & Parker	On	1.2	Soulsby
F2	Tide	Kovacs & Parker	On	1.2	Soulsby
G1	Current	None	Off	-	Soulsby
G2	Current	Olesen	Off	-	Soulsby
G3	Current	Kovacs & Parker	Off	-	Soulsby
H1	Current	Kovacs & Parker	On	0	Soulsby
H2	Current	Kovacs & Parker	On	0.6	Soulsby
I1	Current	Kovacs & Parker	On	1.2	Einstein
I2	Current	Kovacs & Parker	On	1.2	Engelund & Fredsøe

asymmetric flow, which usually yields a dominant growth rate with negative k_y wave numbers in the northern hemisphere, i.e. anti-clockwise directed bedforms. This was explained by Zimmerman (1981) by clockwise circulating residual flow cells around the crests, where the upstream velocity was slightly larger than the

downstream. The use of the doubly-periodic bedform allows the simulation of both negative and positive k_y wave numbers in a single simulation, as previously mentioned. Fig. 5.5 shows a comparison between two flow conditions. One, where a steady current is used ($U_c = 1$ m/s and $U_m = 0$ m/s) and averaged with the same results in the opposite direction, and a second, where an M2 tide with frequency $\sigma_2 = 1.4053 \cdot 10^{-4}$ rad/s is simulated ($U_c = 0$ m/s and $U_m = 1$ m/s) and the growth rate is found by averaging over a tidal period. The left plots show the non-dimensionalized growth rate contours with bed load only, while the right show it for combined bed load and suspended load. The peak $(k_x h_0, k_y h_0)$ positions are marked with a dot for a given set, with the peak growth rates Ω^* indicated. In linear theory, from a completely random bed with the same conditions, a bedform of that peak wavenumber is likely to outgrow all other wavenumber modes, thus be the dominant and observable in developed conditions.

It can be seen that the peaks at negative $k_y h_0$ values are highest in each plot, which supports anti-clockwise directed bedforms. The magnitude of the growth rates is smaller in the tidal case, which is expected since the average flow velocity of half a period is lower than the steady current. The peak growth rate in the averaged steady current case is roughly twice that of the tidal case with bed load alone, and roughly a factor four when suspended load is included. The inclusion of suspended load has caused the growth region in k_x to be shortened by a factor three, while roughly maintaining the k_y region. Thus showing that effectively suspended load suppresses the evolution of shorter wave lengths. For the bed load alone, the contours in both flow conditions show a similar form and peaks located at $(k_x h_0, k_y h_0) = (0.051, -0.083)$ for steady current and $(k_x h_0, k_y h_0) = (0.043, -0.071)$ for the tidal flow. This corresponds to wave lengths of O(2 km) rotated approximately 30° to the mean current direction, i.e. sandbanks. In the cases where suspended load is included a difference in the contour shapes is more observable and the peaks are located at $(k_x h_0, k_y h_0) = (0.015, -0.039)$ for steady current and $(k_x h_0, k_y h_0) = (0.019, -0.047)$ for the tidal flow. This corresponds to wave lengths of O(4 km) rotated approximately 20° to the mean current direction, i.e. also sandbanks.

Based on these results replacing a tidal flow with an averaged (positive and negative) steady current for the linear stability analysis seems to be a viable approach, which has also been confirmed through similar testing of other cases. For bed load alone, which is very commonly used in literature, this is even more reasonable. Although the growth contours with suspended load included are visibly different, the peak growth is at a similar region in both flow cases. Thus, both ways yield the same qualitative results and would work to identify the dominant mode. The main advantage of the steady current over the tidal current, is a much shorter computational time.

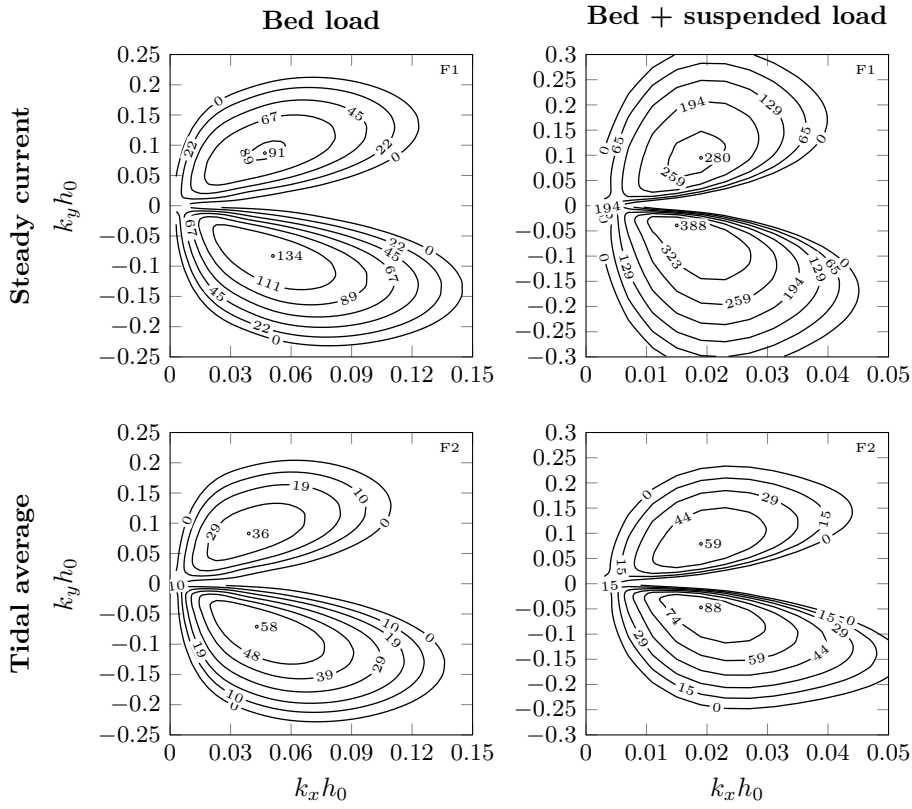

Figure 5.5: Steady current vs tidal current. Non-dimensional growth rate $\Omega^* \cdot 10^{11}$ with bed load alone and combined with suspended load for: $Fr = 0.06$ and $C_{D0} = 0.00459$ with $d_{50}/h_0 = 8.33 \cdot 10^{-6}$. Note the different scaling of the axes.

5.4.2 Bed slope effect

Fig. 5.6 shows the non-dimensional growth rate contours from simulations where the bedform slope effect on the sediment transport was studied. The three configurations are 1) no slope effect, 2) slope effect using the correction by (Olesen, 1987), and 3) slope effect using the correction by (Kovacs and Parker, 1994). Helical flow effects are not included in any of the simulations. Observing the bed load contours, it can be seen that the omission of the bed slope correction produces a bed that is unstable for nearly all simulated wavenumber combinations, without any peak in the range. The contours may close at higher wavenumber values, but at such high wavenumbers it is questionable how valid the shallow

water model is and hence it can be concluded that no bed slope effect essentially destabilizes the bed in a non-physical manner, in line with the conclusion of the analytical work by de Vriend (1986). Inclusion of the bed slope effect thus dampens the growth, mostly of shorter wavelengths, since they have steeper slopes. Comparing the two bed slope correction models, both bed load only and total load, shows that the difference is mainly in the contour shape and very little quantitatively. The empirical model by Olesen results in bedforms slightly more oblique than the vectorial model by Kovacs and Parker, but the latter is preferred in all other simulations because of its reliance on a physical derivation.

5.4.3 Helical flow effects

Fig. 5.7 shows the effect of having the adaption length coefficient in the helical flow equation set to $\alpha_s = 0, 0.6, 1.2$. As seen from the contours, the effect is predominantly influencing the bed load, and therefore the following discussion focuses on the bed load alone plots. The case with 0 adaption length means that essentially Eq. (3.11) is reduced back to Eq. 3.7, i.e. flow responds immediately without any adaption to varying flow conditions. In this case no peak emerges within the studied range and the growth rate increases with increasing wavenumber. With increased adaption length coefficient the higher wavenumbers become stable and a peak growth mode emerges, while the magnitude of the growth rate is reduced. These result are similar to those found by Madsen (2001). While the lateral bed slope effect causes the bed load transport vector to veer downslope, the helical water motion causes it to veer upslope. This balance between these two effects is clearly visible when sequentially considering the plots with $\alpha_s = 0$ (H1), $\alpha_s = 0.6$ (H2), $\alpha_s = 1.2$ (F1) and without the helical flow effect as in the left (G3) plot in Fig. 5.6. The sequence shows that with no adaption length, the helical flow is dominating the bed load vector and causes enhanced bedform development by carrying sediments from troughs to crests, generating steep slopes and shorter wave lengths. The adaption length retards this effect, which is the reason why the growth rate magnitude is reduced and peaks appear at lower wavenumbers. Essentially, the last term on the left hand side of Eq. (3.11) goes to zero and the helical effect becomes insignificant. Increasing the adaption length also yields more asymmetry around $k_x h_0$. This effect is considered later in section 5.4.6. Hulscher et al. (1993) used an adaption length coefficient of 0.6 and were able to show qualitatively how a dominant mode yielding a short waved bedform nearly perpendicular to the mean flow direction emerged. These sandwaves do not appear in the present model because the sediment transport is driven by the depth averaged flow rather than a bed shear stress that can be calculated in the bottom of the flow in a vertically resolved model. The depth averaged flow does not capture the

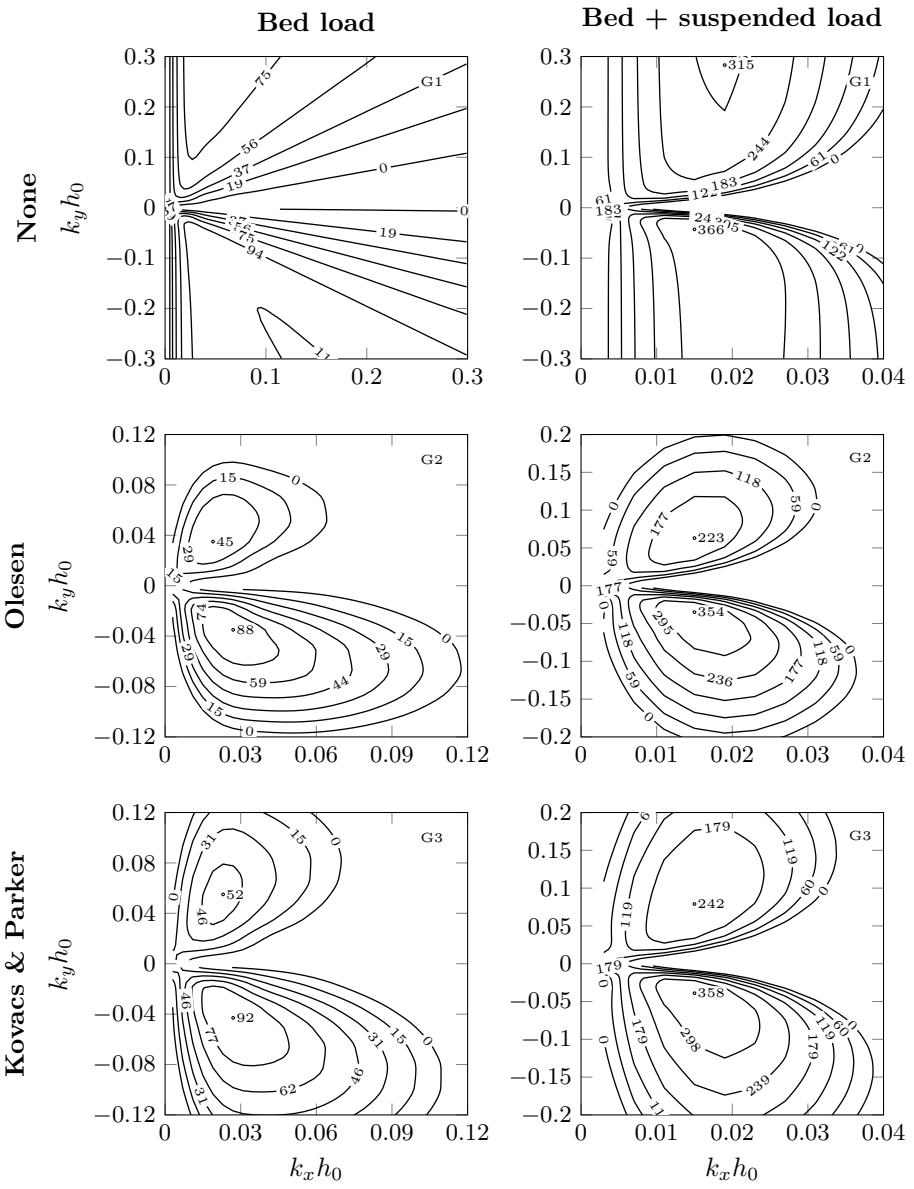

Figure 5.6: Effect of bed slope. Non-dimensional growth rate $\Omega^* \cdot 10^{11}$ for: $Fr = 0.06$ and $C_{D0} = 0.00459$ with $d_{50}/h_0 = 8.33 \cdot 10^{-6}$. Note the different scaling of the axes.

fine variations of the velocity just above bedforms and therefore the mechanism behind the emergence of sandwaves is missing in a depth averaged model. This is confirmed later in Chapter 7. The current results yield wavelengths in the order of 1–2 km and bedform to current angle of approximately 30°, which as previously mentioned, can be characterized as sandbanks.

5.4.4 Skin friction estimation

The growth rate contours in Fig. 5.8 show a comparison between the methods used to calculate the skin friction component of the friction velocity. The methods are Einstein's Eq. 3.26, Engelund & Fredsøe's Eq. 3.37 and Soulsby Eq. 3.30. Qualitatively the results are rather similar so the quantitative difference can be linked to the different friction Shields parameter which is $\theta' = 0.30$ with Einstein's, $\theta' = 0.46$ with Engelund & Fredsøe's and $\theta' = 0.24$ with Soulsby's, which also correlate with a higher value of the growth peaks. The advantage of using Soulby's method for the stability analysis, is that contrary to the other two methods, it is independent of the choice of C_{D0}, so it is easier to control parametrically being affected only by Fr and d_{50}/h_0.

5.4.5 Equilibrium vs non-equilibrium description

Fig. 5.9 shows the growth rate contours where the suspended load formulation is either in equilibrium ($E = 0$) or non-equilibrium. The equilibrium formulation yields a peak at $(k_x h_0, k_y h_0) = (0.059, -0.115)$, while it is at $(k_x h_0, k_y h_0) = (0.015, -0.039)$ with the non-equilibrium formulation. The quantity of the growth rate at equilibrium peak is approximately twice that of the non-equilibrium. The main difference between the formulations, is that the suspended load in the equilibrium description is in phase with the bed shear stress. The suspended load in equilibrium is assumed to be directed in the mean flow direction, thus not affected by bed slope and helical flow effects, as the bed load is. Since these effects are considerably small in the linear regime, the suspended load would practically act as an amplification of the bed load, as they share the same phase (hence, a total load model would show similar results). This causes enhanced transport, and by comparing the equilibrium plot with the bed load alone case (as can be seen in the bottom left plot of Fig. 5.7), the stability contours expand to higher wavenumbers as well as the peaks. The opposite is occurring with the non-equilibrium formulation. This is due to the phase lag, which generates an adaption length for the suspended sediment. As mentioned previously this suppresses the growth of bedforms at higher wavenumbers.

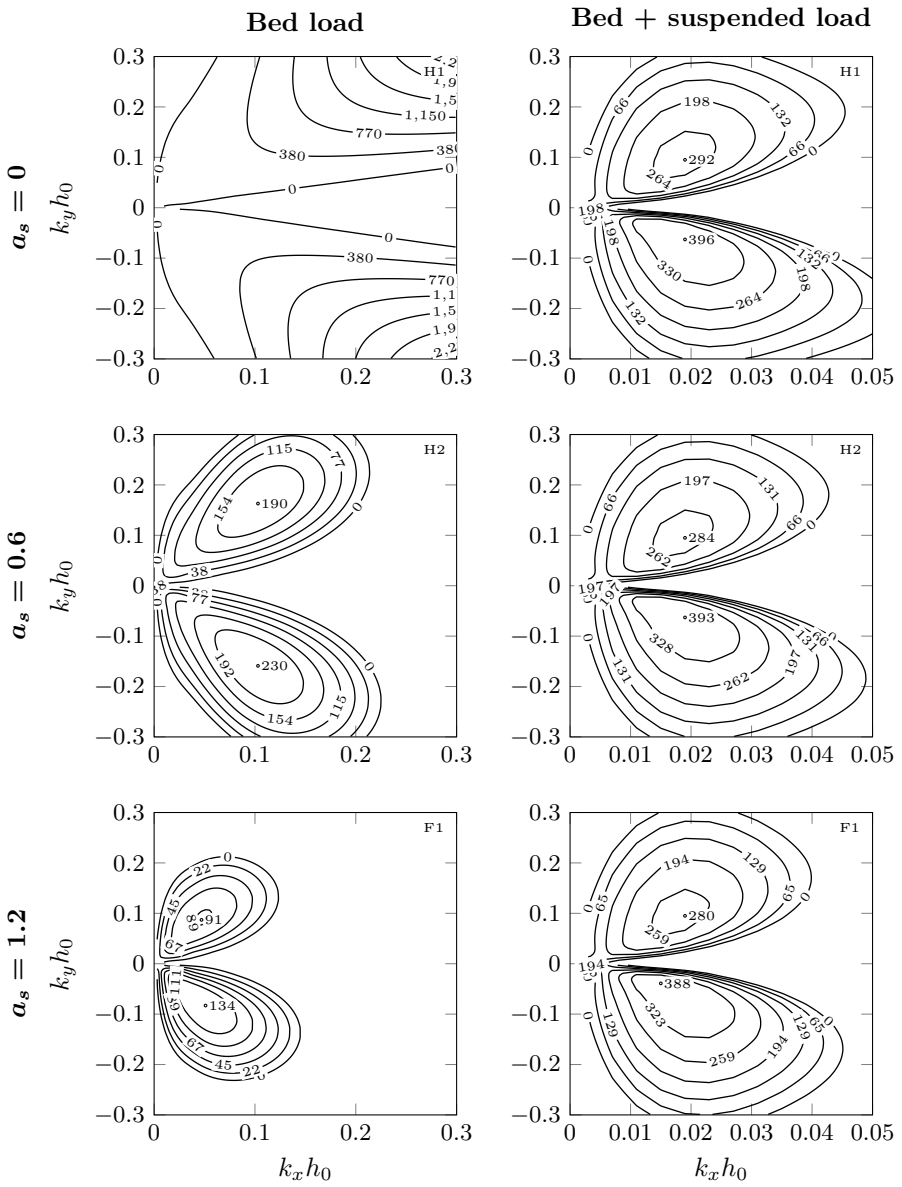

Figure 5.7: Effect of adaption length on helical motion. Non-dimensional growth rate $\Omega^* \cdot 10^{11}$ with bed load alone for: $Fr = 0.06$ and $C_{D0} = 0.00459$ with $d_{50}/h_0 = 8.33 \cdot 10^{-6}$. Note the different scaling of the axes.

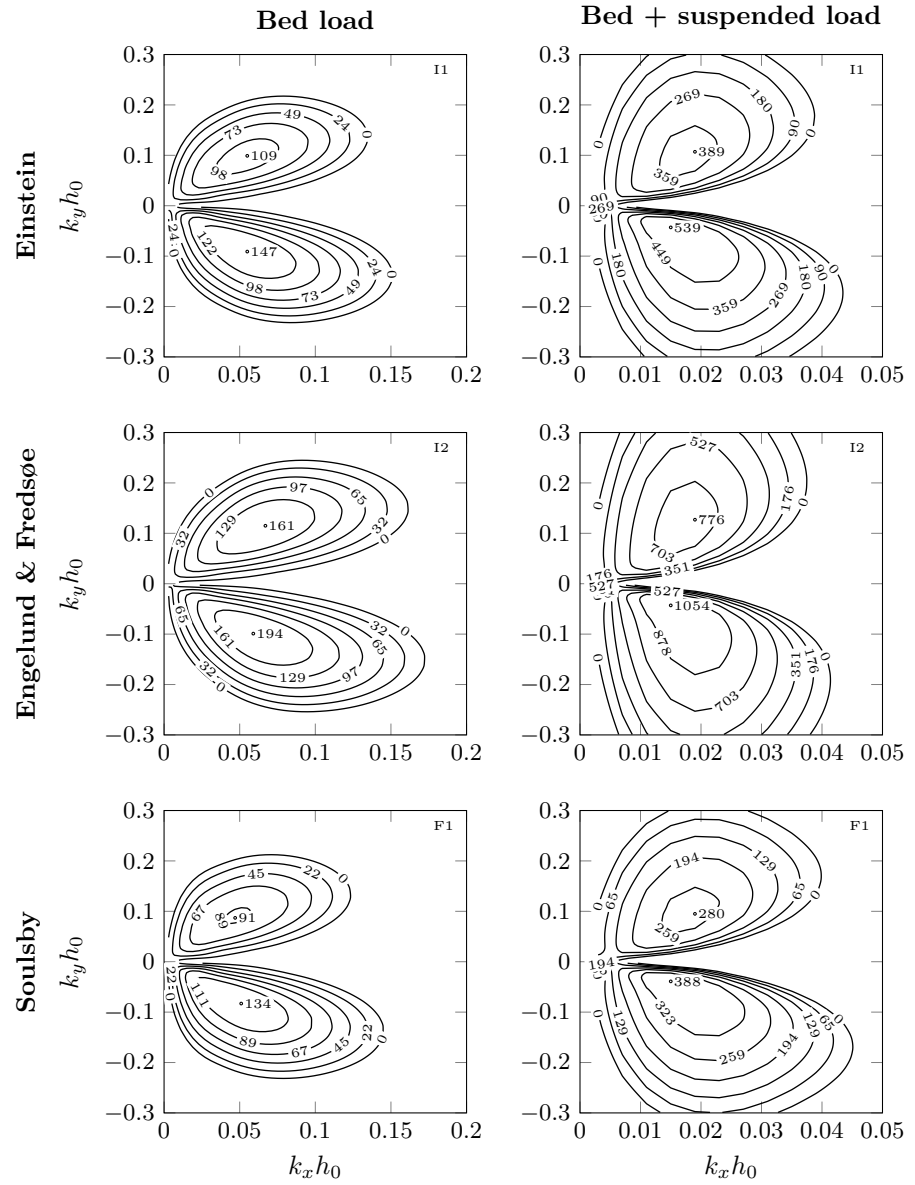

Figure 5.8: Effect of skin friction model. Non-dimensional growth rate $\Omega^* \cdot 10^{11}$ with bed load alone for: $Fr = 0.06$ and $C_{D0} = 0.00459$ with $d_{50}/h_0 = 8.33 \cdot 10^{-6}$. Note the different scaling of the axes.

In order to get a complete description of the physics that govern the problem it is more correct to use the non-equilibrium formulation, and this is therefore used in what follows.

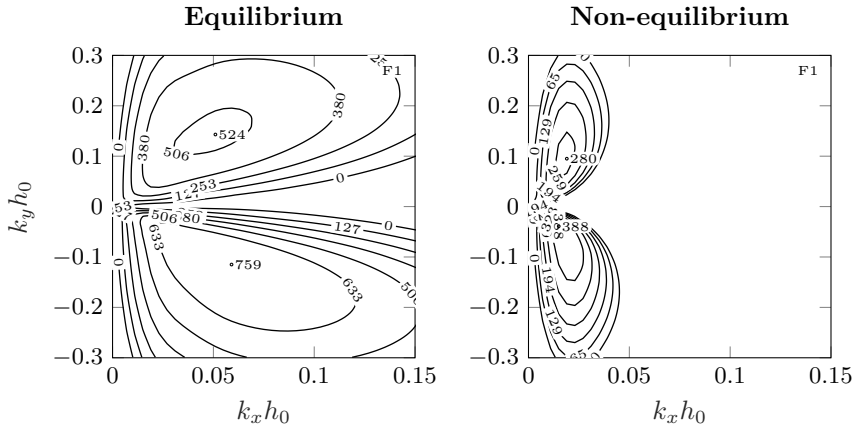

Figure 5.9: Equilibrium vs. non-equilibrium suspended load formulation. Non-dimensional growth rate $\Omega^* \cdot 10^{11}$ with combined bed load and suspended load for: $Fr = 0.06$ and $C_{D0} = 0.00459$ with $d_{50}/h_0 = 8.33 \cdot 10^{-6}$. Note the different scaling of the axes.

5.4.6 Froude number and drag coefficient effect

The results from all cases in Tab. 5.2 will be presented in the following. Figs. 5.10 - 5.14 show growth rate contours, for all the cases in Tab. 5.2. Figs. 5.15–5.19 show the corresponding migration rate contours, for these cases. Each figure groups the results for a constant d_{50}/h_0 and varying Fr and C_D. Results are shown with bed load alone (Figs. 5.10, 5.12 and 5.14) and combined with suspended load (Figs. 5.11, 5.13 and 5.14). The results are organized as follows: Figs. 5.10 and 5.11 for $d_{50}/h_0 = 4.17 \cdot 10^{-6}$, Figs. 5.12 and 5.13 for $d_{50}/h_0 = 8.33 \cdot 10^{-6}$ and Fig. 5.14 for $d_{50}/h_0 = 16.67 \cdot 10^{-6}$. The axis of all plots within a figure are kept fixed in order to assist comparison. The figures with bed load only are presented in order to have a visual comparison between effects of the two sediment transport modes.

A general observation of all figures reveals that increasing Fr, yields growth contours that go from being mostly unstable with negative $k_y h_0$, to becoming more symmetrical around $k_x h_0$, which can also be seen by the ratios of the

peak values with increasing Fr. Furthermore, it is seen that the peaks along with the growth rate contours extend towards higher wavenumbers. Similarly, increasing C_{D0} (i.e. following a figure column from top to bottom) shows the same tendency as with increasing Fr. This is particularly visible in the bed load alone plots. As mentioned previously in the discussion of Fig. 5.7, the adaption length of the helical motion affects the shape of the growth rate contours such that as $\lambda_s \to 0$ the shape becomes more symmetric due to the dominance of the term in Eq. (3.11). Hence, when Fr is increased, effectively $|\mathbf{u}|$ becomes larger and the effect is similar, or when C_{D0} is increased the adaption length decreases through Eq. (3.9). While increasing Fr affects the bed load both through it's effect on θ' and the helical flow, the C_{D0} effect can be related to helical flow only. This is supported by the bed load only plots, where sediment transport is based on skin friction Shields parameter alone. As θ' is only depending on Fr and d/h_0 and independent of C_{D0}, the varying results for bed load alone with increasing C_{D0} imply that it can only influence through the helical flow model.

While increasing Fr and C_{D0} with bed load only yields peaks at higher wavenumbers, it can be different with suspended load. In this case increasing C_{D0} also moves the ridges slightly to higher $k_x h_0$ values, while increasing Fr can have either effect. This is because the change in C_{D0} for the suspended load model, affects the shape of the assumed velocity and concentration profiles, while increasing Fr increases the magnitude of the velocity, yielding a larger adaption length of the concentration, so is more difficult to predict the combined effect. It can be seen that inclusion of suspended load tends to yield sandbanks that are more parallel with the mean flow. The inclusion of suspended sediment also increases the magnitude of the growth rates compared to bed load alone and reduces the unstable region to lower values of $k_x h_0$ and gradually higher values of $k_y h_0$ such that instead of peaks, ridges with constant $k_x h_0$ emerge. These effects can be seen even for values as low as $\Phi_s/\Phi_b = 0.5$ (cases A2, B2 and C2). A comparison can be drawn to (de Vriend, 1990, Figs. 8 and 11), which show growth rate contours for bed load and suspended load, respectively and individually, where $\Phi_s/\Phi_b = 1$ and $C_D = 0.0039$ based on his stated transport rates and Chezy number. de Vriend (1990) did not superimpose the two figures, but it can be seen that doing so would yield similar contour shapes to those presented here as combined bed load and suspended load. Contrary to de Vriend (1990) however, the results here show that the magnitude of the growth rate increases significantly, rather than decreases when suspended load is included. Upon inspection, qualitatively similar findings can also be seen in the limited comparisons made by Madsen (2001), though these results are not widely available. de Vriend (1990) used a simpler suspended load model than used here and it is not clear what Froude number and grain size have been used. The physical parameters considered herein are unambiguous, and over the realistic range considered in the present model yield a qualitatively different conclusion, in this regard.

With respect to the importance of the sediment grain size, the results show that it is mostly a quantitative matter, while being qualitatively similar for all grain sizes. Obviously heavier sediments yield less suspended load and require stronger flows to be in motion compared to lighter grains. In all cases, the emerging peaks of the contours suggest dominant wave lengths in the range 1–5 km with an angle of approximately 20°–40°. The migration rate plots (Figs. 5.15–5.19) show a tendency to be increasing with $k_x h_0$ for the bed load alone, while the contours including the suspended load show a peak along the $k_x h_0$ axis, and negative migration rates at higher wavenumbers $k_x h_0$.

5.5 Closing remarks

The model used within the present framework is an extension of river models adapted into a tidally dominant offshore environment. The accuracy of the results is very difficult to verify due to the practical challenges involved in setting up laboratory models of the same scale, or even just measuring in the field. Hulscher (1996) found tide-parallel sandbanks to appear using bed load alone, while the present work suggests the necessity of suspended load for the process. Although not included here, waves stirring up sediments could increase the suspended load carried by the current. The free choice of the C_{D0} parameter could imply, to some extent, an implicit inclusion of that stirring effect. As discussed in the review, some disregard the suspended sediment load in their 2DH models in the offshore environment. It can be seen that this simplification can have tremendous effects on the results, also when suspended load is accounted for in a total transport model, due to the lack of a phase lag. As mentioned previously, many linear stability studies in literature non-dimensionalize the perturbed growth rate with the unperturbed sediment flux. This allows a direct comparison on the amplification effect of each transport mode. For an equivalent transport of bed and suspended load, de Vriend (1990) found a much smaller growth amplification for suspended load than for bed load. As mentioned in the previous section, superimposing de Vriend (1990) figures 8 and 11 would yield a different result for the total growth since the stable region of the suspended load plot covers and overwhelms a large extent of the unstable region in the bed load plot, due to large decay amplifications. This alone should emphasize the importance of including suspended load. Additionally, it is important to remember that in the sea, the bed would react to a given arbitrary sea state, thus the magnitude of the transport plays an important role and as the results herein suggest, the suspended load in many circumstances is a dominant factor, which should not be ignored. It is emphasized that the non-dimensionalization utilized herein is intended to be straightforward, and hence representative of physically realistic scenarios.

On a side note, caution should be taken when interpreting the results using suspended load near the limits of the validity of the theory, since there is some empirical based background involved. At very low Φ_{s0}/Φ_{b0} ratios a pronounced effect by the suspended load on the growth contours is already visible due to the nature of the equations. Similarly, a common upper limit of $w_s/u'_f < 0.8$ is used to determine whether sediments can be suspended, or become too heavy and hence transported in layers on the bed load. The results in the current stability analysis do not consider these limitations, since the focus is on studying the effects of the different parameters, but for a morphological study it would be better to avoid low ranges of Φ_{s0}/Φ_{b0} and make sure to be within $w_s/u'_f < 0.8$.

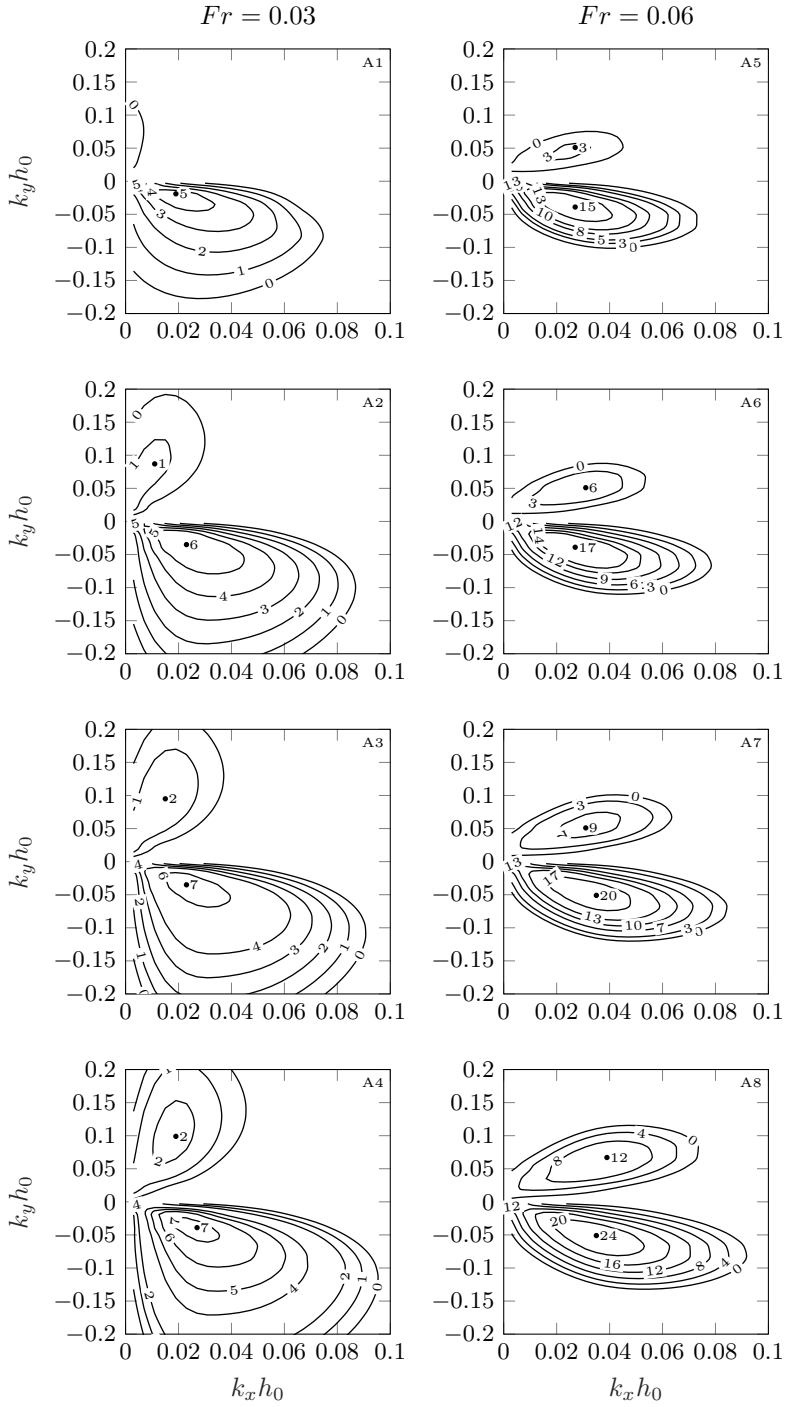

Figure 5.10: Non-dimensional growth rate $\Omega^* \cdot 10^{11}$ with bed load alone for various Fr and C_{D0} with $d_{50}/h_0 = 4.167 \cdot 10^{-6}$

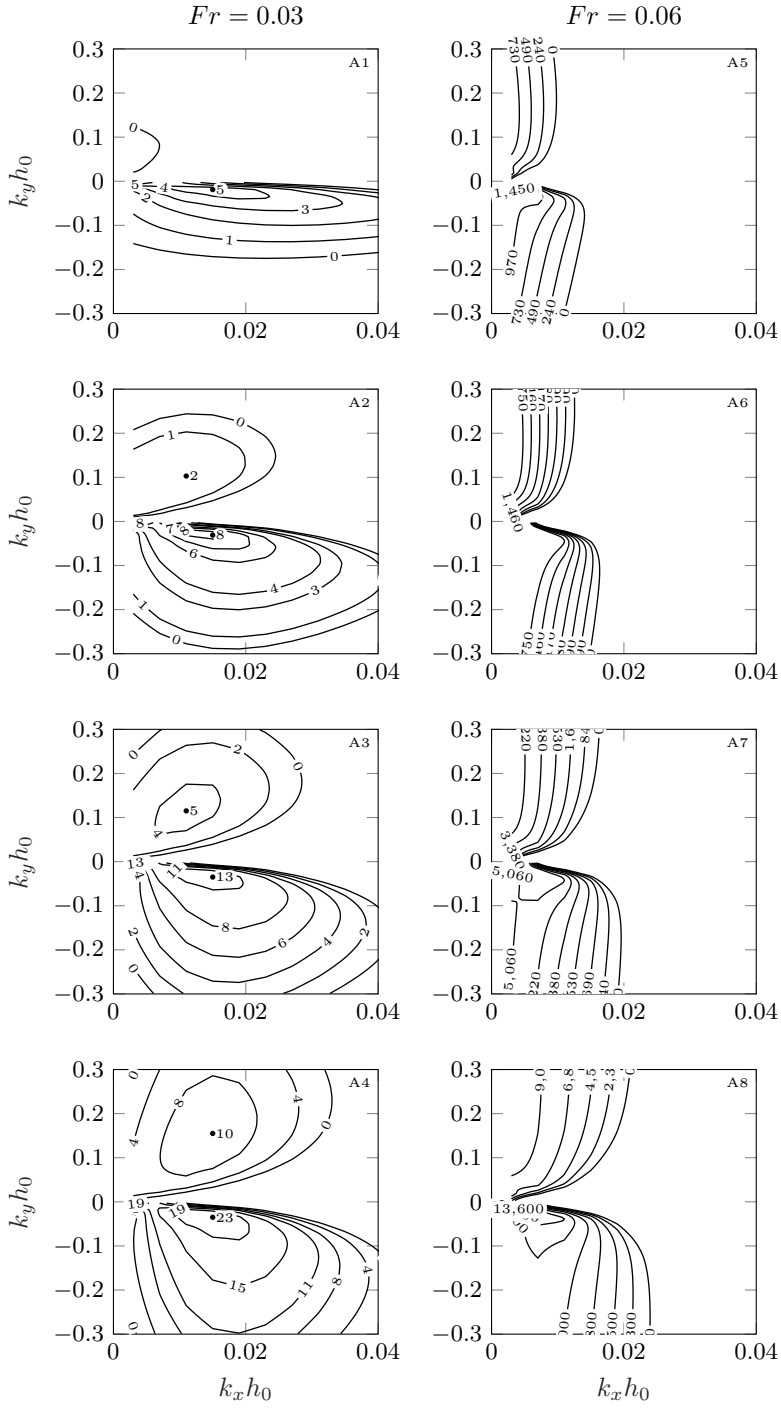

Figure 5.11: Non-dimensional growth rate $\Omega^* \cdot 10^{11}$ with bed load and suspended load for various Fr and C_{D0} with $d_{50}/h_0 = 4.167 \cdot 10^{-6}$

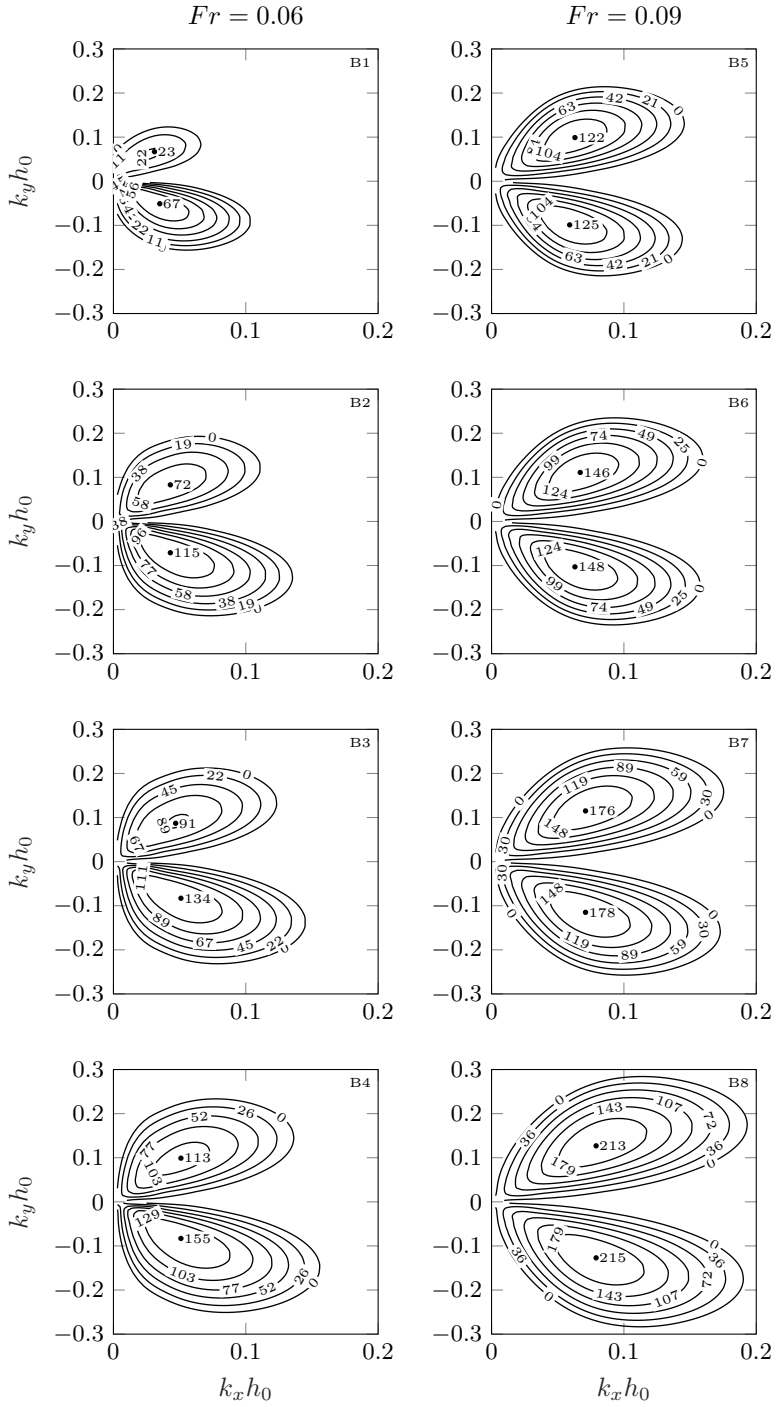

Figure 5.12: Non-dimensional growth rate $\Omega^* \cdot 10^{11}$ with bed load alone for various Fr and C_{D0} with $d_{50}/h_0 = 8.333 \cdot 10^{-6}$

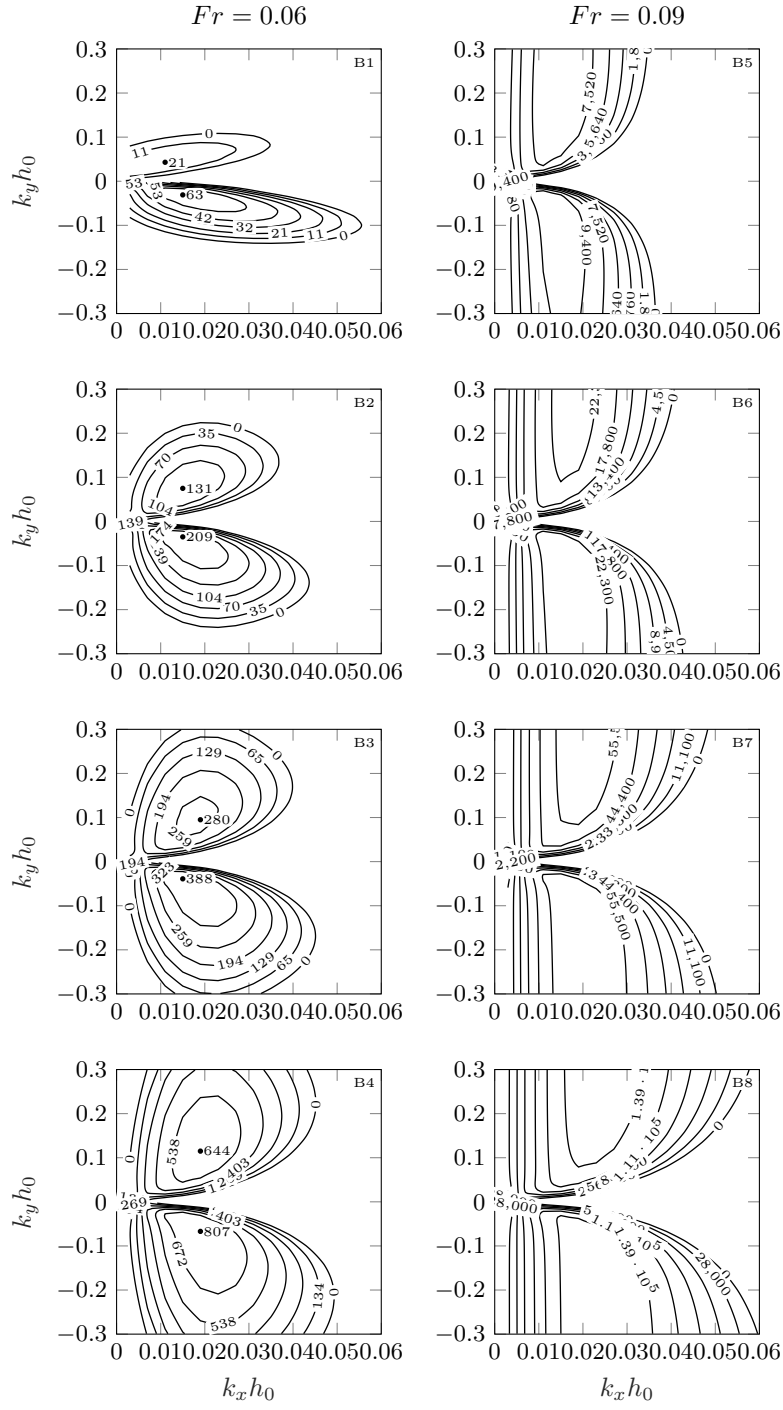

Figure 5.13: Non-dimensional growth rate $\Omega^* \cdot 10^{11}$ with bed load and suspended load for various Fr and C_{D0} with $d_{50}/h_0 = 8.333 \cdot 10^{-6}$

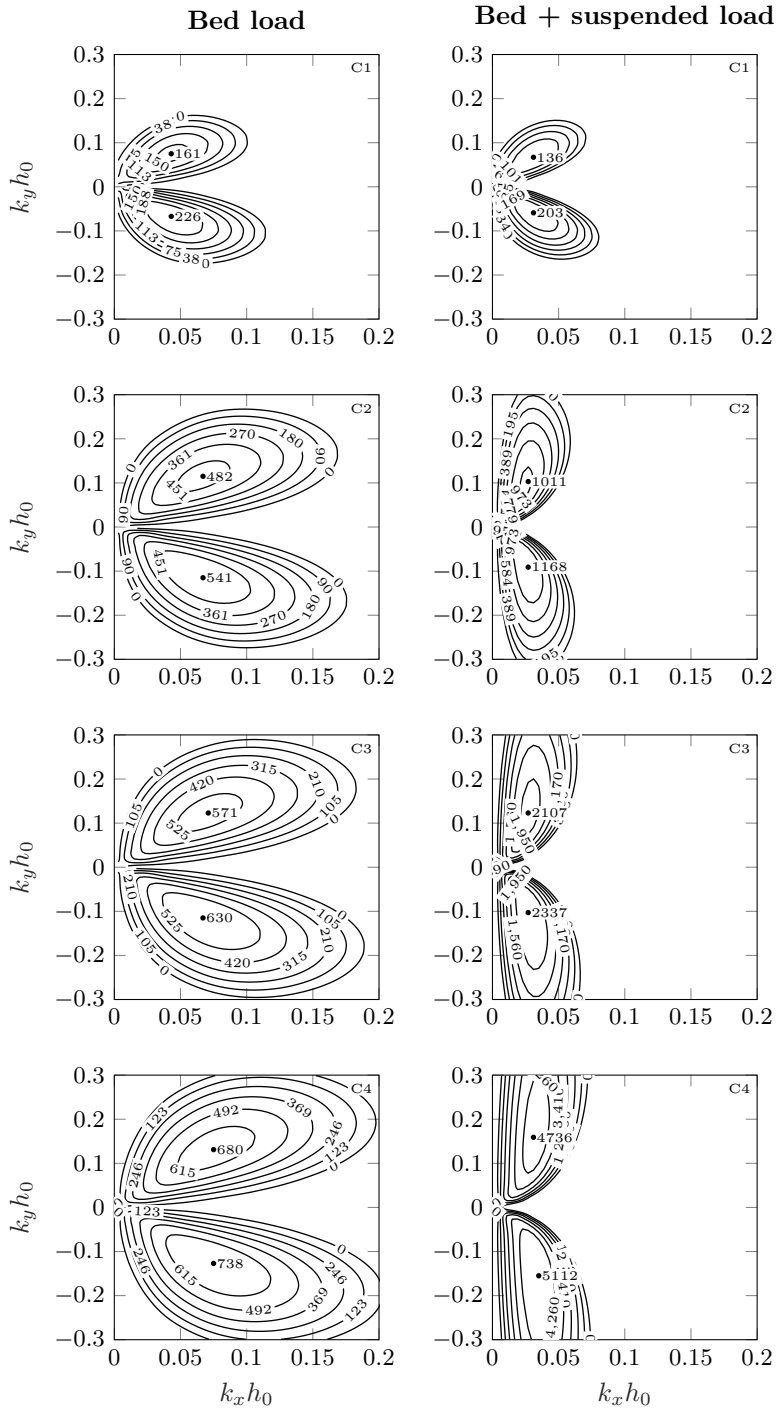

Figure 5.14: Non-dimensional growth rate $\Omega^* \cdot 10^{11}$ with bed load alone and with suspended load for $Fr = 0.09$ and various C_{D0} with $d_{50}/h_0 = 16.67 \cdot 10^{-6}$

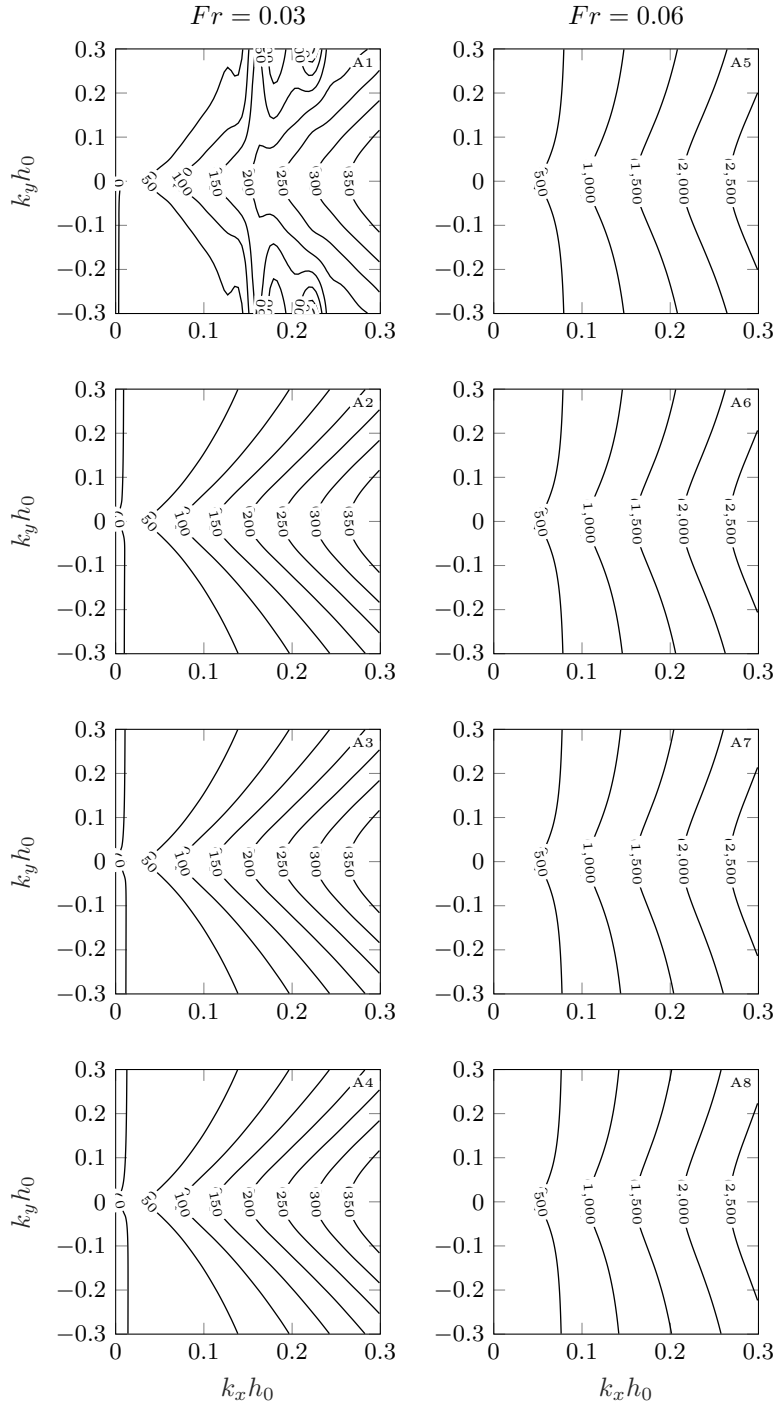

Figure 5.15: Non-dimensional migration rate $\omega_b^* \cdot 10^{11}$ with bed load alone for various Fr and C_{D0} with $d_{50}/h_0 = 4.167 \cdot 10^{-6}$

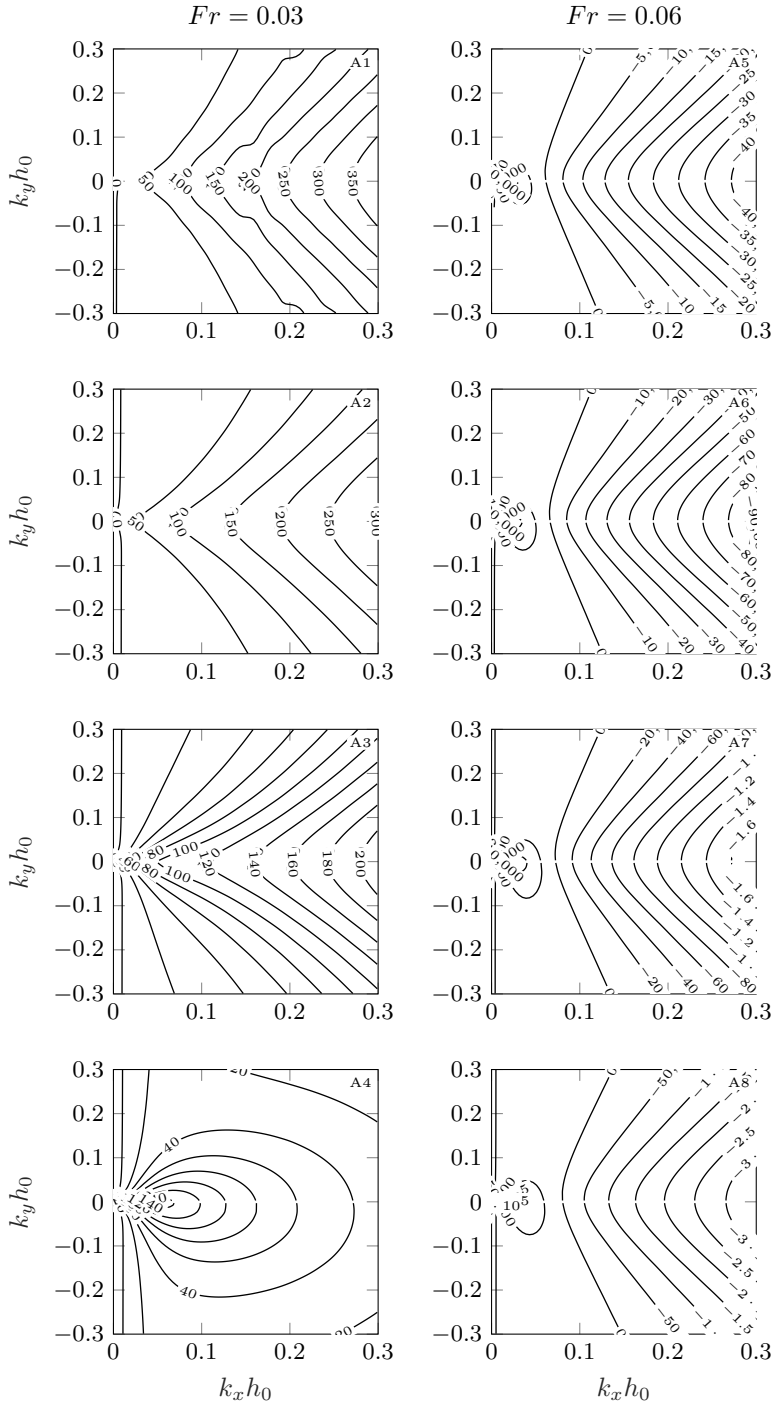

Figure 5.16: Non-dimensional migration rate $\omega_b^* \cdot 10^{11}$ with bed load and suspended load for various Fr and C_{D0} with $d_{50}/h_0 = 4.167 \cdot 10^{-6}$

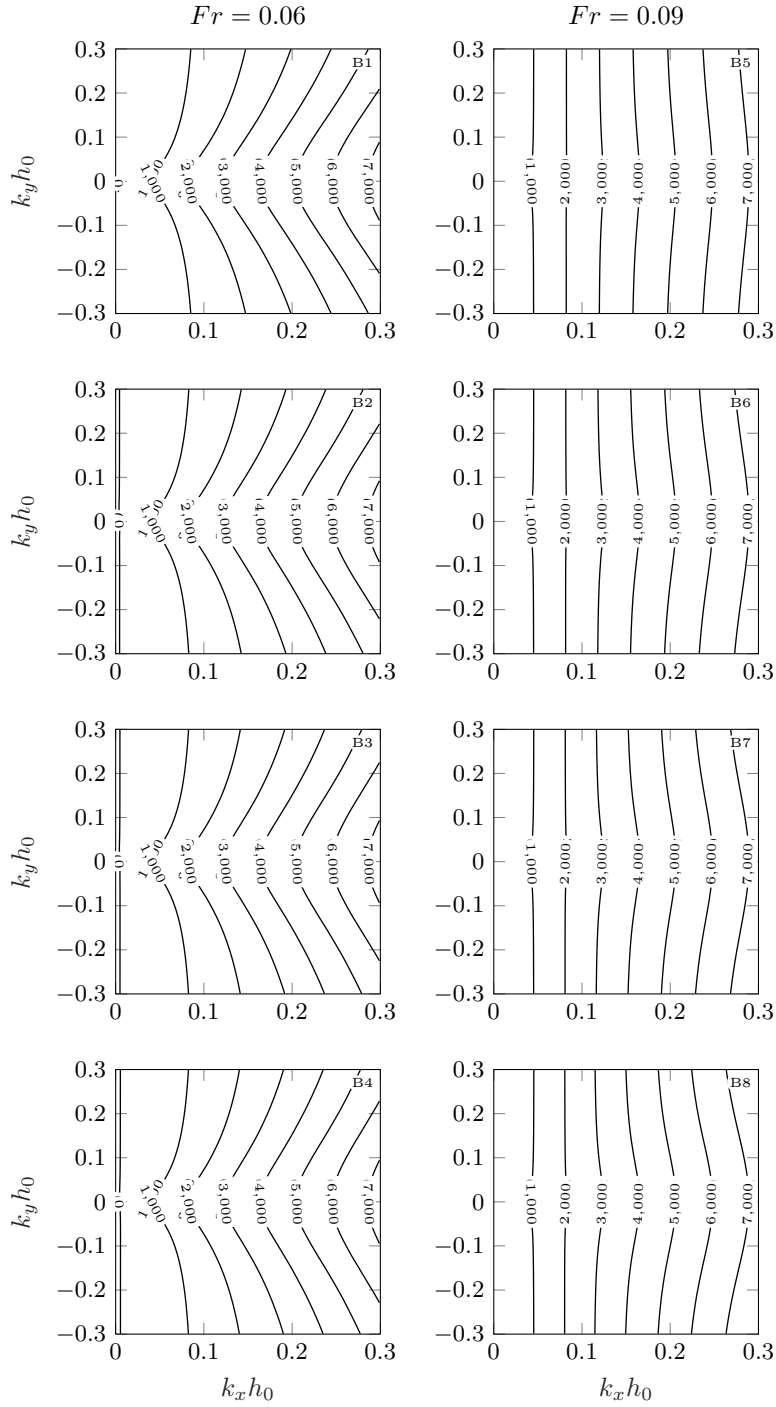

Figure 5.17: Non-dimensional migration rate $\omega_b^* \cdot 10^{11}$ with bed load alone for various Fr and C_{D0} with $d_{50}/h_0 = 8.333 \cdot 10^{-6}$

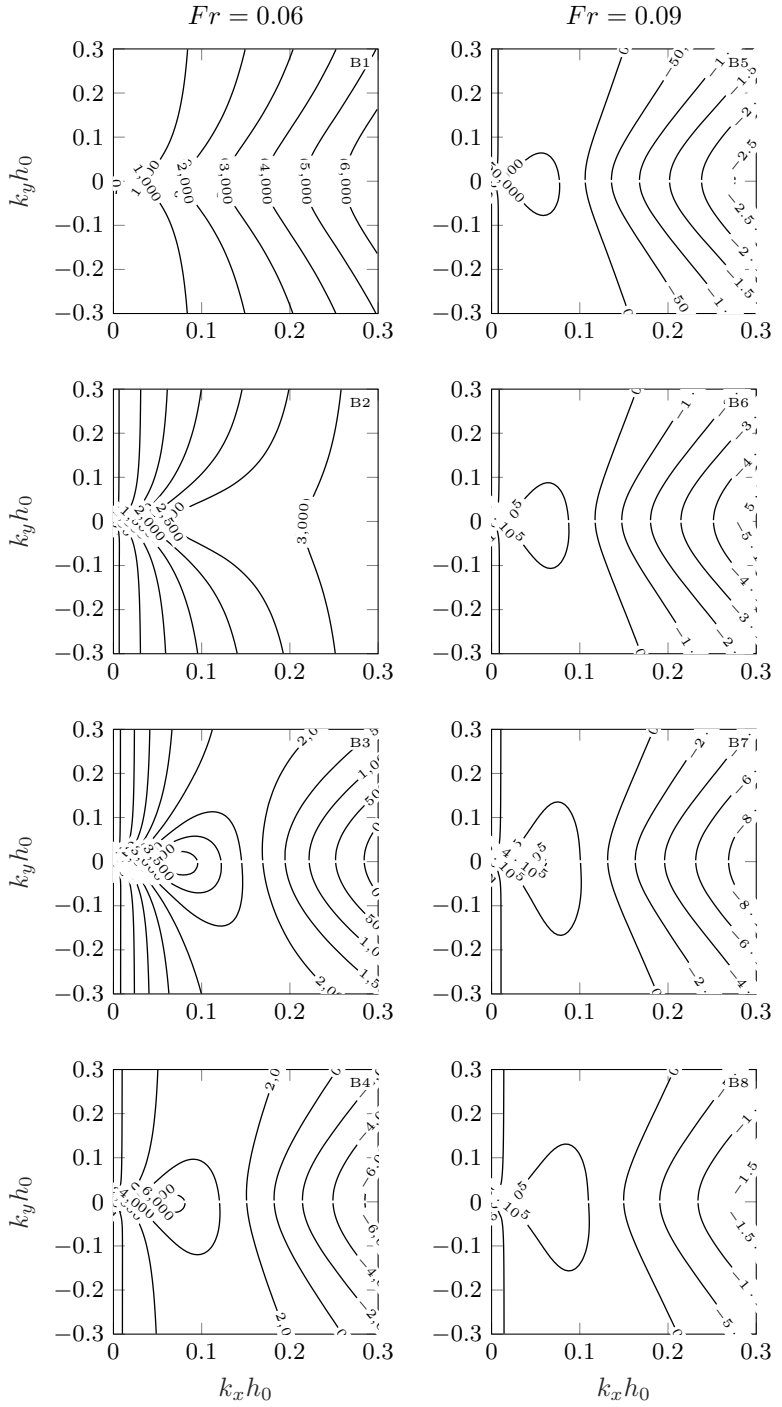

Figure 5.18: Non-dimensional migration rate $\omega_b^* \cdot 10^{11}$ with bed load and suspended load for various Fr and C_{D0} with $d_{50}/h_0 = 8.333 \cdot 10^{-6}$

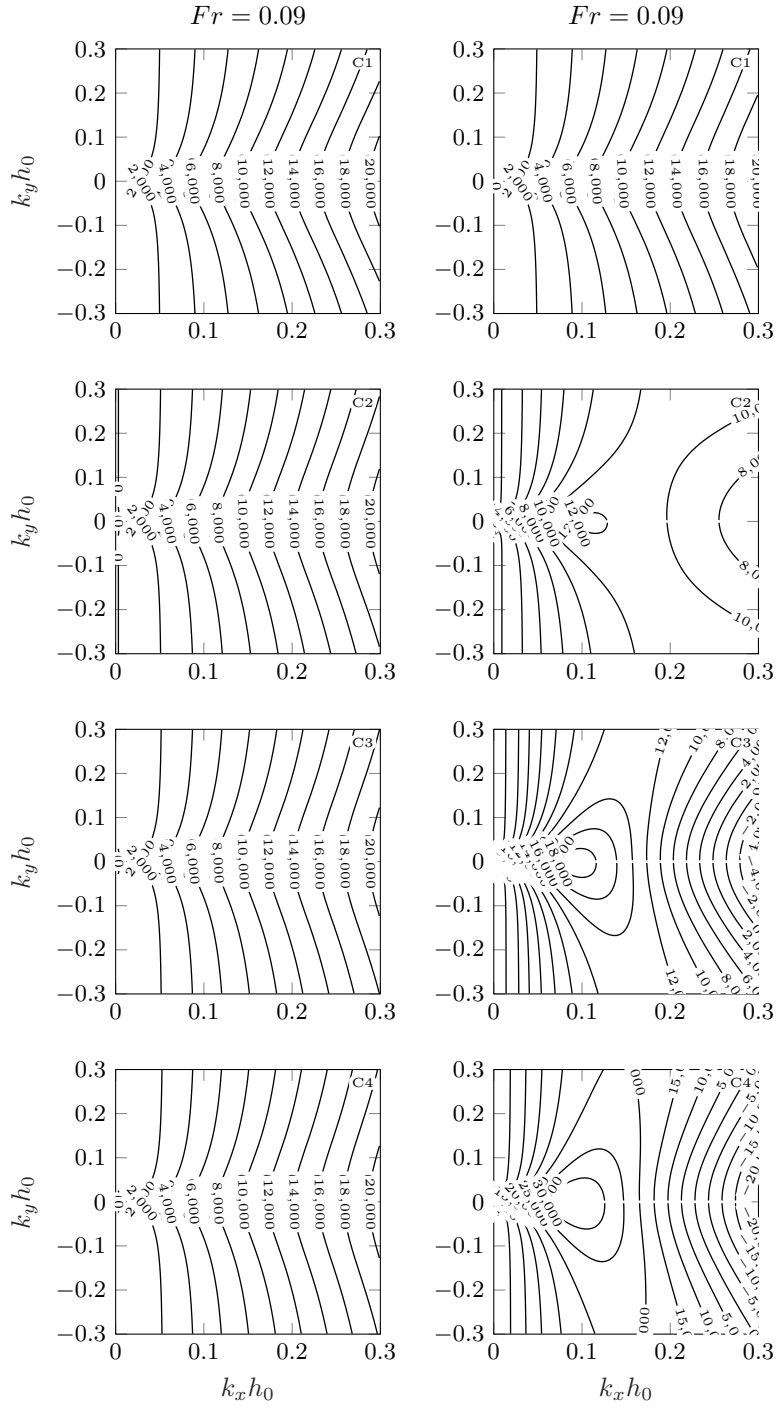

Figure 5.19: Non-dimensional migration rate $\omega_b^* \cdot 10^{11}$ with bed load alone and with suspended load for $Fr = 0.09$ and various C_{D0} with $d_{50}/h_0 = 16.67 \cdot 10^{-6}$

Chapter 6

Morphological simulations

This chapter presents morphological simulations of large-scale bedforms conducted with the 2DH Matlab model. In the first part, the simulations verify the predictions of the linear stability analysis in the early stages of developing bedforms. Furthermore, it is investigated how the domain size influences the simulation outcome and a comparison is made for bedform development under various tide-plus-current scenarios. In the second part the bedforms' interaction with offshore wind farms, modeled as additional flow resistance, are investigated. Preliminary results were published in Margalit and Fuhrman (2017).

6.1 Introductory remarks

The linear stability analysis in the previous chapter provided information on how the various parameters affect the outcome in terms of the bedforms' initial growth and migration rates, wavelengths and orientation. It is however questionable whether these results will be representative of the finite bedforms, i.e. in their fully developed stage, and it does not provide any information regarding the final shape and the timescale of the bedforms' evolutionary process. As was discussed in the review, linear stability analyses comprised the majority of the work conducted on formation of large-scale bedforms in the sea. These were

primarily used to understand the underlying mechanisms involved in making a specific wavelength grow rather than others, but their predictive capabilities have been rather vague in the offshore environment and the very slow morphological timescale makes a validation challenging. In other words, any predictions of a linear stability analysis of large-scale bedforms in the open sea, attempting to explain currently observed bedforms could be entirely coincidental, since the evolutionary process could be in the order of decades, centuries and even millenniums. The linear stability analysis is despite its above mentioned shortcomings, an excellent tool to support a morphological study. It provides information on what one could expect to be the important parameters of the problem and guide towards "smarter" model inputs and domain sizing, as well as qualitative interpretations of the result.

The periodic boundaries of the computational domain have an implication on the possible outcomes of the simulation by restricting the number of bedforms in the domain to an integer value. Furthermore, the sediment within the domain is a circulating finite quantity, which implies that the integral of the bed function h_b will remain constant throughout the simulation. While most presented simulations reached a bedform in equilibrium, in some other simulations the bed keeps getting deeper troughs, while the crests keep growing until it nearly reaching the surface, which causes the simulation to blow up. This does not necessarily mean that the result is wrong. The evolution of the large-scale bedforms takes place over a very long timescale, hence large amplification factors are used in the Exner equation (Eq. 3.91) in order to speed up the morphology. This can lead to quantitative inaccuracies and numerical instabilities and should therefore be used with caution. The bed evolution is monitored with the max bedform height (lowest point to highest point in the domain) and the root-mean-square bed values. As opposed to the linear stability analysis where parameters were presented in their non-dimensional form, in the morphological study all parameters are presented in their dimensional form, to emphasize the physical order of magnitude of the results.

6.2 Large-scale bedform evolution

6.2.1 Sinusoidal perturbation

6.2.1.1 Bed load only

In the previous chapter, growth and migration rates were obtained for sinusoidal perturbations of a flat bed, assuming exponential growth within a linear

morphological regime. The extent of time in which these rates represent the bedform development is now studied by allowing the bed to morph. The parameters of case B1 from Tab. 5.2 with $h_0 = 30$ m are used to simulate the morphological evolution of a bedform prescribed by Eq. 5.1 with wavenumbers $k_x h_0 = 0.033$, $k_y h_0 = -0.049$, which the linear stability analysis has shown to yield the fastest growth rate. Only bed load is included since the parameters of case B1 give a minor suspended load transport, and considering the previously discussed uncertainty of including the suspended load at the very low Φ_{s0}/Φ_{b0} ratios. The linear stability analysis demonstrated that using the spectral method, the bedform could be resolved with 16 grid points in each direction. In the morphological stage nonlinear interactions between bedform modes and the flow happen and it is therefore not necessarily sufficient to apply the same grid resolution. Therefore, the bedform morphology is tested with three different resolutions, namely $N = 16$, 32 and 64. The morphological development has been amplified by a factor 100,000 to speed up the simulations.

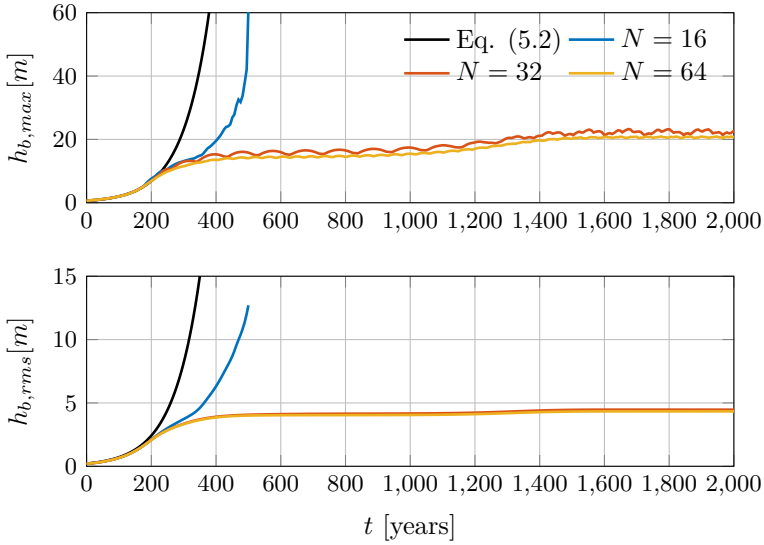

Figure 6.1: Maximum bedform height (max) and root mean square (rms) bed value during the simulation of case B1 with domain wavenumbers $k_x h_0 = 0.033$, $k_y h_0 = -0.049$ resolved by N grid points in each direction. Only bed load included.

Fig. 6.1 shows the growth over time of the bedform represented by the maximum bedform height ($h_{b,max}$) and the root-mean-square ($h_{b,rms}$) value of the bed. In addition to the refined grid simulations, the exponential development given by Eq. 5.2 is also included. The figure shows that regardless of the grid resolution, the bedform initially experiences an exponential growth. Fig. 6.2 shows that

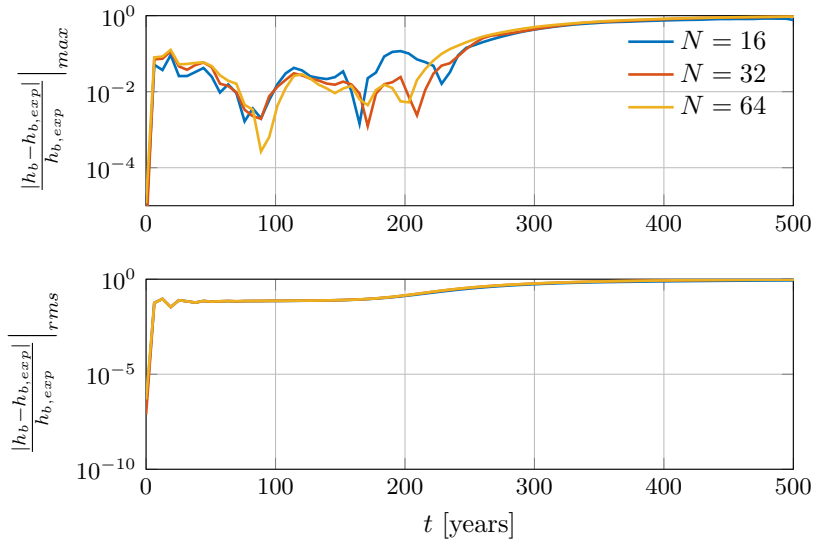

Figure 6.2: Difference between the exponential (exp) and the simulated solutions of case B1 for the first 500 years.

in approximately the first 200 years, the simulations are matched within 10% by Eq. 5.2. After some time with exponential growth, the bedform enters a transitional stage with a damped growth, after which the results show a grid-resolution-based deviance. The simulation with $N = 16$ shows that the bedform remains unstable and grows exponentially until reaching the surface. On the other hand, at approximately the 500 years mark, the simulations with $N = 32$ and 64 enter a stage of moderate stability, where the bedform reaches a temporary equilibrium in form and height, and predominantly migrates. Within this period the effect of the second fastest growing mode, corresponding to the second peak in the linear stability contour in Fig. 5.12 (B1), becomes visible as the bedform still experiences a minor growth which stabilizes at about the 1,400 years mark. At this stage the bedform crest is approximately at elevation 6 m, while the trough is approximately at -14 m, i.e. bedform height 20 m, or $0.67h_0$.

Figs. 6.4 and 6.5 show the form of the bed at selected times of the morphological evolution, through a stream-wise middle section and a top view, respectively. The section also includes the bedform with the exponential growth rate given by Eq. 5.2 for comparison. As mentioned before, the growth of the bedform in terms of the height is matched very well with the linear stability analysis in the first stage, however, the actual migration rate appears to be slower than the rate found in the linear stability analysis. The last time instance in Fig. 6.5

shows that the final bedform shape has become doubly periodic, due to there being growth in the positive k_y wavenumbers as well. Thus the final shape is the result of nonlinear interaction between all the modes confined in the domain. This is also illustrated in Fig. 6.3 in 3D.

Additionally, it can be seen that as long as the bedform maintains its sinusoidal shape, the representation of it is smooth with all the tested grid resolutions. Once it becomes skewed and resembles dunes in the sectional shape, discontinuities appear, but the overall bed level values are similar. The mechanism behind the bedform's growth is (as described in Chapter 2), the balance between the flow driving the sediment transport and the gravity effect on sediments over the sloping bed. Once the bedform reaches a certain height, the downslope becomes so steep that there is equilibrium between the flux of sediments going up to- and down from the crest. It is therefore necessary to resolve the steep downslope gradient correctly, which is not attained with 16 grid points for the whole bedform. A comparison between $N = 32$ and 64 in Fig. 6.1 shows that the max bedform height at the stable stage is "bumpier" with the lower grid resolution. This is caused by the morphological amplification which makes the crest slightly overshoot the growth when the steep downslope of the bedform is less resolved. The excessive growth leads to a higher crest that is then eroded away, leading to the "bumpy" pattern. On the other hand, the rms level of the bed is smooth for both cases and practically identical. Thus it can be concluded that the simulation can be conducted with 32 grid points per wavelength to yield satisfactory results.

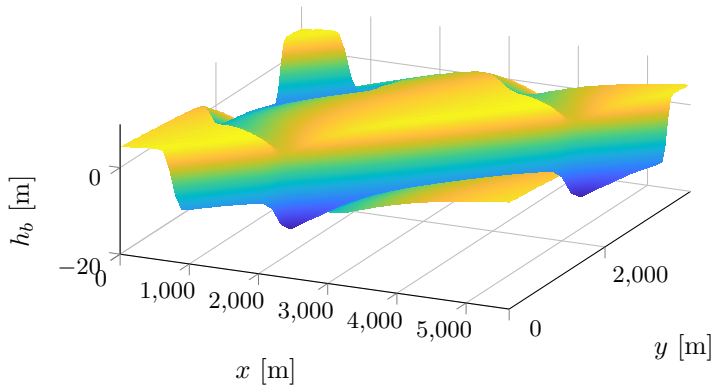

Figure 6.3: 3D view of the bed at $t = 1500$ years. Case B1.

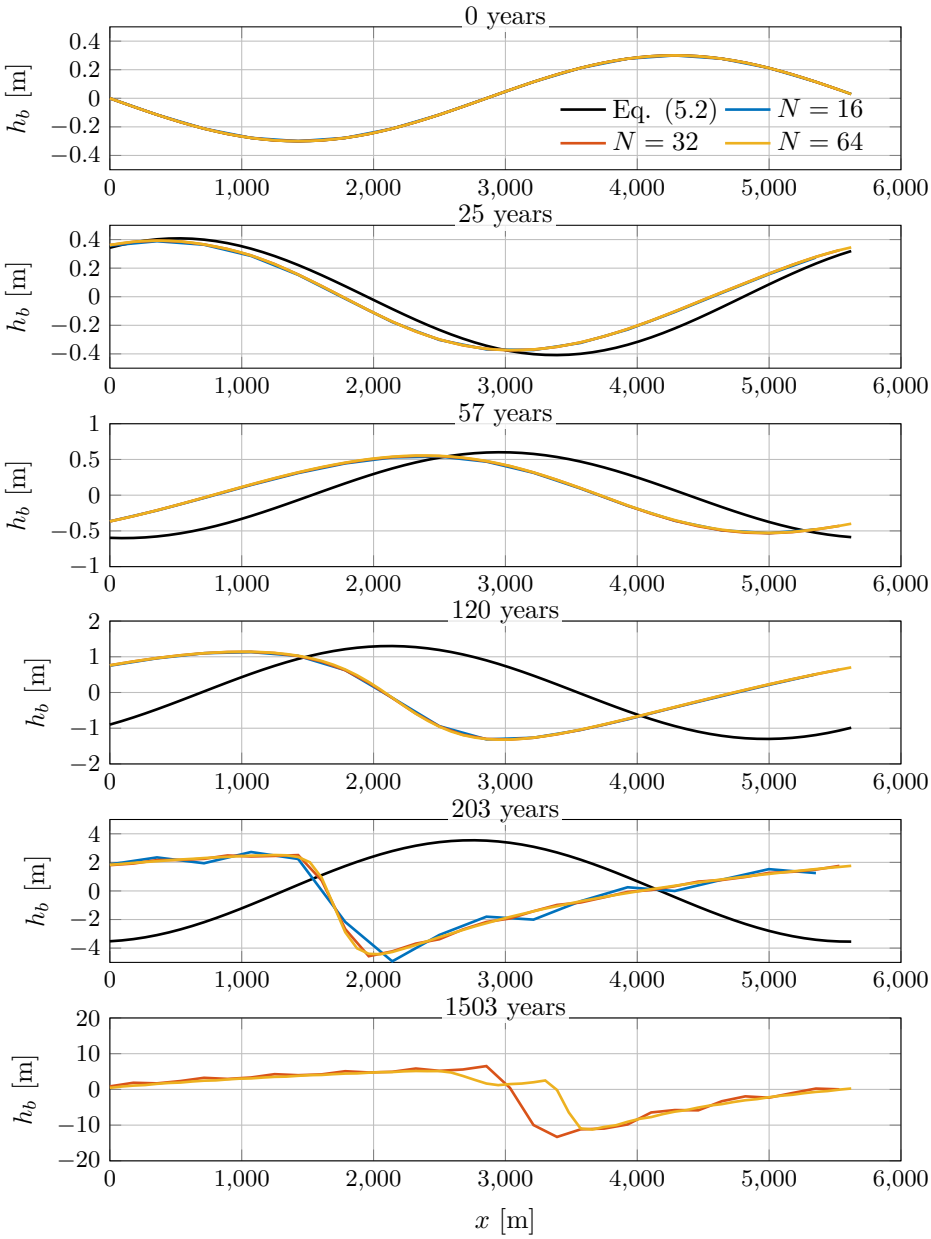

Figure 6.4: Longitudinal section profiles of the bed through center. Case B1.

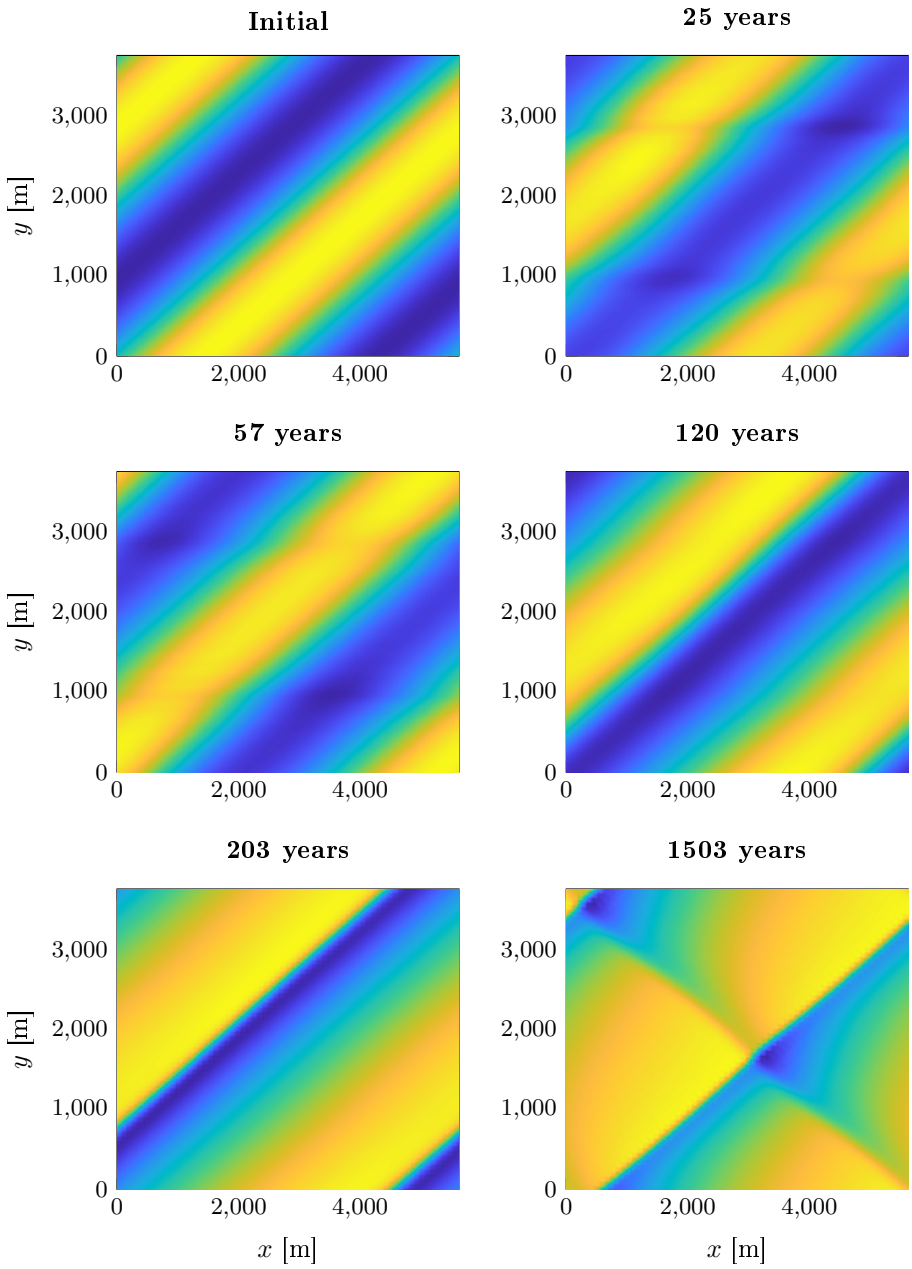

Figure 6.5: Top view of the morphing bed. Blue indicates deeper areas / yellow shallower areas. Case B1.

6.2.1.2 Bed load and suspended load combined

Case B3 from Tab. 5.2 with $h_0 = 30$ m is now used to study the morphological development of a bedform using both bed load and suspended load. The fastest growing mode was found to have wavenumbers $k_x h_0 = 0.017$, $k_y h_0 = -0.049$, which were used to perturb the bed and run a simulation in the same manner as with case B1 above. The morphological development was amplified by a factor 10,000. Fig. 6.6 shows the time development of the max height of the bedform, where it can be seen that the bedform grows exponentially all throughout the simulation, which eventually blows up due to the bed reaching the surface. The development for both $N = 16$ and 32 is similar, but grow at a slightly lower rate than the prediction in the linear stability analysis given by Eq. 5.1. The timescale in the present case is in the order of decades, contrary to centuries in B1's case. This faster rate is naturally caused by the additional sediment flux from the suspended load. The reason that the bedform keeps growing exponentially is not physical, but can rather be attributed to a limitation in Galappatti's (1983) suspended load model, explained in the following.

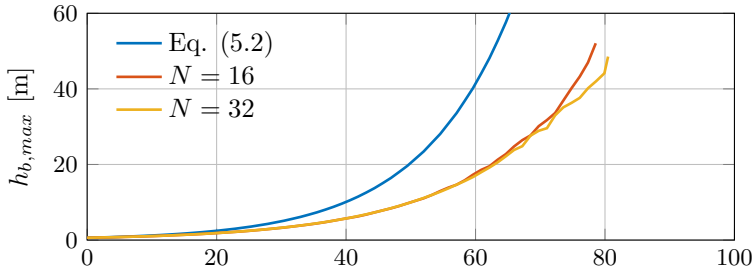

Figure 6.6: Maximum bedform height (max) of bedform during the simulation of case B1 with domain wavenumbers $k_x h_0 = 0.017$, $k_y h_0 = -0.049$ resolved by N grid points in each direction. Bed load + suspended load.

The concentration boundary condition (Eq. 3.71) in the x direction can be written

$$T_A \frac{\partial \bar{c}}{\partial t} = \bar{c}_e - \bar{c} - L_A \frac{\partial \bar{c}}{\partial x} \tag{6.1}$$

where T_A and L_A are the adaption time and length, respectively. A solution to (6.1) in a steady uniform flow, initially not in equilibrium, could be given by

$$\bar{c} = \bar{c}_e - \bar{c}_e e^{-t/T_A} \tag{6.2}$$

which shows that $(\bar{c}_e - \bar{c})$ will decay exponentially, leading the instantaneous concentration to eventually adapt to the equilibrium concentration. On the

other hand, with a periodic unstable bed the amplitude grows exponentially as described by Eq. 5.2, where the perturbation is given by

$$\tilde{h}_b = Ae^{\Omega t}\sin(k_x x + k_y y - \omega t) \tag{6.3}$$

from which it follows that the velocity and the depth would take a similar form given by

$$U = U_0 + \tilde{U}, \quad h = h_0 + \tilde{h} \tag{6.4}$$

One of the simplest ways of obtaining the sediment transport is as a power of the velocity such as

$$q = aU^b \tag{6.5}$$

where a and b are calibration parameters with b typically being of order 3 or higher. As described in Chapter 3, the depth, velocity and transport rates are then used to calculate the equilibrium concentration by

$$\bar{c}_e = \frac{q}{hU} = \frac{aU^{b-1}}{h} \tag{6.6}$$

Thus the term $(\bar{c}_e - \bar{c})$ would in fact diverge for $b > 1$ due to the exponential nature of the perturbation amplitudes, see Fig. 6.7. Initially there is a decay because it is in a stage where linear interactions govern, but as the bed grows further, interactions become predominantly nonlinear such that the instantaneous concentration does not adapt to the equilibrium concentration. So once an unstable bedform will starts growing, it will keep growing exponentially. For this reason the use of Galappatti's depth-averaged solution is to be used with caution in morphological simulations. Toffolon and Vignoli (2007) have as well described some of the stability issues of Galappatti's depth-averaged suspended load solution. Similarly to the previous case Figs. 6.8–6.9 show the corresponding section and top view of the bedform.

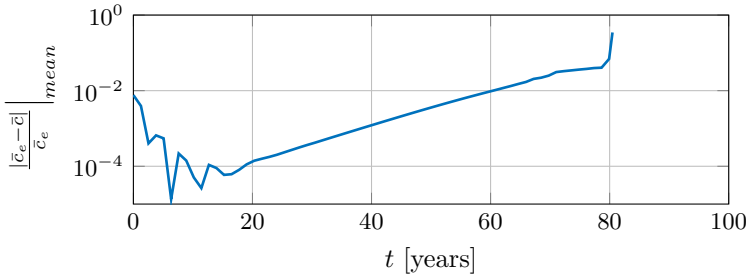

Figure 6.7: Adaption of the instantaneous concentration to the equilibrium concentration during the morphological simulation of B3.

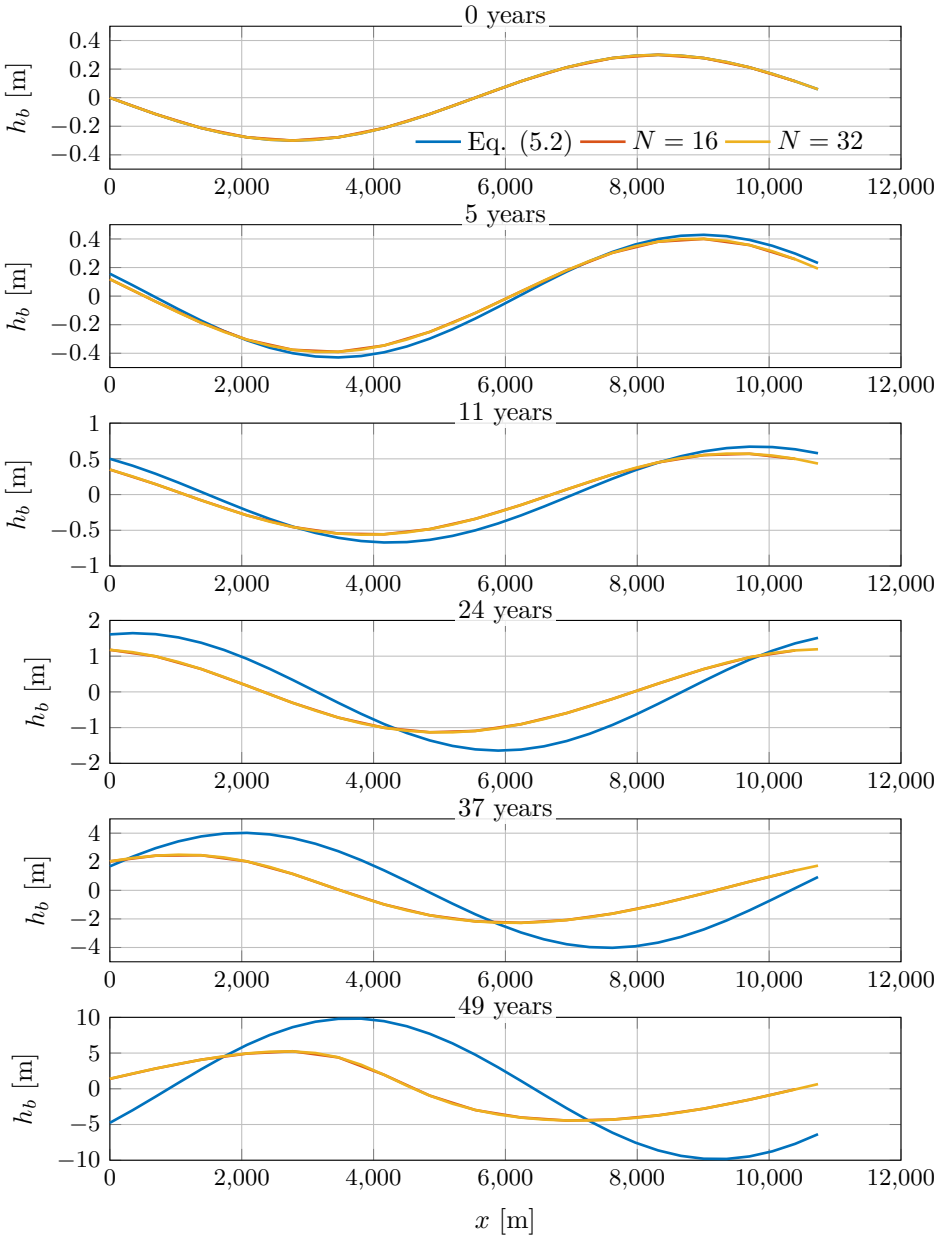

Figure 6.8: Longitudinal section profiles of the bed through center. Case B3.

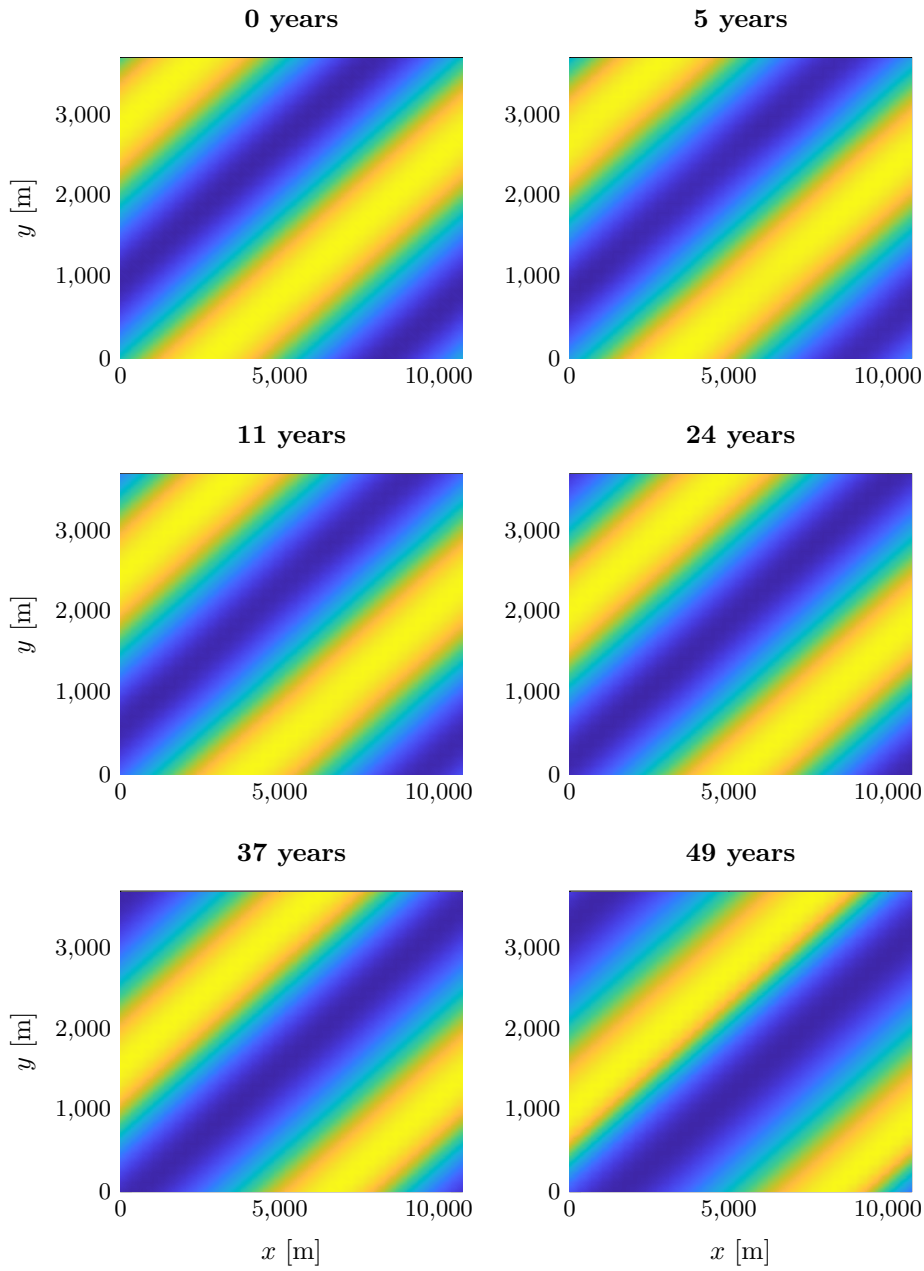

Figure 6.9: Top view of the morphing bed. Blue indicates deeper areas / yellow shallower areas. Case B3.

6.2.2 Random perturbation and varying domain size

One of the shortcomings of numerical simulations is that the imposition of the domain size and the grid density can limit the spectrum of the possible outcomes of the simulation. The simulation is thus limited to include only wavenumbers within the interval of the domain wavenumber and the shortest resolvable wave limited to three grid points here, due to the Orszag 2/3 spectral filter. In the following, the domain size and number of grid points are doubled and quadrupled compared to the previously shown case B1. Instead of prescribing the bedform, a random noise is applied to the bed, as was done in the validation of the alternate bars in the flume (Chapter 4), thus letting the bedform emerge freely. Three types of domain sizes are simulated in the following: 1) corresponding to the wavenumbers of B1 ($k_x h_0 = 0.033$, $k_y h_0 = -0.049$) and resolved with $N = 32$ grid points in each direction, 2) half of the wavenumber i.e. ($k_x h_0/2$, $k_y h_0/2$) resolved with $2N = 64$ grid points in each direction, and 3) a quarter of the wavenumber i.e. ($k_x h_0/4$, $k_y h_0/4$) resolved with $4N = 128$ grid points in each direction. As before, Fig. 6.10 shows the time development of the max bedform

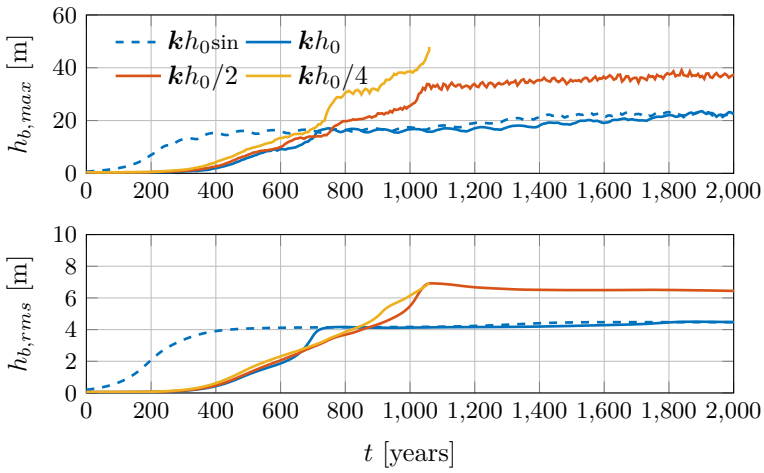

Figure 6.10: Maximum bedform height (max) and root mean square (rms) bed value during the simulation of case B1 with random perturbation. Domain wavenumbers $\boldsymbol{k}h_0 = [0.033\ -0.049]^T$, $\boldsymbol{k}h_0/2$ and $\boldsymbol{k}h_0/4$. Only bed load included.

height and rms value of the bed. It can be seen that the bedform with the same domain size as the previous simulation of B1 with a sinusoidal perturbation ($\boldsymbol{k}h_0$ vs $\boldsymbol{k}h_{0\sin}$), reaches similar height levels (Fig. 6.1). The development time until it reaches equilibrium is longer because it starts from the random noise, so it needs some additional time to generate coherent bedforms, which then start

to grow. This was also the case with the alternate bars validation. There is a short exponential growth initially, but for the most part the growth is linear until eventually leveling off and becoming stable. By doubling the domain size ($\boldsymbol{k}h_0/2$) it can be seen that the bed has a similar development in the growth period (t = 0–700 years), but it then surpasses the shorter domain simulation ($\boldsymbol{k}h_0$) and reaches equilibrium at a higher bed level. This is because additional bedform modes are now included by the larger domain and even though they might have a lower growth rate, they do interact and contribute to yield higher bed levels. When the domain is doubled again ($\boldsymbol{k}h_0/4$), the development is similar to the two previous simulations, but does not become stable, because the combination of the additional waves yields even higher bed levels, eventually leading to the simulation blowing up. This behavior is somewhat expected when considering the growth rate contour of B1 in Fig. 5.12, where wavenumbers close to zero are also inside the growth region of the contours.

The set of Figs. 6.11-6.16 show the sections and top views of the bedforms, for each simulation. Regardless of the simulation considered, the development from flat noisy bed can be described as follows: The earliest coherent patterns to form are of wavenumber $2\boldsymbol{k}h_0$. As the bed continues to develop, the bedforms grow, migrate downstream and merge until eventually the domain wavenumber is prevalent. To explain this behavior, one should consider the migration rate contours for B1 on Fig. 5.17. The contours reveal that the migration is mainly a function of the wavenumber component in x, and increase with larger $k_x h_0$. This means that the shorter the bedform, the faster it will migrate. When the simulation is initiated, none of the modes is given preference (contrary to the case with a sinusoidal perturbation), and hence they all develop simultaneously and interact. In the early stages of the evolution, the emerging bedforms appear nearly symmetrical, but as they grow, a skewness is observed leading to a moderate upstream bedform slope to the crests with an abrupt downslope to the troughs, which resembles a dune shape as previously observed. Since shorter bedforms migrate faster, they merge with the longer bedforms, once they meet at the crests. For the stable bedform emerging with $\boldsymbol{k}h_0/2$ the crest and trough levels are approximately 10 m and -25 m, i.e. total height of 35 m or $1.2h_0$.

As discussed in the previous subsection, the timescales of the development here is in the order of millenniums. The simulations here assume constant steady conditions with infinite boundaries. Thus, in reality there would be many more factors affecting the process along the way, such as alternating flow conditions and possibly boundary effects (land). It is however a good way to get an idea of the order of magnitude of the bedform evolution as well as the intermediate mechanisms. It could be said with some care that from a human time perspective, large-scale bedforms in the sea may appear to be in equilibrium, even if they still haven't reached a stable state.

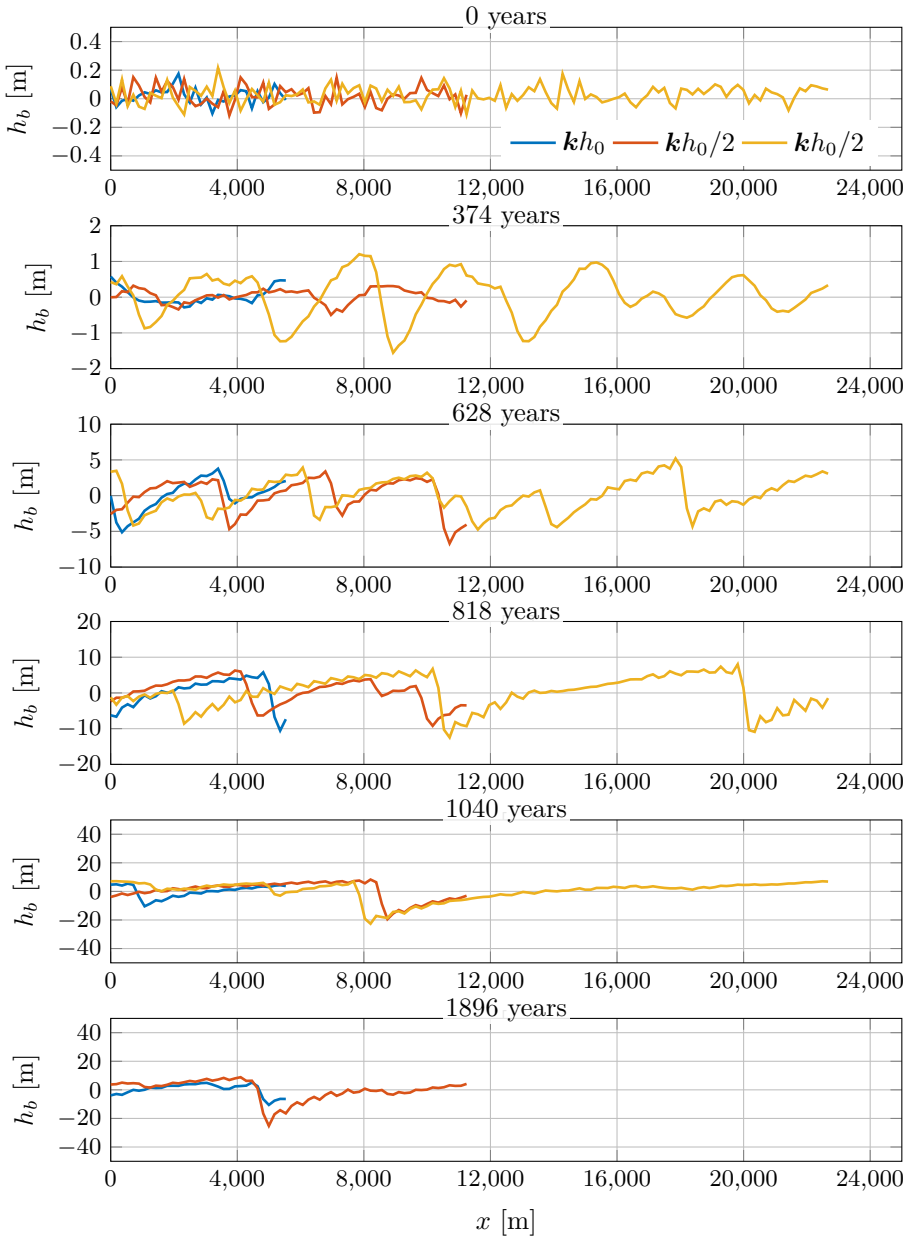

Figure 6.11: Longitudinal section profiles of the bed through center. Case B1 with increasing domain sizes.

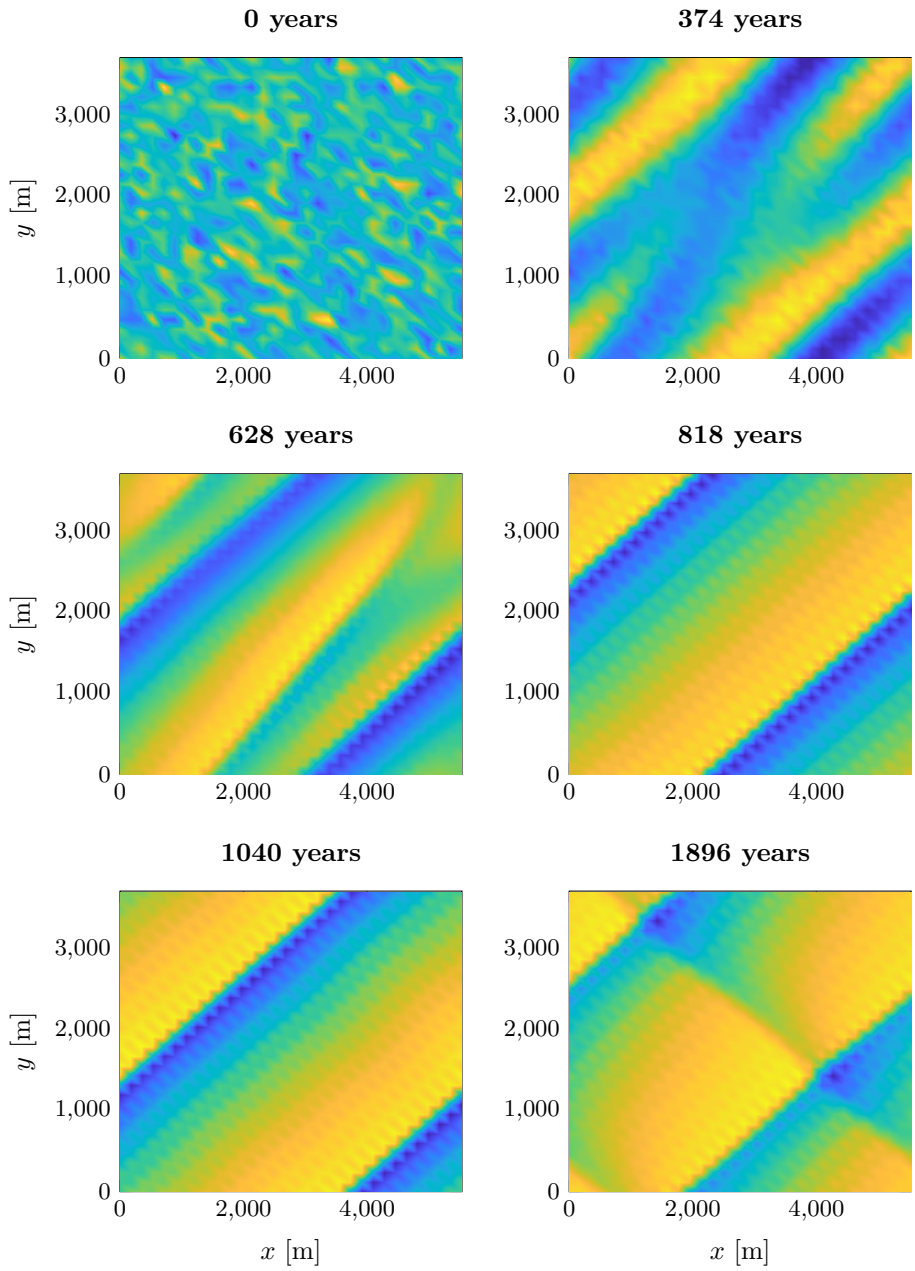

Figure 6.12: Top view of the morphing bed. Blue indicates deeper areas / yellow shallower areas. Case B1 with $\boldsymbol{k}h_0$.

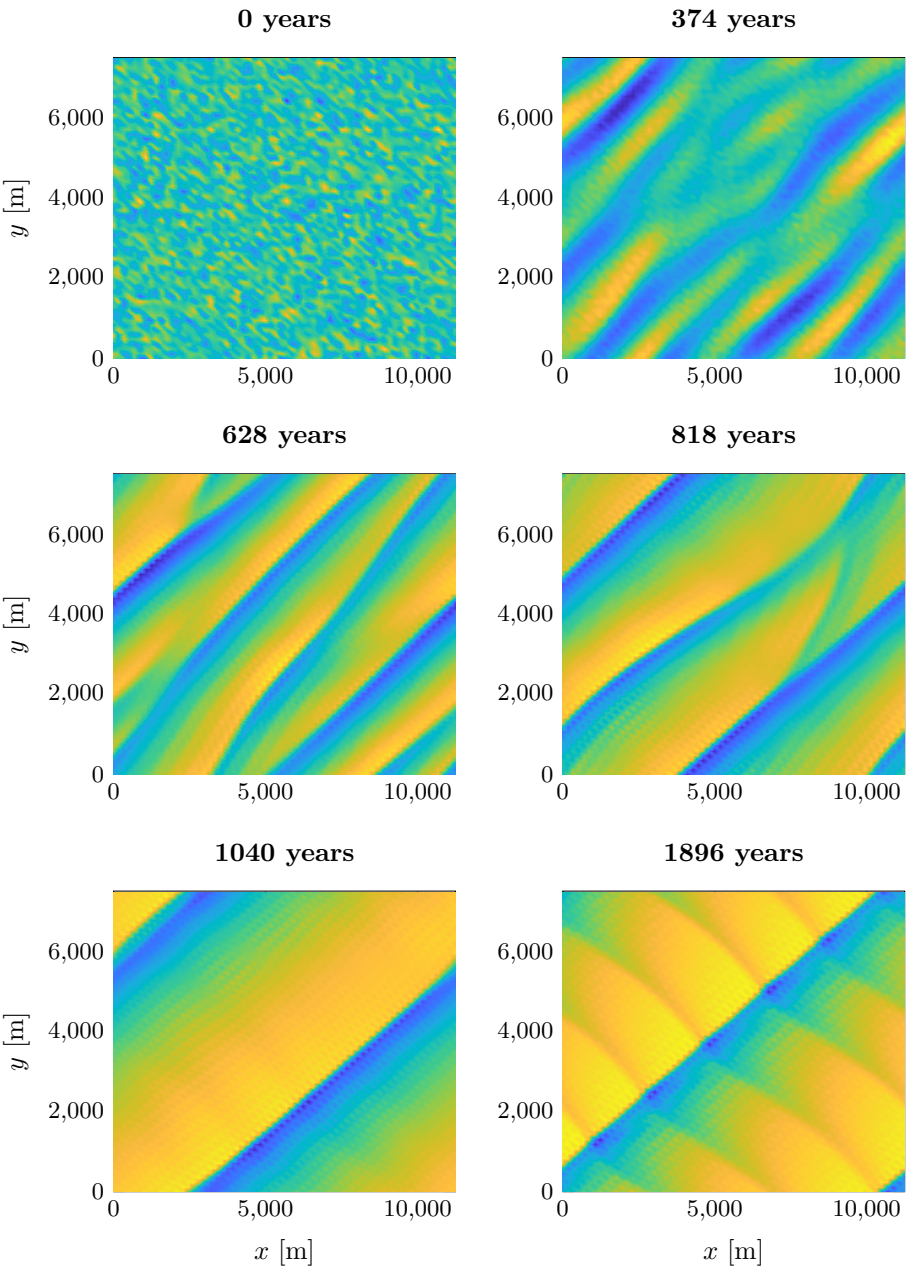

Figure 6.13: Top view of the morphing bed. Blue indicates deeper areas / yellow shallower areas. Case B1 with $\boldsymbol{k}h_0/2$.

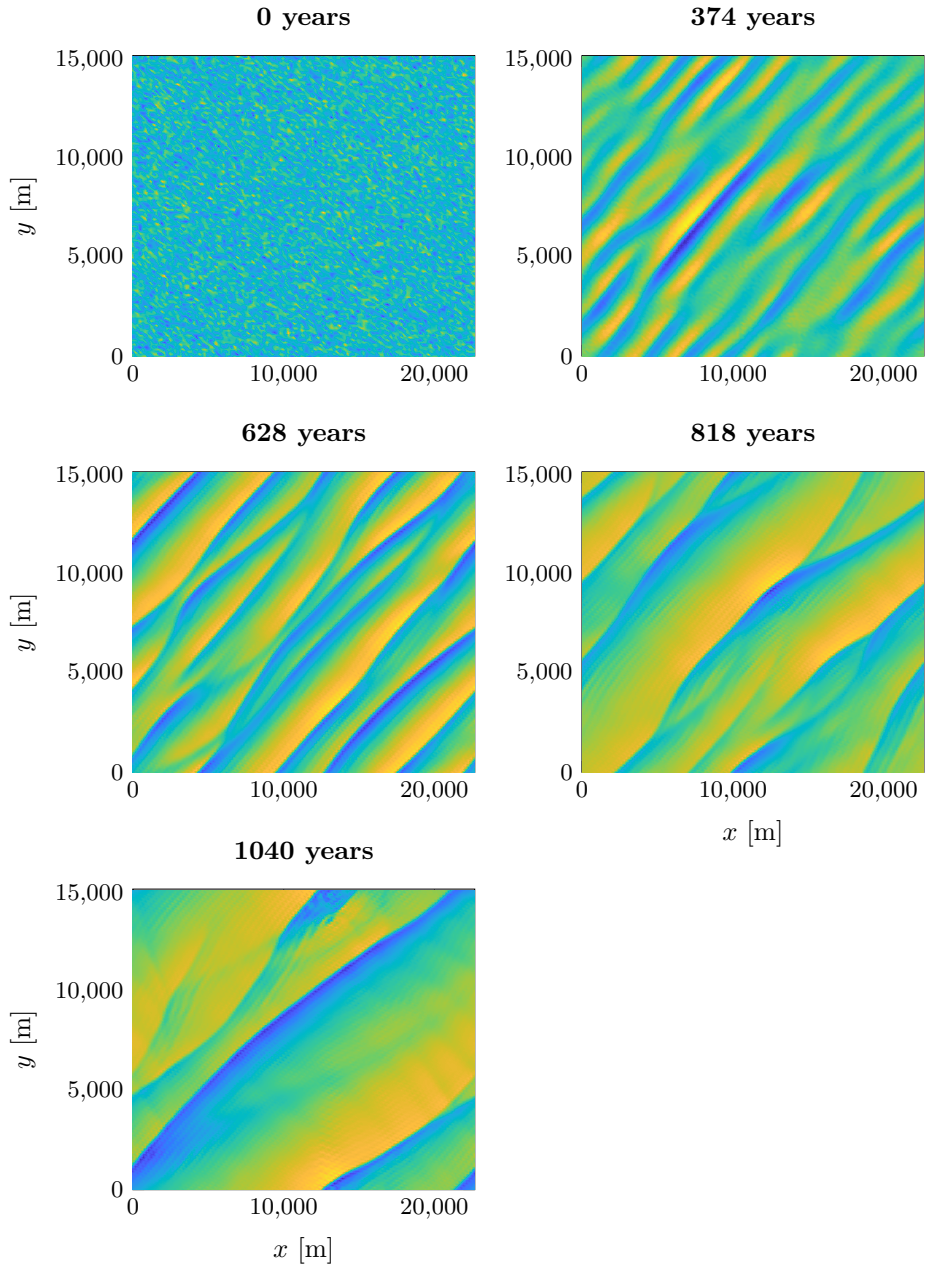

Figure 6.14: Top view of the morphing bed. Blue indicates deeper areas / yellow shallower areas. Case B1 with $\boldsymbol{k}h_0/4$.

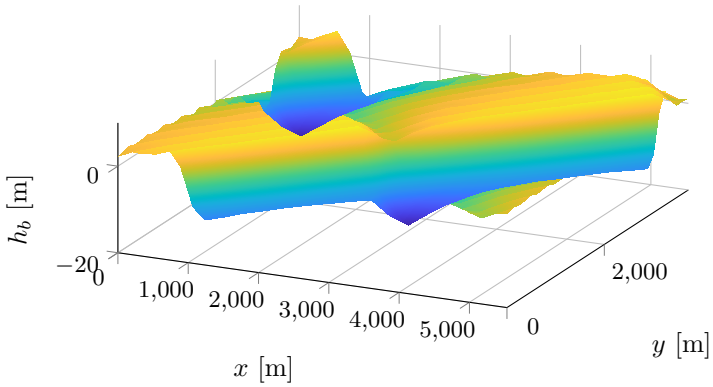

Figure 6.15: 3D view of the developed bedform. Case B1 with $\boldsymbol{k}h_0$.

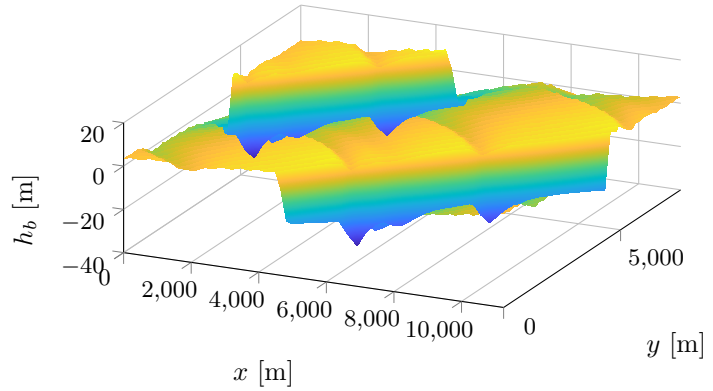

Figure 6.16: 3D view of the developed bedform. Case B1 with $\boldsymbol{k}h_0/2$.

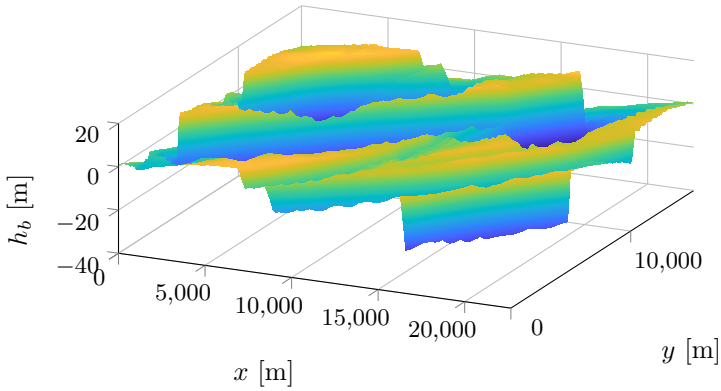

Figure 6.17: 3D view of the developed bedform. Case B1 with $\boldsymbol{k}h_0/4$.

6.2.3 Evolution in tide vs steady current

The simulations conducted so far showed the development of the bedforms under a steady current. As previously discussed, offshore sandbanks' morphology is typically dominated by a tidal current. Recall that the linear stability analysis yielded quantitatively different results between the steady and the tidal currents in terms of the growth rate. In the following it will be studied whether these results carry over to the morphological stage. For comparative purposes the domain utilized is identical to the previous tested B1 ($k_x h_0 = 0.033$, $k_y h_0 = -0.049$) resolved with $N = 32$ grid points, perturbed by the noise and simulated with bed load only. The simulated cases constitute of different combinations of a unidirectional tide and a steady current, applied to the body force (Eq. 5.25) by preceding the input velocities with a weight factor a_w such that the input velocity becomes

$$\bar{u} = U_0 = (1 - a_w)U_c + a_w U_m \sin(\sigma_2 t) \tag{6.7}$$

The amplification of the morphology of 100,000 is applied here as in the previous simulations of B1. This means that each tidal cycle represent a great amount of cycles combined. Another simplification is that it is assumed that the boundary layer is fully developed at all times, and there is no differentiation in velocity and depth like in ebb and flood tides.

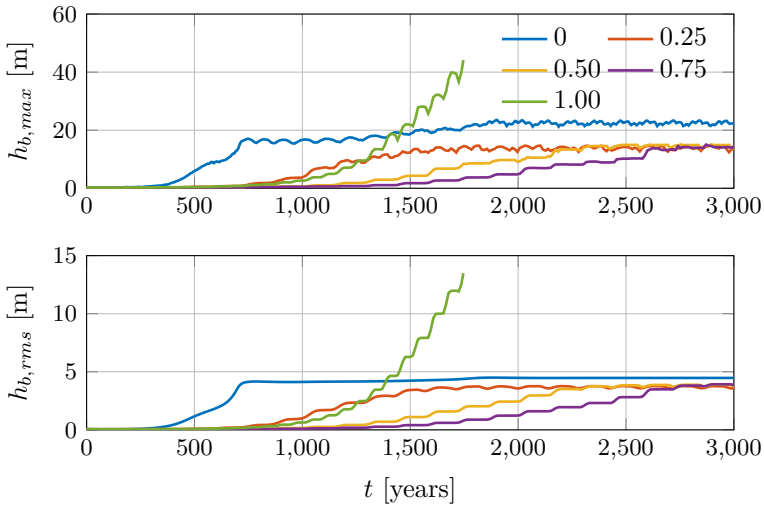

Figure 6.18: Maximum bedform height (max) and root mean square (rms) bed value during the simulation with varying tidal weight factor a_w values. Only bed load included.

Fig. 6.18 shows the time development of the max bedform height and rms value of the bed for five cases, where the weight factor has been varied between a pure steady current $a_w = 0$ (equal to $\boldsymbol{k}h_0$ on Fig. 6.10), combined tide and current $a_w = (0.25, 0.5, 0.75)$, and a pure tide $a_w = 1$. The three simulations that included a current combined with a tide reached an equilibrium bedform height of approximately 15 m. That height is 1 m lower than the bedform height at the temporary equilibrium stage with pure current. In these cases the growth rate of the bedform is reduced with increasing a_w values. This growth rate is correlated with the tides period-averaged velocity, which goes towards zero a_w approaches 1. For all tidal cases the growth has a step pattern caused by the time intervals where the velocity reverses and is either too low to cause sediment transport (whereby the bedforms remain stationary), or simply erode some of the previous cycles growth. Interestingly, the pure tide yielded a step-wise exponential growth that led to a simulation blow up. This is most likely related to it being the only case where the bedform has a period averaged symmetric shape (see Fig. 6.19). Asymmetrical bedforms with steep downslopes are necessary to establish the zero phase between the sediment transport and the bed, which yields pure migration. Thus the symmetrical sinusoidal shape keeps growing exponentially (in much accordance with Eq. (5.2)), because the velocity reversal alters the bedform polarity, whereby a steep downslope is never maintained.

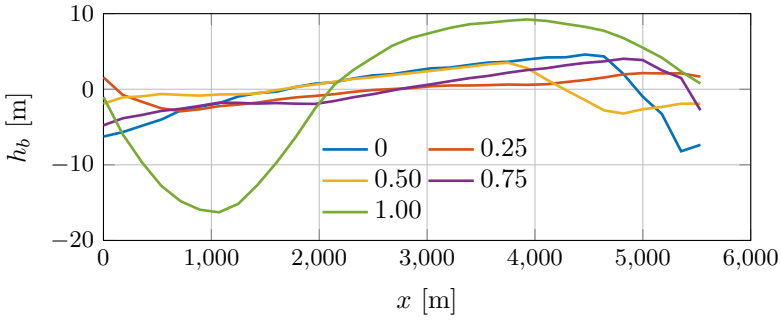

Figure 6.19: Tidal period-averaged bedform sections. Only bed load included.

An interesting feature of the tidal component is that the stability modes vary on the discrete time basis, due to the variation of the velocity over time. Within a tidal period, the system could vary between zero sediment transport, bed load only, or both bed and suspended load. For the above mentioned case B1, a simulation with $a_w = 1$ including suspended load yielded similar results to the one presented for bed load only. On the other hand, when case B3 (peak at $k_x h_0 = 0.049$, $k_y h_0 = -0.081$ on Fig. 5.12) was simulated with suspended load, the bed did not grow at all! This is because the wavenumbers of the peak

mode of the bed load alone (on which the domain size was based) lay outside the positive growth contour of B3 on Fig. 5.13, which includes suspended load. Thus, suspended load that occurs only at the climax of a tidal period, can be sufficient to suppress the bed growth that is driven by bed load in the rest of the tidal period.

6.3 Modeling offshore wind farm effects

The simulations up until this point considered the bedform morphology, confined only by the domain properties. In this section offshore wind farms are added to the puzzle, which makes the matter more complicated. Offshore wind farms are obviously affecting the sea directly by their physical obstruction of the water flows, but also indirectly by affecting the wind field, which is then acting differently on the sea. In this work only the direct obstruction of the water flow is considered.

Offshore wind farms consist of an array of turbines, which are usually aligned in a regular grid. As an example, consider Fig. 6.20, which shows the existing alignment of Horns Rev 1 and 2 as well as the future alignment of Horns Rev 3, located off the west coast of Denmark. Horns Rev 1 covers an area of 20 km^2, at a water depth in the range 7 – 14 m, with a spacing of 560 m between the 2 MW turbines. Horns Rev 3 will cover an area of 88 km^2, at water depths 11 – 19 m, with a spacing of 1.1–1.5 km between 8.3 MW turbines. The spacing is generally a function of the turbines lee wake, hence, as the newly designed turbines become bigger over time, the spacing increases accordingly.

Fig. 6.21 shows some of the sub-aqueous foundation types that an offshore wind turbine could be placed on. As mentioned in the introduction, the vast majority of installations in the north sea are executed with a monopile foundation that is driven into the seabed. Sumer and Fredsøe (1997, 2002) greatly covers the topic of flow around a vertical cylindrical structure and the implications on the nearby seabed. Fig. 6.22 is taken from the work of Roulund et al. (2005), who carried out a detailed study on the flow and scour around a monopile. The figure depicts the flow processes that occur when a monopile obstructs a current, resulting in vortex shedding in the lee side and a horseshoe vortex forming from the monopile front near the seabed. This flow pattern amplifies the bed shear stresses around the monopile, leading to a scour hole forming around the structure, for which scour protection solutions are usually necessary.

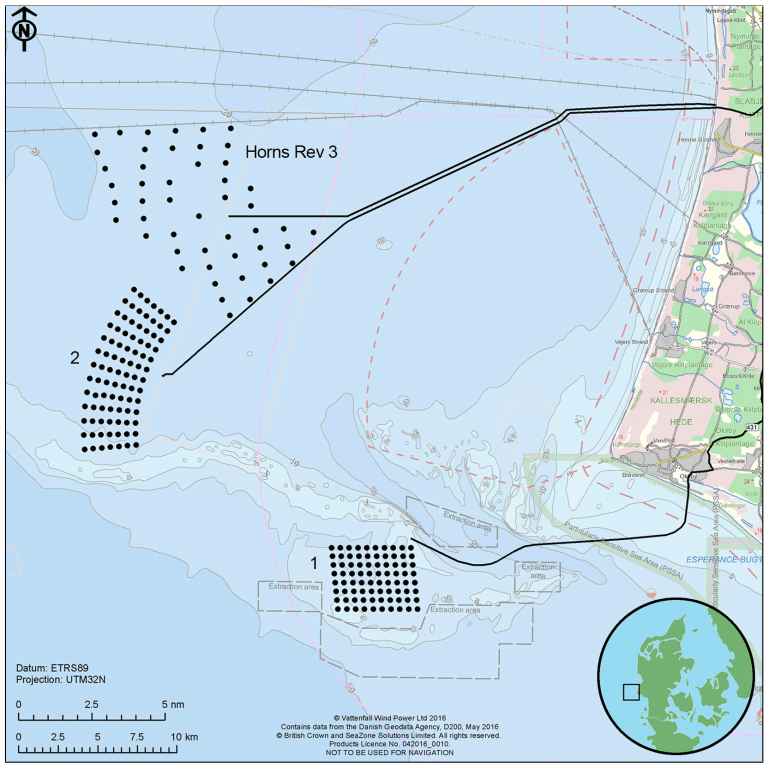

Figure 6.20: Horns Rev wind farms. Credit: Vattenfall (a).

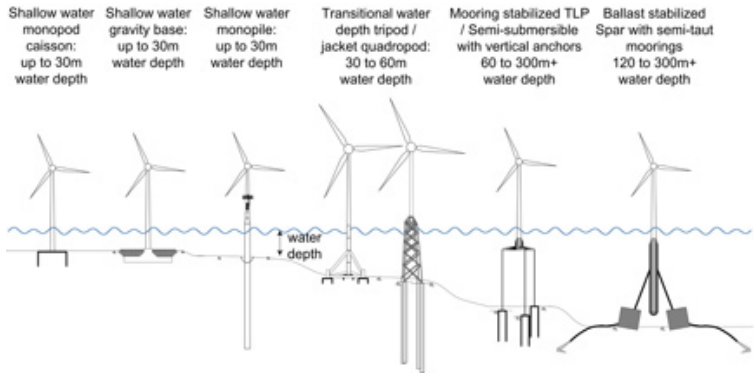

Figure 6.21: Offshore wind turbine foundations. Credit: Schneider.

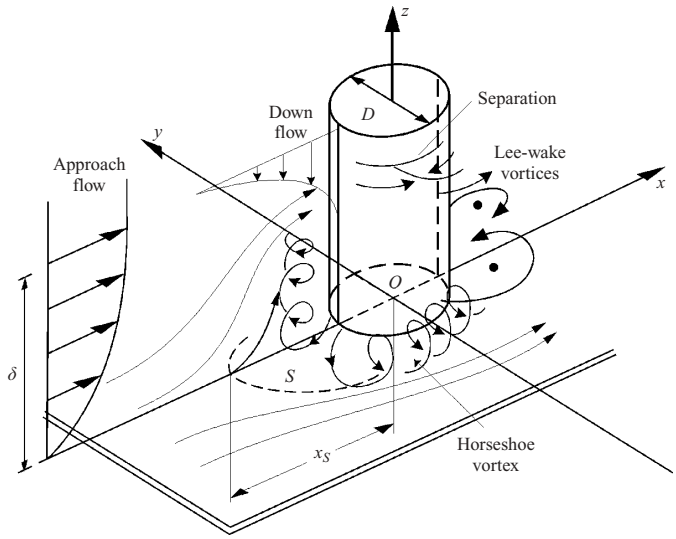

Figure 6.22: Flow around a pile. Credit: Roulund et al. (2005)

6.3.1 Representation of monopiles in the 2DH model

Modeling the flow around a cylinder in a manner that captures the details shown in Fig. 6.22 requires a fine 3D mesh with the full set of Navier-Stokes equations applied in a computational fluid dynamics (CFD) model. For the time and length scales considered in the present 2DH shallow water model, it is practically impossible to obtain such an accuracy for each monopile. Scour hole characteristics are generally a function of the flow and monopile diameter, and evolve on the timescale of hours to days. On the other hand, large-scale bedforms operate over time- and length-scales that are several orders of magnitude larger, as the previous simulations indicated. The monopiles are incorporated into the model by estimating their overall subgrid resistance, because the numerical grid used to model the sandbanks is too coarse to resolve individual monopiles.

To estimate the subgrid resistance from each monopile, a semi empirical formula that obtains the force that a fluid exerts on a cylinder is used:

$$F_M = \frac{1}{2}\rho C_M D_M U^2 \tag{6.8}$$

where U is the incoming flow velocity, D_M is the cylinder diameter and C_M is the drag coefficient of the structure. Sumer and Fredsøe (1997) have compiled curves of this drag coefficient as a function of the monopile Reynolds number UD_M/ν.

The above subgrid level force, is incorporated into the 2DH model by diffusing it over a grid-cell-area, yielding the relation

$$A_e = n_M \frac{D_M h}{\Delta x \Delta y} \tag{6.9}$$

where n_M are the number of monopiles within $\Delta x \Delta y$ in a given cell. Eq. (6.8) is now modified into a set of drag equations given by

$$S_{M,x} = -\frac{1}{2} C_M A_e \bar{u} |\boldsymbol{u}| \tag{6.10}$$

$$S_{M,y} = -\frac{1}{2} C_M A_e \bar{v} |\boldsymbol{u}| \tag{6.11}$$

which are added to the respective depth-averaged momentum equations (3.2) – (3.3). The monopiles drag coefficient C_M is generally of O(1) for $|\boldsymbol{u}| D_M/\nu > 100$, with a temporary drop to 0.5 when the Reynolds number reaches $3 \cdot 10^5$. With $U = 1$ m/s, $\nu = 1.3 \cdot 10^{-6}$ and $D_M = 4$ – 10 m, the Reynolds number is in the range $5 \cdot 10^6$ – 10^7. It is questionable how much an accurate description of the drag coefficient would contribute to the overall results with the above incorporation of the monopile effects. Thus, to be on the conservative side, a constant value of 1 is used regardless of the value of $|\boldsymbol{u}| D_M/\nu$.

In a confined study with imposed boundary conditions the monopiles would be applied as a subgrid cluster in a limited area of the domain, whereby it acts similarly to a porous zone in the affected cells. The present implementation of the model with periodic boundaries does not allow the inclusion of an entire wind farm to a certain area, but instead the domain represents a part within the theoretically infinite wind farm. Therefore, the computational grid is made fine enough to resolve the spacing between the monopiles, whereby a smaller segment can be simulated utilizing the periodic boundaries.

The following shows the implication of the above-mentioned monopile implementation on the flow and the resulting bed. Figs. 6.23 depicts the flow velocity and sediment transport vectors around a subgrid monopile marked in red, and Fig. 6.24 shows the bed and rate of bed level change in a stream-wise section through the monopile. The monopile resistance causes the incoming water to decelerate in front and divert the streamlines around. As a result, it generates a negative gradient in the sediment transport, which through the Exner equation (3.89) makes the bed grow. The acceleration of the water as it passes the monopile creates the opposite effect, whereby the bed is eroded. The disadvantage of this approach is that it appears to overestimate the extent to which the monopile is affecting the surroundings, but for a large-scale study on the much larger bedforms it can give indications of the overall effects.

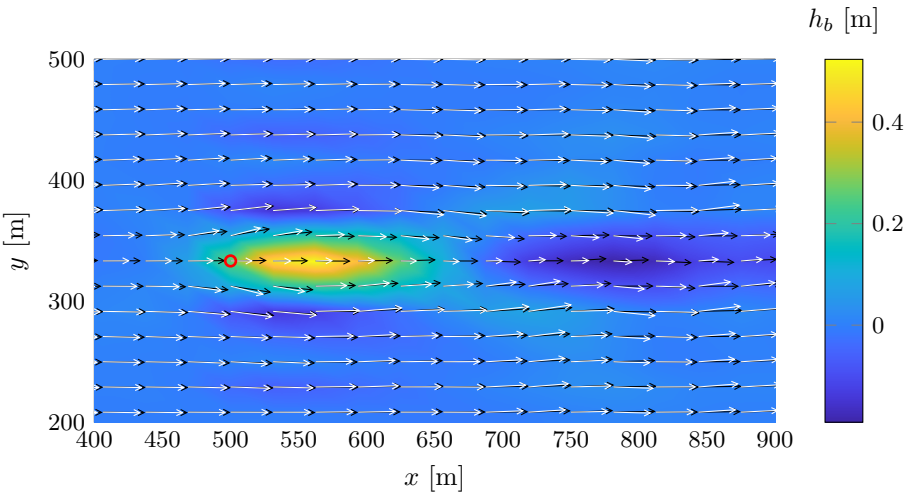

Figure 6.23: Bed level h_b, flow (Black vectors) and sediment transport (White vectors) around monopile indicated by the red circle. The y component of the vectors is amplified by a factor 5 for a clearer visualization.

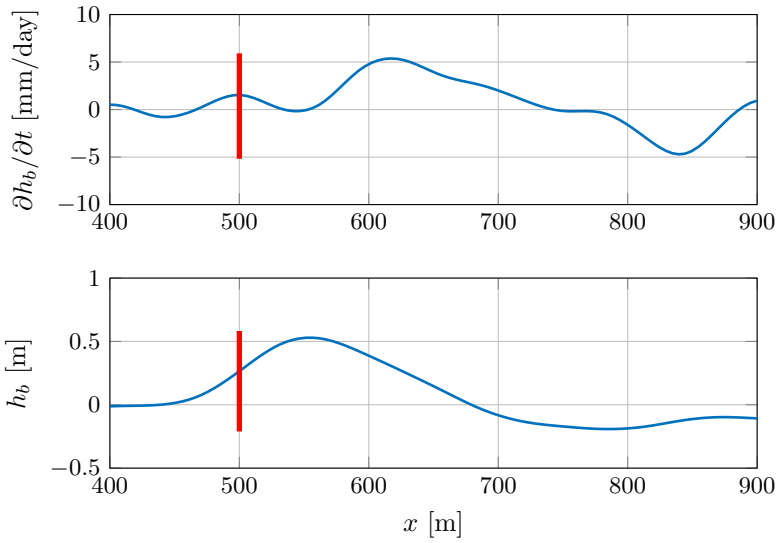

Figure 6.24: Rate of bed level change and bed level at longitudinal section through the monopile (indicated by the red line).

6.3.2 Effects of wind farms on sandbanks morphology

In section 6.2 it was found that the domain size influences the outcome of the bedforms and that an asymmetric tide yields qualitative similar results to a steady current. In the following, a qualitative study is conducted with respect to the wind farms effect on large-scale bedforms. The attempt is not on establishing the exact final bedforms, but rather compare situations with and without the wind farms. For a comparison to be valid, each simulation must be conducted with the same domain wavenumber and initial conditions, while varying only the monopile spacing.

Three scenarios with wind farms are studied: 1) Monopiles introduced onto an already established sandbank, 2) monopiles introduced onto a flat bed perturbed with noise, and 3) a single monopile on a flat unperturbed bed. To maximize the effect of the wind farms, a conservative monopile diameter $D_M = 8$ m is used in all simulations. Flow is simulated as a steady current and as previously, only bed load is considered. The results are studied in a similar manner to the way employed in the previous section, where the max bedform height and rms value of the bed are presented for each simulation, supplemented by plots of the bedforms.

6.3.2.1 Wind farms on existing sandbanks

The stable bedform that emerged in the simulation labeled $\boldsymbol{k}h_0$ in section 6.2.2, is used in the following as an initial bed condition to study the effects of a wind farm on an already established bedform. Tab. 6.1 shows the parameters of the simulations. The grid is resolved with $N = 64$ grid points in each direction. Three simulations are conducted with horizontal distance between the monopiles given by $\Delta M = (714, 1428, 2856)$ m. These spacings are chosen because they are divisors of the domain length in x, and thus fulfill the periodicity in that direction. In the y direction the periodicity is not repeated correctly, but in order to compare to the known development, the length cannot be modified. The simulation results are not expected to be largely affected by the latter, because the flow and transport are predominantly directed in x.

Table 6.1: Parameters for monopiles on existing sand banks simulations.

h_0	U_0	C_{D0}	d_{50}	D_M	L_x	L_y
m	m/s	-	mm	m	m	m
30	1.0	0.001781	0.250	8	5712	3847

From Fig. 6.25 it can be seen that the closer the monopiles spacing, the more

the bedform is affected. The bedform establishes an oscillatory equilibrium pattern with the max bedform height increasing by 0.5 m for $\Delta M = 2856$ m, 1 m for $\Delta M = 1428$ m and 6 m for $\Delta M = 714$ m, i.e. an increase of up to 30%. Essentially the monopiles introduce an increased flow resistance to certain areas, so the bed modes adapt to the new conditions. The denser the monopile grid, the more uniform the resistance becomes, which is then similar to simply increasing the overall drag coefficient, as was done in the parametric study of the linear stability analysis in Chapter 5. Fig. 6.27 shows that the most pronounced effect is that the monopiles slow down the migration rate of the bedform, as the distance between them reduces. In term of the expressions in Eqs. (5.10) and (5.11) the introduction of monopiles on the equilibrium sand bank increases the phase ϕ from zero, causing the bedform to grow and reduce the migration speed. Fig. 6.27 shows that regardless of the monopile spacing, the large bedform maintains its overall shape. Thus also the regions which do not cross through a monopile are slowed down. Furthermore, on both figures there is a slight visible local effect from each monopile, increasing with decreasing monopile spacing. The development timescales in this conservative simulation are fortunately still on the order of centuries, so considering the 25 – 30 year lifespan of wind farms it suggests that the effect on sandbanks is negligible. A different alignment of the wind farm array relative to the flow direction has yielded the same conclusion in other simulations.

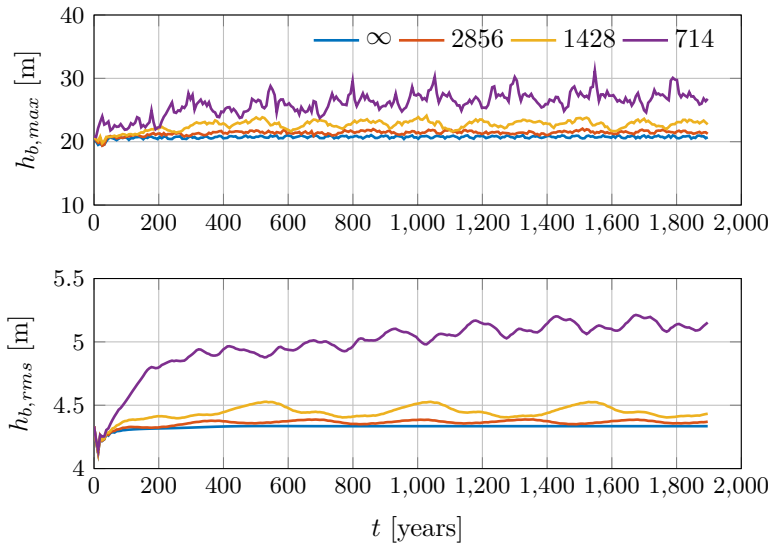

Figure 6.25: Maximum bedform height (max) and root mean square (rms) bed value during the simulation with ΔM meters between monopiles. Initially developed bedform and mean depth $h_0 = 30$ m.

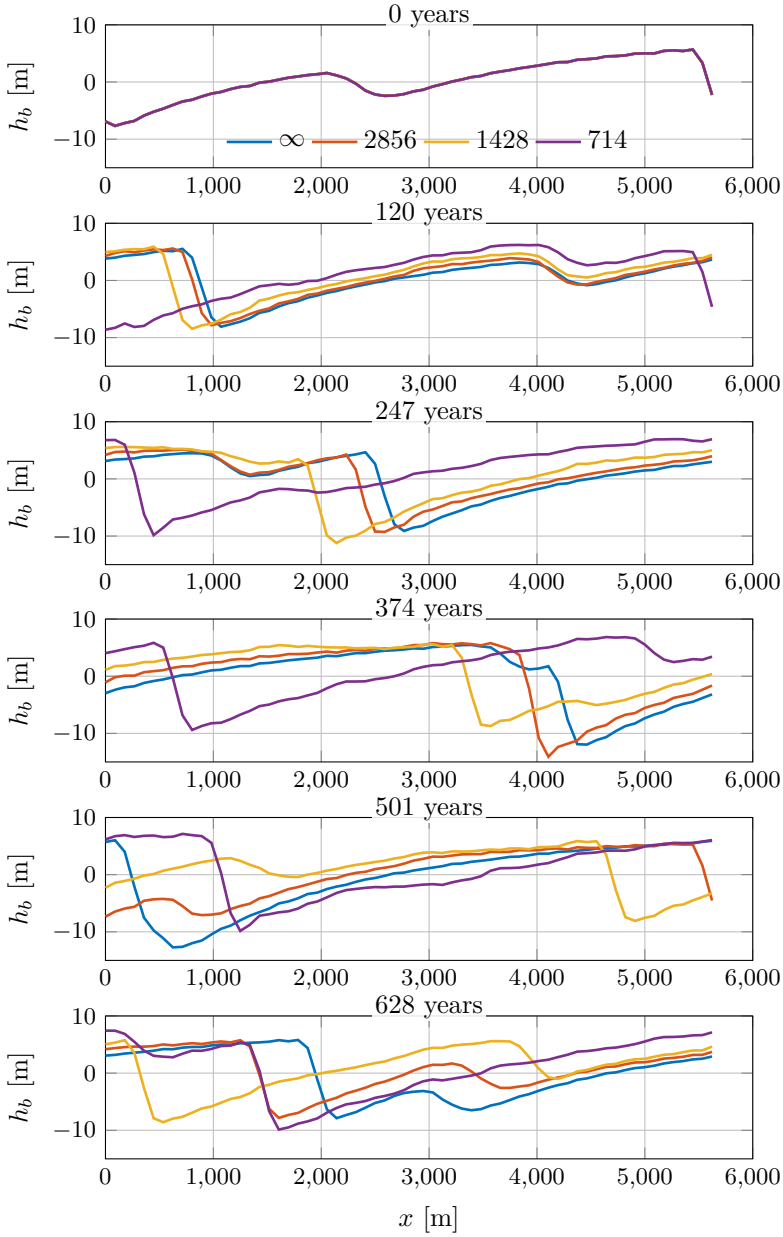

Figure 6.26: Bed levels in a stream-wise section through $y = 2885$ m with ΔM meters between monopiles.

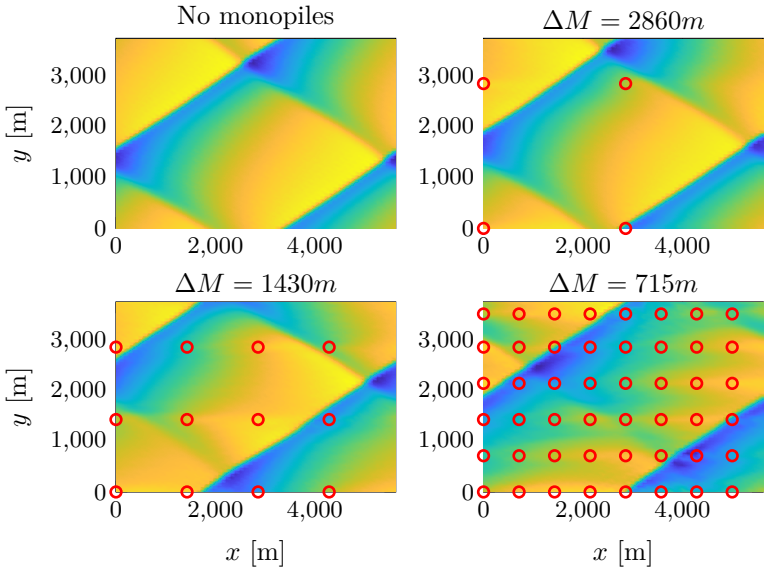

Figure 6.27: Fully developed bedforms. Red circles indicate monopile positions and ΔM the distance between monopiles.

6.3.2.2 Wind farms on perturbed flat bed

Another test is now conducted on a flat bed perturbed by a noise. A shallower depth $h_0 = 10$ is used to see the effect on the length- and timescales, while the domain wavenumber is set to $k_x h_0 = 0.049$, $k_y h_0 = 0.049$. With the rest of the simulation parameters in Tab. 6.2, this gives a Froude number of 0.10, for which there is no linear stability contour, but it is within the proximity of the investigated cases. Several monopile spacings given by $\Delta M = (160, 320, 640)$ m are tested, for which the periodicity matches in both horizontal directions. These spacings purposely go below realistic values, in order to probe the limits.

Table 6.2: Parameters for monopiles on perturbed flat bed simulations.

h_0	U_0	C_{D0}	d_{50}	D_M	L_x	L_y
m	m/s	-	mm	m	m	m
10	1.0	0.001781	0.250	8	1282	1282

Fig. 6.28 shows the bed level development over time and Fig. 6.29 shows the shape of the fully developed large scale bedform. The presence of the monopiles on the flat unstable bed now has a major effect on the initial growth pattern and the equilibrium form. Initializing the simulation in this manner with an

unstable bed and monopiles, generates a shock for the system, visualized by the rapid growth and oscillatory pattern of the bed level curves. This is caused by the bed humps forming on the lee side of the monopiles, which grow fast and reach an equilibrium level in an early stage. Meanwhile, the large-scale bedform, (which also develops without the monopiles) starts forming and growing in a slower pace. The final shape of the bed is highly affected by the spacing between the monopiles. The large scale bedform is still visible in all cases, however, it appears to be scoured in the lateral space between the monopiles.

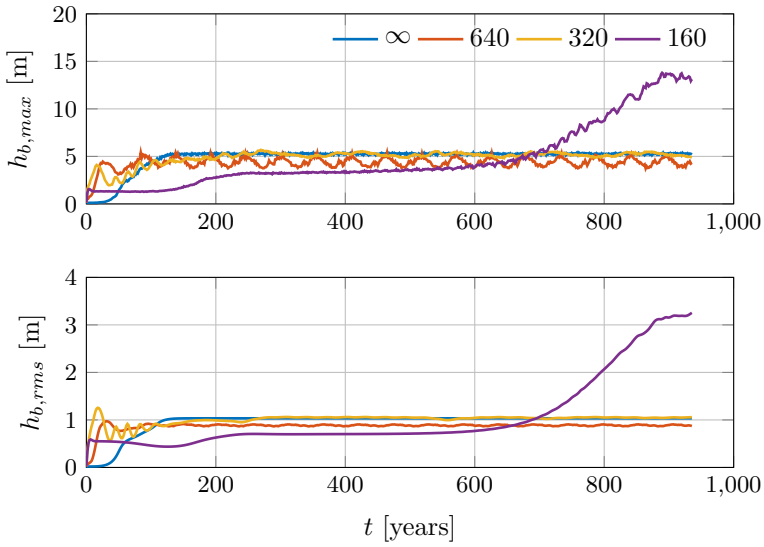

Figure 6.28: Maximum bedform height (max) and root mean square (rms) bed value during the simulation with ΔM meters between monopiles. Initial flat bed and mean depth $h_0 = 10$ m.

6.3.2.3 Monopiles as perturbation

Some wind farms that are located at shallow tidal inlets can experience a great variation in the water depth, and they might experience bedforms emerging because of the monopiles. These bedforms are perpendicular to the flow direction, as characteristic for sandwaves, which the 2DH model is not able to simulate. However, with less emphasis on the correct emerging bedform, a test is still made with a steady current at a very shallow water depth of $h_0 = 5$ m. The purpose of this simulation is to test whether a monopile could perturb a flat bed, and over what timescale. The parameters of the simulation are listed in Tab. 6.3. In this case a single monopile is placed within a domain of size 1×1

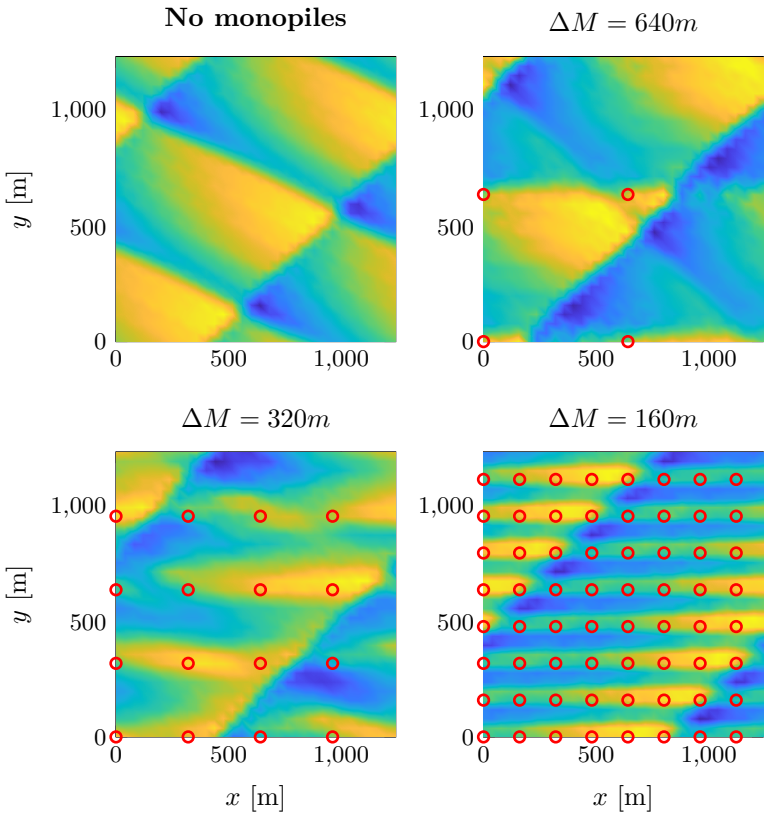

Figure 6.29: Fully developed bedforms. Red circles indicate monopile positions and ΔM the distance between monopiles.

km, which means a monopile spacing of 1 km, and compared to an identical domain without a monopile and perturbed with bed noise. From Fig. 6.30 it can

Table 6.3: Parameters for monopiles on existing sandbanks simulations.

h_0	U_0	C_{D0}	d_{50}	D_M	L_x	L_y
m	m/s	-	mm	m	m	m
5	1.0	0.001781	0.250	8	1000	1000

be seen that the domain perturbed by the single monopile, causes the bedform to initiate growth earlier and also grow at a faster rate. However, eventually the simulations reach a similar bedform height in equilibrium. An interesting feature of this comparison is seen on Fig. 6.31, which shows a top view of the bed development for the two cases. It appears that while the undisturbed flow

gave rise to a bedform with the domain wavenumbers, the flow perturbed by the monopile yielded a factor 2 in the lateral wavenumber, i.e. the monopile "pushed" the flow to prefer a different equilibrium bedform length, while the equilibrium height was similar. It is also interesting to notice that the development of these bedforms occurred over a time span of 10 – 20 years, which make them very relevant for wind farm design.

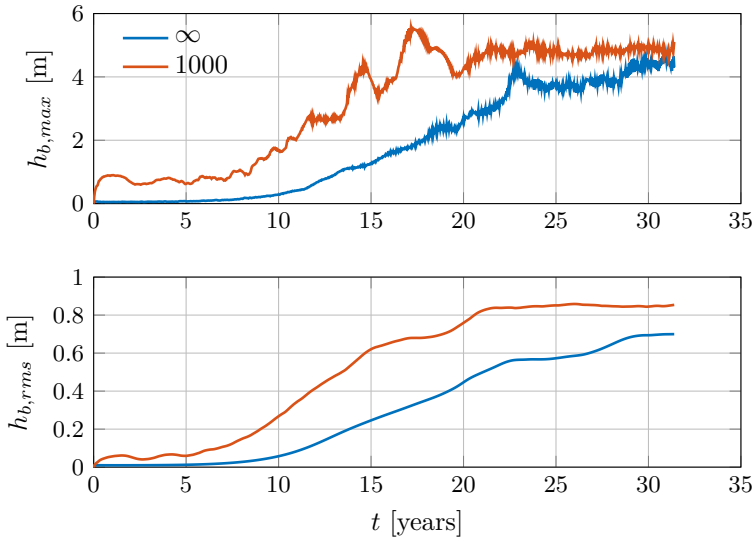

Figure 6.30: Maximum bedform height (max) and root mean square (rms) bed value during the simulation with ΔM meters between monopiles. Initial flat bed and mean depth $h_0 = 5$ m.

6.4 Closing remarks

This chapter has shown that the growth rate of the large-scale bedforms in their early morphological development, is well predicted by the linear stability analysis. However, the finite bedform length and height is sensitive to the domain configuration due to nonlinear mode interactions in the morphological stages. This means that the linear stability analysis is most useful for identification of the role that the different parameters play in the simulation, and for revealing the unstable wavenumber space where bedforms are likely to emerge. The migration rate of the bedforms is greatly overestimated by the linear stability analysis, but is useful when comparing migration magnitudes and direction for

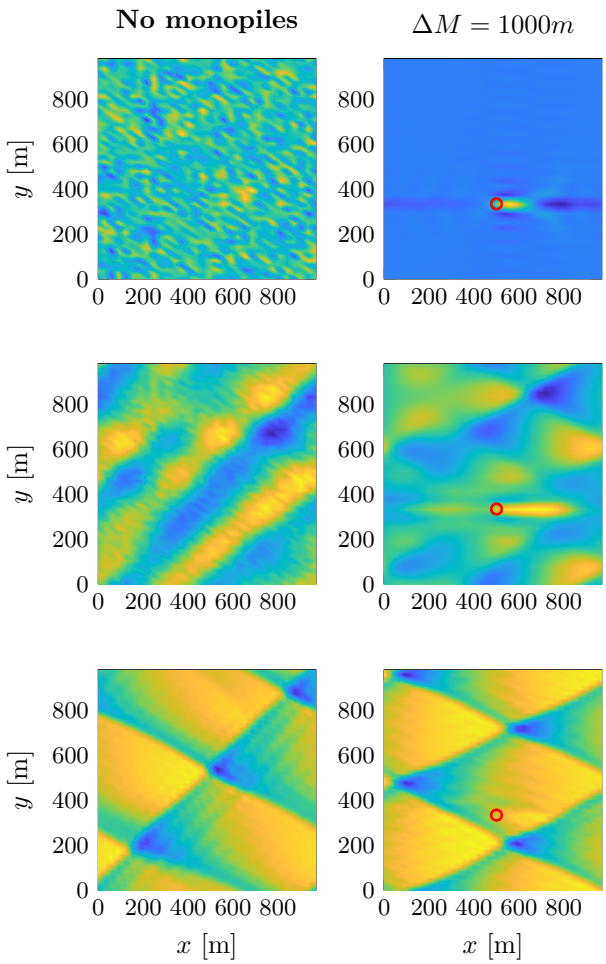

Figure 6.31: Fully developed bedforms. Red circles indicate monopile positions and ΔM the distance between monopiles.

different wavenumbers. Suspended load increases the growth rate of bedforms, but its implementation with Galappatti's depth-averaged model is not suitable for advanced morphological stages with periodic boundaries as it becomes unstable. Replacing Galappatti's model with an equilibrium suspended load model, would neglect the phase difference between the suspended load and the bed shear stress. This phase difference is the most important qualitative contribution of the suspended load to the calculation. Hence, it was unfortunately not possible to perform morphological simulations with suspended load. Nonetheless, using bed load only, it was possible to show the qualitative bedform behavior with

respect to the domain size and the morphological similarities between different cases with current-plus-tide flows. The processes that lead to bedform growth and maintenance match the description of the mechanisms in Chapter 2. An interesting feature was noticed when the flow was a pure symmetric tide. Then the bedform kept growing until blowing up the simulation, because the symmetrical oscillatory flow kept deforming the established equilibrium shape with each flow reversal. On the other hand, all cases with current-plus-tide yielded the same finite stable bedform. The simulations were all performed at a mean depth 30 m, mean flow velocity of 1 m/s and mean grain diameter of 0.250 mm to represent reasonably realistic values in the north sea. With these parameters all the above-mentioned effects happen over timescales of decades to centuries.

To study how large-scale bedforms interact with offshore wind farms, monopiles at various spacings were added to the periodic domain to simulate a smaller part within a theoretically infinitely long wind farm. The implementation of the wind farm effects is done by adding flow resistance to certain subgrid points that symbolize the monopiles. This is suitable for cases where the ratio of the effective flow-resisting-area of the monopile to grid-cell-area $D_M h/\Delta x \Delta y \ll 1$. The validity of the results when the latter doesn't hold would be more questionable. For established sandbanks at intermediate depths, it seems that with realistic monopile spacings there is no practical concern regarding the effect on the stability of the sandbank. The sandbanks are migrating at extremely low rates, and the wind farm actually reduces this rate even further. As the distance between monopiles is reduced, the overall flow resistance in the domain becomes more uniform because it covers most of the grid cells. This is somewhat equivalent to an overall increase of the the drag coefficient, as done in the parametric study of Chapter 5. By and large, it can be said that increased flow resistance yields higher sandbanks, including when the increased resistance is caused by monopiles. On the other hand, the sandbanks migration rate is lowered by wind farms. It is not clear how the additional suspended load seen in the plumes of Thanet wind farm (Fig. 1.3), would affect the bedforms as it requires detailed 3D modeling. It could be speculated that it would stabilize the bed as suspended load has shown to suppress the growth of shorter wavelengths. This cannot be modeled in a 2DH model, but might also not be of great structural importance as the extent of the plume could indicate that the suspended material consists mainly of very fine sand and silt. On the basis of this it appears that offshore wind farms at intermediate depths have minor effects on the development of sand banks.

A conceptual simulation showed that at a depth of 5 m, a wind farm could perturb a flat bed and form migrating bedforms. This scenario is most likely better simulated in a 3D model, because empirical evidence suggests that the emerging bedforms around wind farms are sandwaves and hence need a vertical grid to be modeled numerically. The timescale of sandwaves morphology is more

on par with the lifespan of wind farms and should therefore probably be the main concern. In the next chapter a developer version of the three-dimensional model MIKE 3 by DHI, is used to explore some possibilities for extension of the study.

Chapter 7

Exploring three-dimensional modeling options

In this chapter a three-dimensional model with is used to explore the feasibility of the model to simulate large bedforms in the order of sandwaves, and their interaction with resolved monopiles. First, a brief description of the model is presented, followed by a model validation using the backfilling trench from Chapter 4. Then a few simulations of sandwave morphology are shown and the chapter ends by presenting preliminary results of a scour hole developing around a monopile as well as sandwaves migrating past a monopile.

7.1 Introductory remarks

Up until this point the thesis dealt with large-scale bedforms in a depth-averaged model. These bedforms were shown to be slowly morphing over centuries and only affected to a limited degree by construction of offshore wind farms. In order to study the three-dimensional effects together with more active bedforms such as sandwaves, the model has to include the vertical discretization in addition to the horizontal. Extending the 2DH model to account for this would be extremely time consuming, so it is therefore decided to use a commercial model for the task, namely MIKE 3 Wave FM by DHI. Some of the questions that arose

during the work with the 2DH model were how exactly a sandwave is affected by a monopile, i.e. does it break? change orientation? slow the migration rate or continue uninterrupted? Also, would a monopile change the local flow conditions enough to initiate the generation of bedforms? Scour studies around monopiles show the accumulation of the eroded material downstream of the hole. Hence, under what conditions would this material be washed out or start forming a stable series of bedforms? Due to time limitations, this chapter does not provide explicit answers to these questions, but instead explores the possibility to answer them with a three-dimensional model. The intention is to conduct the simulations with true length- and timescales. Such scales are not realistic in traditional CFD modeling, but as this chapter shows, the utilized model has a great potential in future use.

7.2 Model

MIKE 3 Wave FM is a three-dimensional σ-coordinate model with non-hydrostatic pressure terms. It is a not yet released extension of the commercial MIKE 3 FM software. Although its development aimed primarily at simulating the morphodynamics under surface waves, this chapter shows that it performs well with pure current as well. Fig. 7.1 shows a definition sketch of the model conventions. The vertical resolution is based on division of the water column into bed-following σ-layers. Notice that here the zero level of the z coordinate is defined at the still water depth elevation denoted H. The total water depth is then given by $h = H + \eta$. The full model solves the three-dimensional incompressible Reynolds averaged Navier Stokes (RANS) equations, with continuity, salinity, temperature, density gradients and a turbulence close model. For a detailed description of the model, the reader is referred to DHI (2013a). In the following, a brief overview of the parts with relevance to the conducted simulations is presented.

7.2.1 Hydrodynamics

The model is implemented on a transformed coordinate system defined by

$$x' = x, \quad y' = y, \quad \sigma = \frac{z + H}{h} \tag{7.1}$$

which means that σ is the vertical coordinate going from 0 at the bed to 1 at the surface. This transformation implies the following relations for the spatial

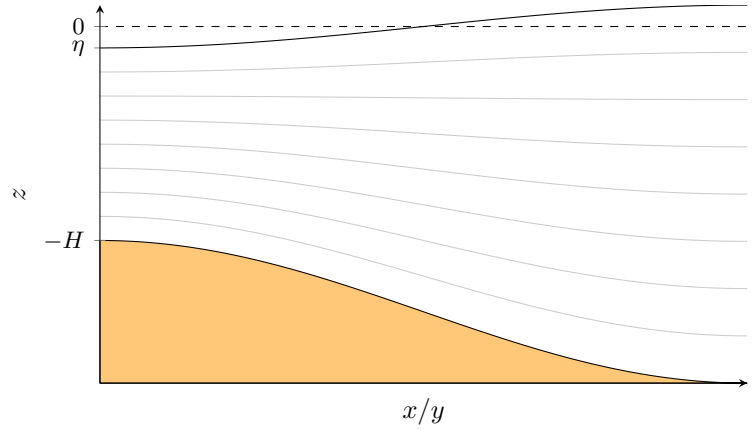

Figure 7.1: Domain conventions in MIKE 3 with σ layers represented by the gray lines.

gradients

$$\frac{\partial}{\partial x} = \frac{\partial}{\partial x'} - \frac{1}{h}\left(-\frac{\partial H}{\partial x} + \sigma\frac{\partial h}{\partial x}\right)\frac{\partial}{\partial \sigma} \tag{7.2}$$

$$\frac{\partial}{\partial y} = \frac{\partial}{\partial y'} - \frac{1}{h}\left(-\frac{\partial H}{\partial y} + \sigma\frac{\partial h}{\partial y}\right)\frac{\partial}{\partial \sigma} \tag{7.3}$$

$$\frac{\partial}{\partial z} = \frac{1}{h}\frac{\partial}{\partial \sigma} \tag{7.4}$$

The continuity and momentum equations in the transformed coordinates are thus defined by

$$\frac{\partial h}{\partial t} + \frac{\partial hu}{\partial x'} + \frac{\partial hv}{\partial y'} + \frac{\partial h\omega}{\partial \sigma} = 0 \tag{7.5}$$

$$\frac{\partial hu}{\partial t} + \frac{\partial huu}{\partial x'} + \frac{\partial hvu}{\partial y'} + \frac{\partial hu\omega}{\partial \sigma} = -gh\frac{\partial \eta}{\partial x'} - \frac{h}{\rho}\frac{\partial p_{dyn}}{\partial x'} + \frac{\partial}{\partial \sigma}\left(\frac{\nu}{h}\frac{\partial u}{\partial \sigma}\right) + hF_u \tag{7.6}$$

$$\frac{\partial hv}{\partial t} + \frac{\partial huv}{\partial x'} + \frac{\partial hvv}{\partial y'} + \frac{\partial hv\omega}{\partial \sigma} = -gh\frac{\partial \eta}{\partial y'} - \frac{h}{\rho}\frac{\partial p_{dyn}}{\partial y'} + \frac{\partial}{\partial \sigma}\left(\frac{\nu}{h}\frac{\partial u}{\partial \sigma}\right) + hF_v \tag{7.7}$$

$$\frac{\partial hw}{\partial t} + \frac{\partial huw}{\partial x'} + \frac{\partial hvw}{\partial y'} + \frac{\partial hw\omega}{\partial \sigma} = -\frac{1}{\rho}\frac{\partial p_{dyn}}{\partial \sigma} + \frac{\partial}{\partial \sigma}\left(\frac{\nu}{h}\frac{\partial w}{\partial \sigma}\right) \tag{7.8}$$

where p_{dyn} is the dynamic pressure term, (F_u,F_v) are horizontal diffusion terms and ω is the vertical velocity with respect to the variations in σ given by

$$\omega = \frac{1}{h}\left(w + u\frac{\partial H}{\partial x'} + v\frac{\partial H}{\partial y'} - \sigma\left(\frac{\partial h}{\partial t} + u\frac{\partial h}{\partial x'} + v\frac{\partial h}{\partial y'}\right)\right) \tag{7.9}$$

Compared to the depth-averaged shallow water model, this model adds the vertical discretization of the velocity components, horizontal and vertical diffusion as well as the additional non-hydrostatic pressure distribution.

The above system is solved by a fractional step approach, in which the continuity and momentum equations are first solved without the dynamic pressure. The latter yields an intermediate solution for the velocities, which are then projected onto the space of divergence free solutions by the effect of the dynamic pressure, solved using a Poisson pressure equation. When the final velocities are obtained, the free surface is calculated from the depth-averaged continuity equation (Eq. 3.1), where the depth-averaged velocities are obtained by vertical integration of the velocity profiles.

The eddy viscosity ν_T is estimated by a $k - \varepsilon$ model, which uses the relation

$$\nu_T = c_\mu \frac{k^2}{\varepsilon} \tag{7.10}$$

where $c_\mu = 0.09$ is an empirical constant, k the turbulent kinetic energy (TKE) and ε the dissipation of TKE.

7.2.2 Sediment transport

The sediment transport calculations are generally very similar to the ones presented in the depth-averaged model. The differences presented in the following, relate to the additional available information regarding the vertical variation of the velocities. Some of the sediment transport modeling has been implemented by the author of this thesis and are therefore not included in the original software code.

The model allows (by input selection) the bed shear stress calculation to be performed in one of the following ways:

Bed shear stress from depth-averaged velocity
The three-dimensional velocity field is found from the flow equations and integrated vertically, whereby a depth-averaged velocity is found. From this point it is identical to the depth-averaged model, where the velocity $(\bar{u}, \bar{v})$, is multiplied with a friction coefficient C_D to find the bed shear stress τ_b with Eq. (3.4). This approach will thus not take full advantage of the availability of vertical velocity profiles.

Bed shear stress from bottom cell velocity
The second method is to assume a logarithmic boundary layer in the bottom

cell with height z_b, from which a friction coefficient can be estimated by

$$C_{Db} = \left[\frac{\kappa}{1 + \ln\left(\frac{z_0}{z_b}\right)} \right]^2 \tag{7.11}$$

The bed shear stress can now be calculated from the above and the bottom cell velocity by

$$\frac{\boldsymbol{\tau}_b}{\rho} = C_{Db} \boldsymbol{u}_b |\boldsymbol{u}_b| \tag{7.12}$$

where u_b is the velocity in the bottom cell. The skin friction component of the bed shear stress, can now be calculated using the same skin friction methods that are used in the depth-averaged model. Note that while this is straightforward using Eq. (3.37) (Engelund and Fredsøe (1982)), the iterative method of Einstein (1950) (Eq. 3.26) or the simpler suggestion of Soulsby (1997) (Eq. 3.30), require that the depth-averaged velocity is to be estimated based on the bottom shear stress.

When the skin friction Shields parameters has been obtained, the bed load is then calculated with the Engelund and Fredsøe (1976) equation (Eq. 3.16) and adjusted for slope effects by the empirical method of Olesen (1987) (Eqs. 3.38,3.40). To obtain the suspended sediment concentration profile, the velocity fields and eddy viscosity are inserted in the concentration transport Eq. (3.61). The boundary condition at the bottom, is the reference concentration c_b, calculated by Eq. (3.86) Zyserman and Fredsøe (1994), which is imposed at the distance $2d_{50}$ above the bed.

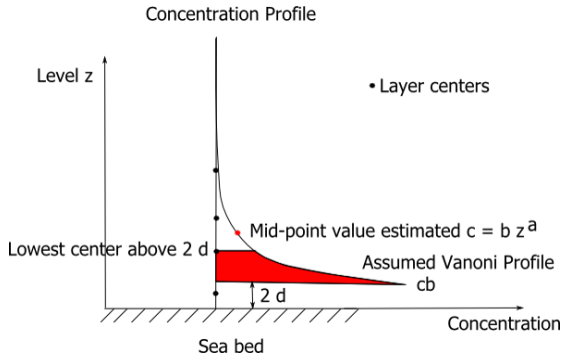

Figure 7.2: Conceptual drawing of the near bed suspended sediment concentration in MIKE 3 Wave FM. Credit: DHI.

Fig. 7.2 illustrates the treatment of the concentration profile at the bottom boundary. As seen, between $2d_{50}$ and the lowest σ-layer center above $2d_{50}$, a

Rouse profile (named Vanoni in the figure) is assumed, due to lack of resolution. When the concentration field c is obtained, the suspended load is found by

$$\boldsymbol{q}_s = \int_{2d_{50}}^{\eta} \boldsymbol{u} c dz \tag{7.13}$$

Finally, the bed level change is calculated (as in the depth-averaged model) by inserting the bed load and suspended load in the Exner equation (Eq. 3.91).

7.3 Validation: Backfilling trench

The backfilling trench experiment DHL (1980) used in the validation of the depth-averaged model in Chapter 4, is used here again to validate the MIKE3 model. The trench is modeled in 2D (x, z) with horizontal grid spacing $\Delta x =$ 0.25 m and 30 σ layers refined towards the bed, with the lowest layer thickness in wall units $\Delta z^+ = \Delta z u_f / \nu$ in the range 150–210. The inlet boundary condition is a constant discharge far upstream and in the outlet a fixed surface elevation is applied. The channel bed has a slope equal to the energy gradient, to ensure equilibrium conditions of the incoming flow. A speed up factor of 100 has been used to amplify the morphological development, and the slope factor on the bed load from Eq (3.38) is set to $\alpha = 30$. It has generally been observed that this factor can be used to stabilize simulations where morphological amplification has been applied.

Fig. 7.3 shows the velocity profiles (in the five locations indicated on Fig. 4.1) before bed morphology is initiated, with the measured data, a log law fit and the simulation results. The log law fit is including all data points through the depth yielding $k_s = 0.0262$ m at profile 1, but if instead, only the lowest five measurements are used, then the roughness height of the incoming velocity is reduced to $k_s = 0.0057$ m. Both configurations have been tested, but only the results with the former are included since they were overall more accurate. Again, application of a global total roughness height rather than grain roughness only, makes some of the profiles suffer from the same problem like the the depth-averaged model near the bed, but it allows the use of larger cells that incorporate the effect of ripples without resolving them.

The skin friction Shields parameter is estimated from Eq. (3.37), where the bed shear stress is calculated by Eq. (7.12). Fig. 7.4 shows the suspended sediment concentration profiles with the measured data, a Rouse profile fit and the simulation results, before bed morphology is initiated. As mentioned in the model description above, the concentration is assumed to follow a Rouse profile between $2d_{50}$ and the center of the σ layer above $2d_{50}$. Using the reported

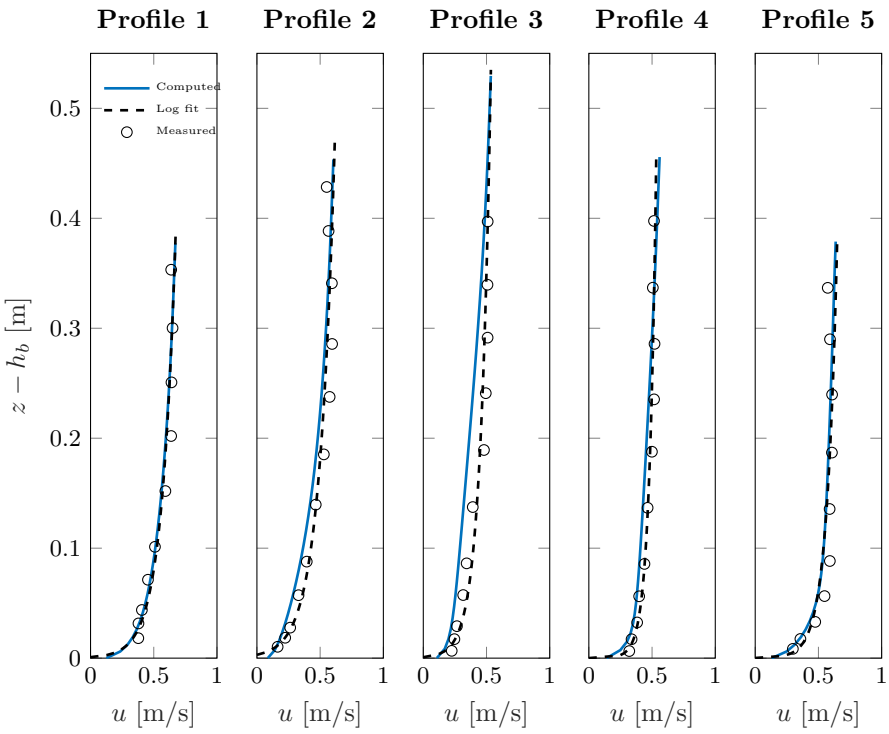

Figure 7.3: Velocity profiles in the five locations.

fall velocity $w_s = 0.013$ m/s rather than calculating, the profiles are predicted exceptionally well in MIKE3 and match the measured data. Profile 3 has a slight deviance between the measured and computed results, which show that the lower near bed part is underestimated, while the mid-upper part is slightly overestimated. Since the concentration is highest near the bed, the suspended load is extremely sensitive to the smallest variations of the various fields and the model inputs. A discrepancy emerges when considering that integration of the measured velocity times concentration in profile 1 with Eq. (7.13), yields an incoming suspended load of $q_s = 0.030$ kg/(s·m) (as originally reported). Here only the interval between the lowest data point 2 cm above the bed and the highest data point at 35 cm are included. On the other hand, integration with the concentration given by a Rouse fit profile starting from $2d_{50}$, yields $q_s = 0.043$ kg/(s·m), which is higher than the reported total seeded value of $q_t = 0.040$ kg/(s·m). The validation here is done by matching the computed profiles to the data in the incoming flow and then observing the results downstream. This yields an incoming suspended load $q_s = 0.047$ kg/(s·m) and bed load $q_b = 0.020$ kg/(s·m). In order to keep the profiles match with the data, the transports

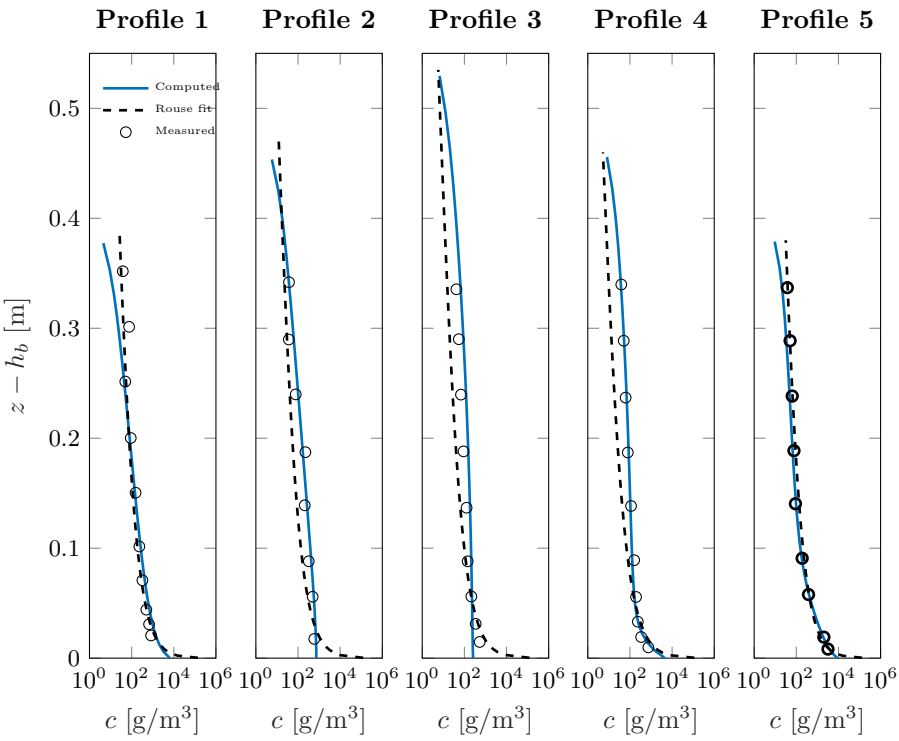

Figure 7.4: Concentration profiles in the five locations.

after integration are reduced artificially by multiplying with a calibration factor, which for the suspended load is 0.75, yielding $q_s = 0.035$ kg/(s·m) and 0.25 for the bed load, yielding $q_b = 0.005$ kg/(s·m).

Fig. 7.5 shows the state of computed fields in the proximity of the trench before the initiation of the bed morphology. The depth-averaged velocity $\bar{u}$ which is denoted HD is calculated by vertical integration of the velocity profile, while the one denoted ST is based on the bottom cell velocity extrapolated using a log law assumption, as described in the previous section. As seen, the velocity differences are mostly prominent above the sloped parts of the trench. This is the primary reason for differences in the results between the depth-averaged Mat2DH model and the MIKE 3 model. The total transport curves (q_t) reveal that both models yield very similar results from the incoming flow side until the beginning of the upslope, where after MIKE 3 shows it's superiority at capturing the large increase in transport. The rate of bed level change $\partial h_b/\partial t$ shown below on the figure, emphasizes this difference above the slopes. The trench backfill is shown in Fig. 7.6 at the timestamps 7.5 and 15 hours, for

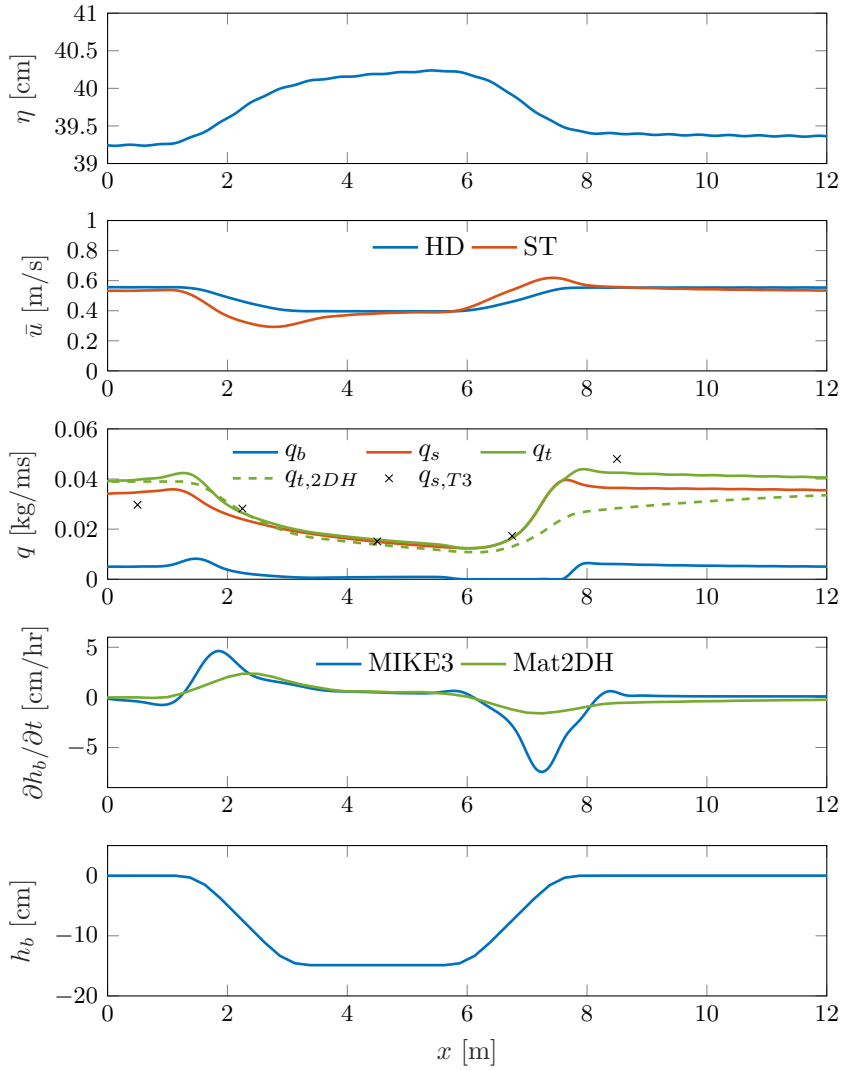

Figure 7.5: Initial state in the simulation before the trench backfilling begins.

which measured data has been provided. After 7.5 hours the MIKE 3 model predicts the trench profile exceptionally well on the downstream side, while it slightly overshoots the backfilling on the upstream side. At the 15 hours mark it can be seen that the whole profile has surpassed the measured data, which means that the backfilling rate is too rapid. The reason for the rapid migration rate can be attributed to some extent to the incorrect evolution of the slope on

the upstream side. The observant reader will notice on Fig. 7.5 a slight increase in the ST velocity just as the bed slopes into the trench, followed by a fast decrease. This phenomena is caused by a combination of streamline divergence as well as adverse pressure gradients. The velocity increase is translated into the sediment transport, which increases the rate of bed level change shown by the pronounced peak just before the $x = 2$ m mark. This peak is infamous to cause unphysical results in numerical simulations and is in some cases reduced by filtering, which has been applied here as well. As the bed starts morphing an equilibrium slope is established whereby pure migration occurs in the upstream side. The steepness of this slope affects the migration rate, hence, when the slope is steeper the migration rate is increased. The depth-averaged model, which does not capture the detailed flow pattern, is therefore predicting the downslope better as it smooths out the rate of bed level change.

Another contributer to the mismatch can be due to inaccurate data in the original report. Other simulations with a lower transport rate have shown better matches at the 15 hours time stamp as well as the upstream side prediction. One reason to suspect some flaws in the data is that the bed load has to be reduced with as much as a factor 0.25 in the incoming flow side, which is supposed to be in equilibrium. On a plane bed with steady flow, the formula is expected to perform better, and only a reduction of the incoming velocity can attain that. However, this would underestimate the velocity profiles compared to the measurements. Furthermore, the drop in measured suspended load between profiles 1 and 2 is extremely low as seen by the $\times$ mark on Fig. 7.5. This means that practically all the suspended sediments remain in suspension while being transported horizontally over 1.5 m and a drop of 7.5 cm. To conclude though, it can be seen that the MIKE 3 model performs well at predicting the concentration profiles and the overall physical mechanism.

7.4 Sandwave simulations

In this section the model is used to simulate sandwaves. Rather than a detailed study, the simulations here are intended to test the model for this kind of application and compare to similar work done in the past as e.g. by Niemann (2003).

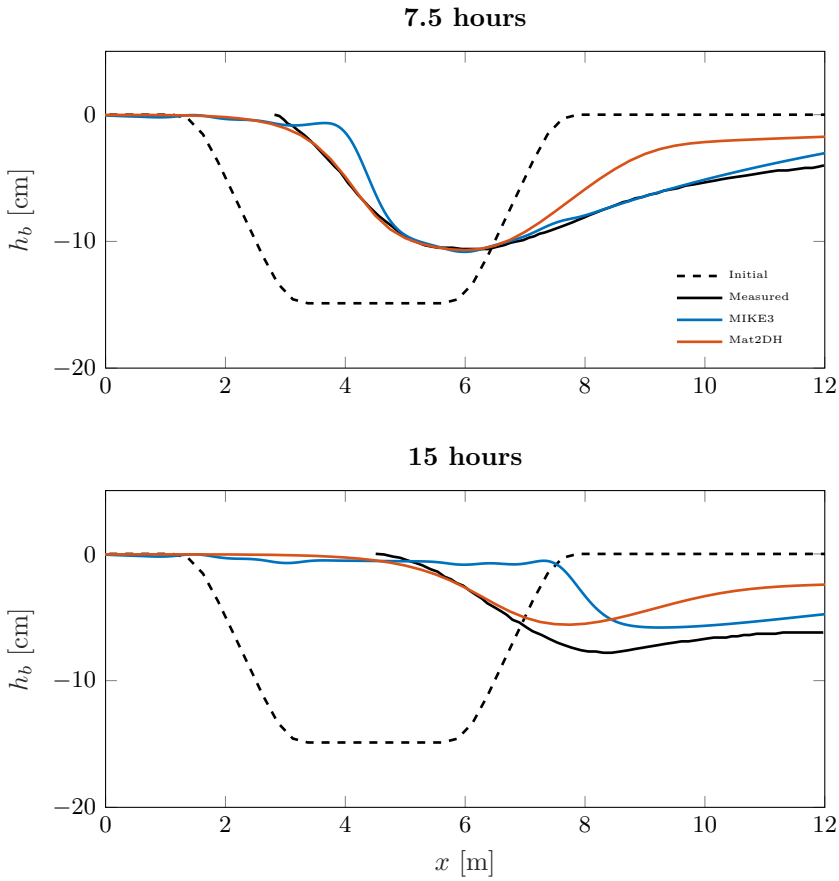

Figure 7.6: State of the trench after 7.5 hours and 15 hours.

7.4.1 Linear stability analysis

A linear stability analysis is conducted as a preparation for a morphological simulation of sandwaves. The methodology is identical to the stability analysis in Chapter 5, where the perturbation here is applied with $k_y = 0$ in Eq. (5.1), i.e. assuming uniformity in the lateral direction. The simulation parameters are a depth of $h_0 = 12$ m, mean flow velocity $U_0 = 1$ m/s, mean grain diameter $d_{50} = 0.26$ mm and bed roughness coefficient $C_{D0} = 0.0025$. The domain is 2D vertical with periodic boundaries and the flow is driven by a body force. 40 σ-layers refined towards the bottom are used to resolve vertically and different number of simulations with increasing N in the range 10–160 grid points per wavelength are tested.

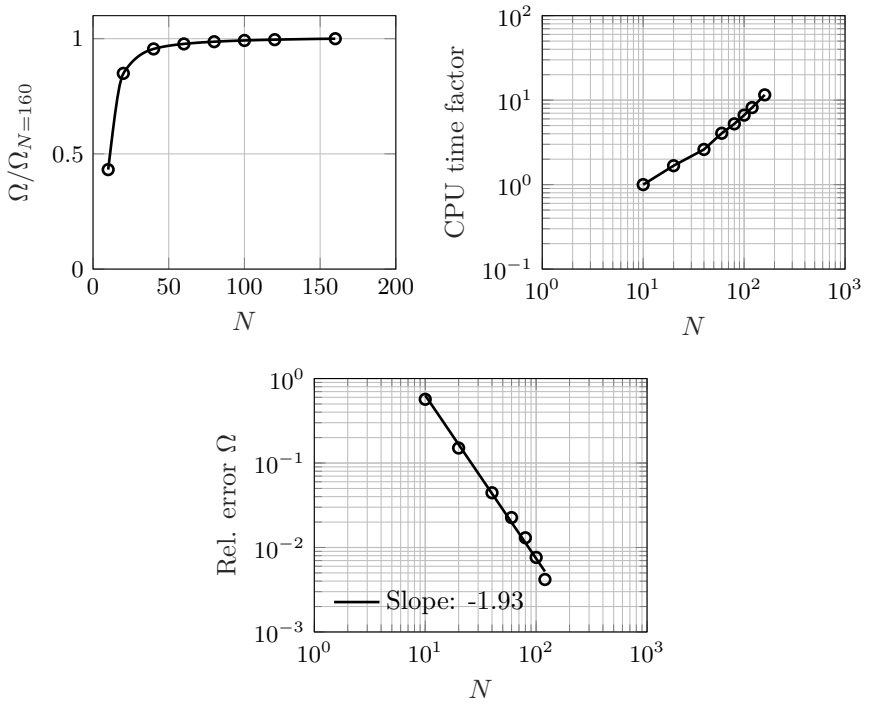

Figure 7.7: Convergence of the growth rate Ω vs. N, for a perturbation with $A/h_0 = 0.01$ and $k_x h_0 = 0.05$. N is the number of grid points per bed wavelength and the error is calculated relative to the growth rate with $N = 160$.

Fig. 7.7 show the results of a convergence study of the growth rate Ω vs. the number of grid points per bed wavelength N. As seen, the convergence rate is roughly a factor two, which is what would be expected for the second order discretization scheme in space. The accuracy of the solution would be satisfactory with as little as 40 grid points per wavelength, but this might not be enough at nonlinear stages and it is therefore chosen to use twice that number in the following morphological simulation, i.e. $N = 80$. This lays within the range 60–160, which Niemann (2003) found necessary to simulate dune morphology with a satisfactory accuracy.

Fig. 7.8 show the stability curves of Ω vs $k_x h_0$, when the bed shear stress is calculated from 1) the bottom layer velocity u_b and from 2) the depth-averaged velocity $\bar{u}$. As seen, there are no bedforms growing with the latter method, i.e. the bed remains stable. This is because the depth-averaged velocity represents a smeared out value of the velocities through the whole water column. Hence, for a

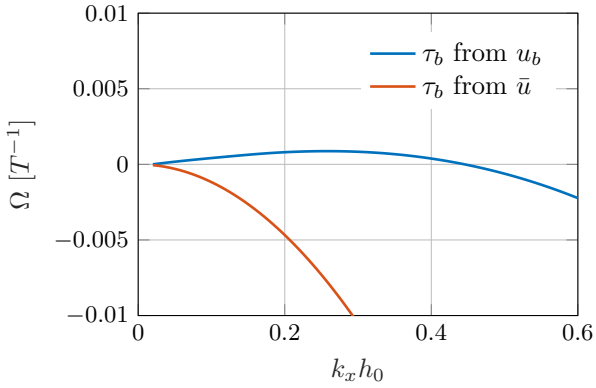

Figure 7.8: Stability curves.

subcritical flow (which is the case), the depth-averaged velocity will be in phase with the bed, and thus also the bed load before consideration of other effects. However, once the gravity effects of transport over slopes (recall, calculated from the gradient of the bed) as well as the suspended load are considered, the sediment transport will have a negative phase compared to the bed, and hence no growth occurs. On the other hand, when only the velocity of the bottom cell is used, adverse pressure gradient effects become more pronounced and hence despite the decaying effects of the gravity and suspended load, the bed shear stress will attain a positive phase difference at a certain range of wavenumbers. As seen from Fig. 7.8, the bedforms with wavenumbers in the range $k_x h_0 =$ 0.02–0.45 are all unstable. The fastest growing bedform in the peak of the range at $k_x h_0 = 0.26$, corresponds to a sandwave with a wavelength of approximately 300 m.

7.4.2 Morphological development

Similar to the previous morphological simulations of the sandbanks, the fastest growing sandwave wavelength that emerged in the linear stability analysis, is used as a guidance for the following morphological runs. The flow parameters are identical to the ones presented previously. The horizontal length of the domain is set to the length of three of the above-mentioned sandwaves. One limitation of the model is that the Poisson solver does not have periodic boundaries implemented, so when the sandwave becomes high enough for the dynamic pressure to be of higher significance, an "artificial" increase of the sandwave occurs once it reaches the outflow boundary. Therefore the presented results only consider the development up till that point, and the subsequent unphysical development

is omitted. In these simulations the spatial filter mentioned in the trench validation is deactivated, in order to allow uninterrupted bedforms development. This shows as sharp peaks on some of the sandwave crests, but has generally not interfered.

Three configurations of initial bed condition are simulated: The first is given a sinusoidal perturbation equal to the peak growth wavenumber $k_x h_0 = 0.26$ and amplitude $A/h_0 = 0.01$, as in the linear stability analysis. The second simulation is initiated with a completely plane bed, and the third simulation is plane like the latter, but is also resolved in the lateral direction with 10 grid points, i.e. being a 3D simulation. The development of the maximum amplitude over time for each case is shown in Figs. 7.9–7.11, and an illustrative progression of the whole bed is shown in Figs. 7.12–7.14. It can be seen that for the initial plane bed cases an instability causes the bed to grow without introduction of any perturbation. This is due to a build up of numerical residuals in the dynamic pressure, which affect the other fields. As the rate of bed level change is amplified by a factor 10,000, at some point an instability "kicks in" the emergence of ripple-like bedforms that grow and merge. These also appear in the perturbed simulation, but generally as superimposed bedforms on the three sandwaves, which appear to remain throughout the simulation. In the plane bed case there is a gradual process of bedforms merging and only towards the end of the presented simulation it is reduced to three sandwaves in the domain. Interestingly they vary in length and amplitude, as sandwaves do in real bathymetry scans. The 2D and 3D flat bed simulations show a very similar bedform development, with difference being mostly in the progression of the max amplitude, which is less oscillatory in the 3D case. Note that the latter was simulated for half the time of the other two cases. The 3D case yielded sandwaves that were almost perfectly uniform in the lateral direction, but more investigation is necessary as the low lateral resolution as well as the quadrilateral mesh elements used in this case might affect the results. Regarding the height development, the perturbed case starts growing immediately, while the unperturbed need more time to build up the instability, but these are only numerical issues. For all cases there is a rapid growth initially which decays in a similar manner to the sandbank development simulations in the previous chapter. The mean amplitude growth here is proportional to $\ln(t)$ and seem to stabilize towards a height of 4 m, which is exactly a third of the mean depth and in line with the the reviewed literature.

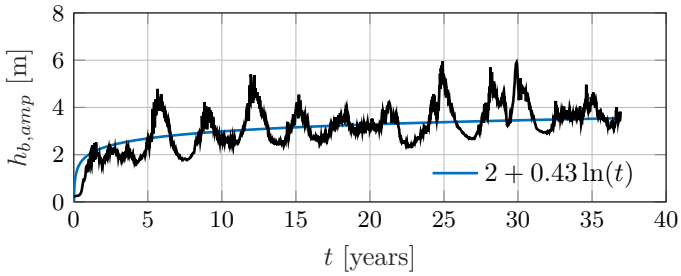

Figure 7.9: Bedform height development for 2D perturbed case.

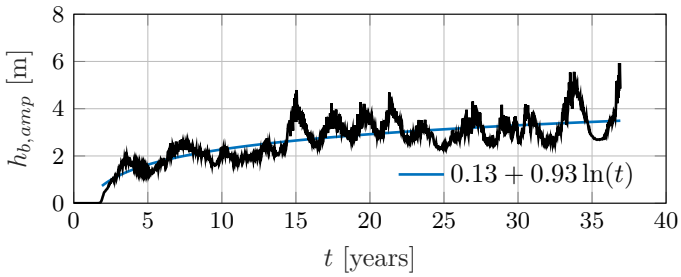

Figure 7.10: Bedform height development for 2D plane bed case.

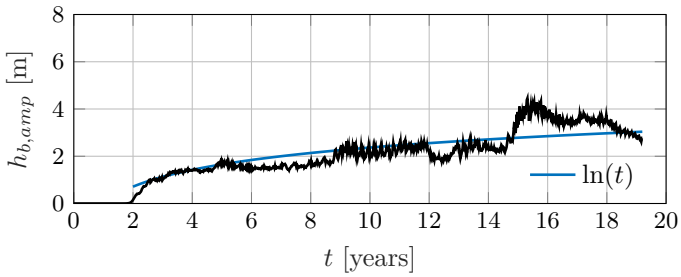

Figure 7.11: Bedform height development for 3D plane bed case.

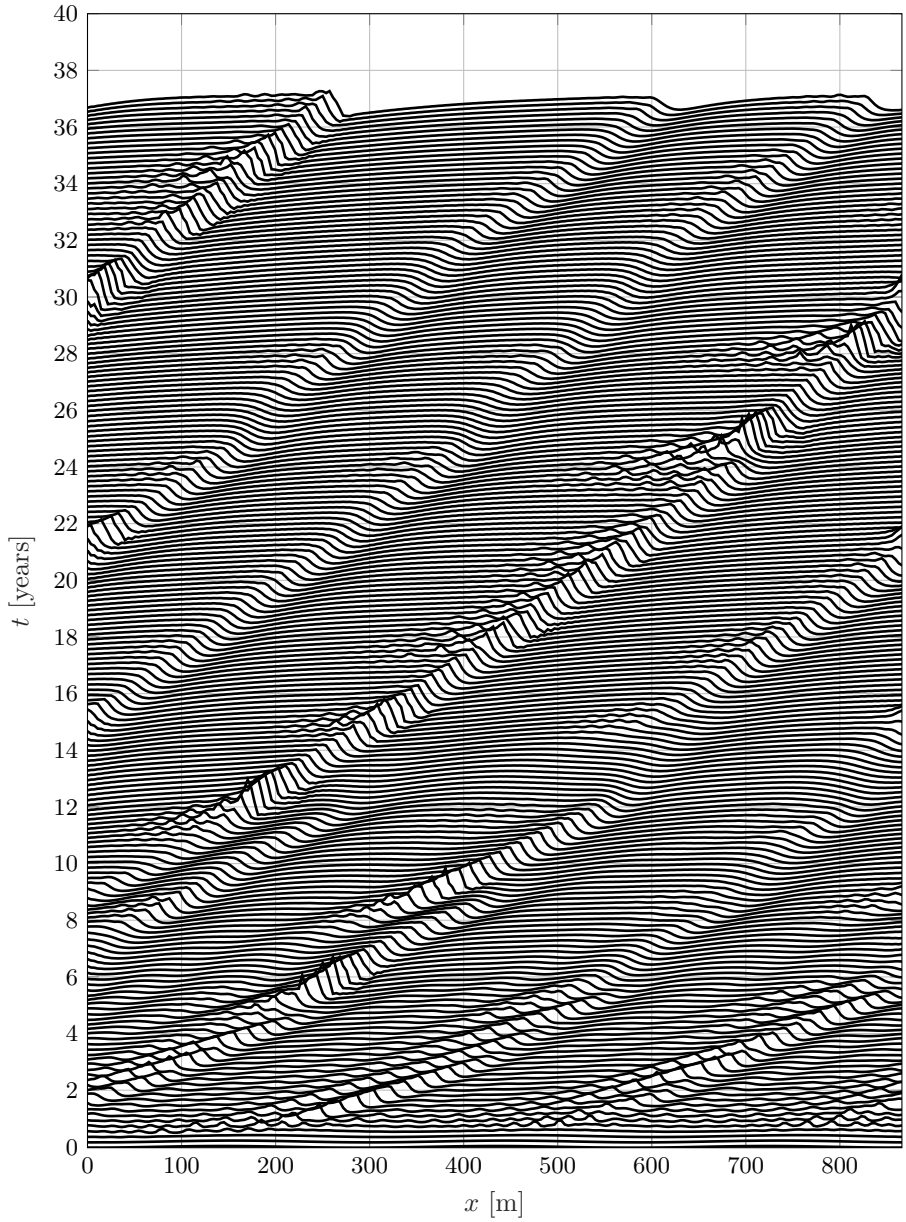

Figure 7.12: Sandwaves development in 2D from sinusoidal perturbation.

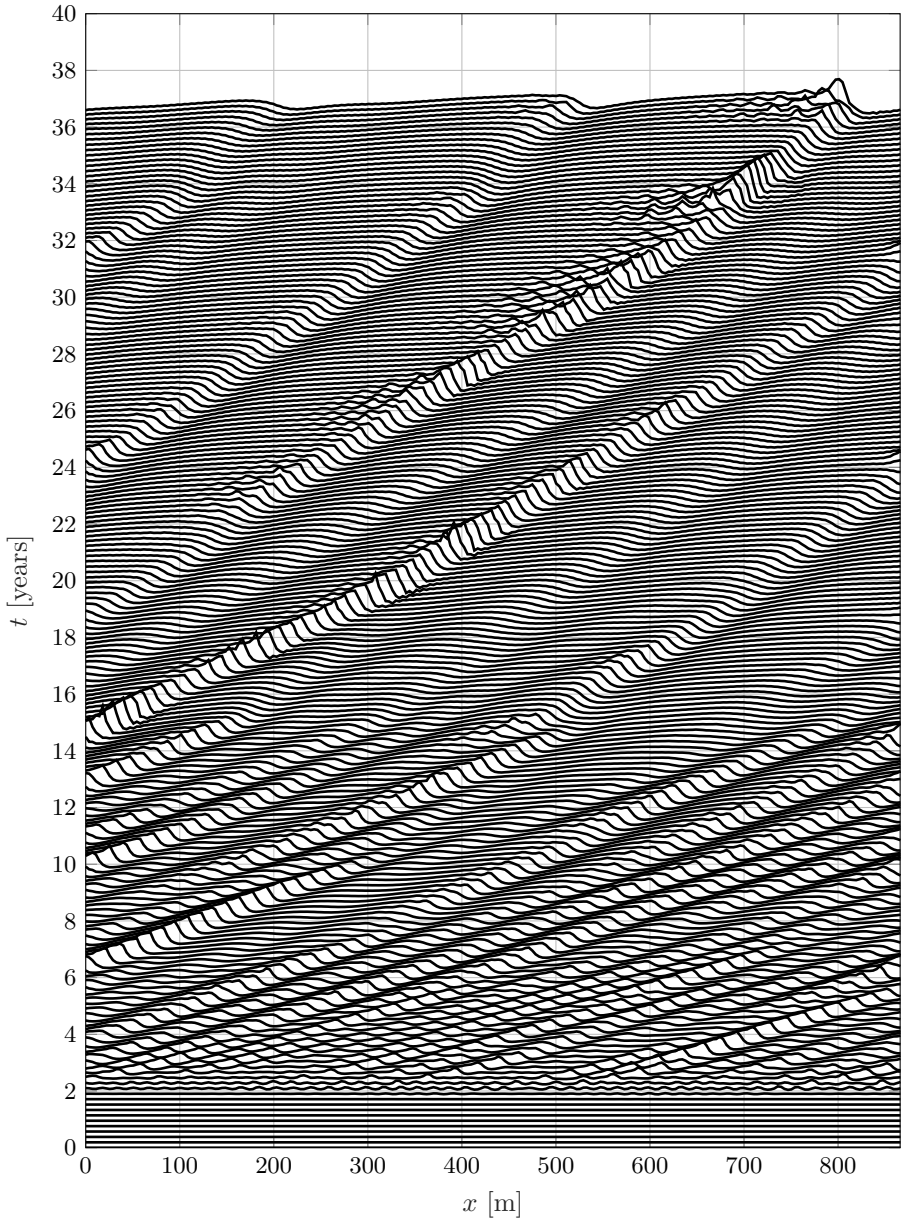

Figure 7.13: Sandwaves development in 2D from plane bed.

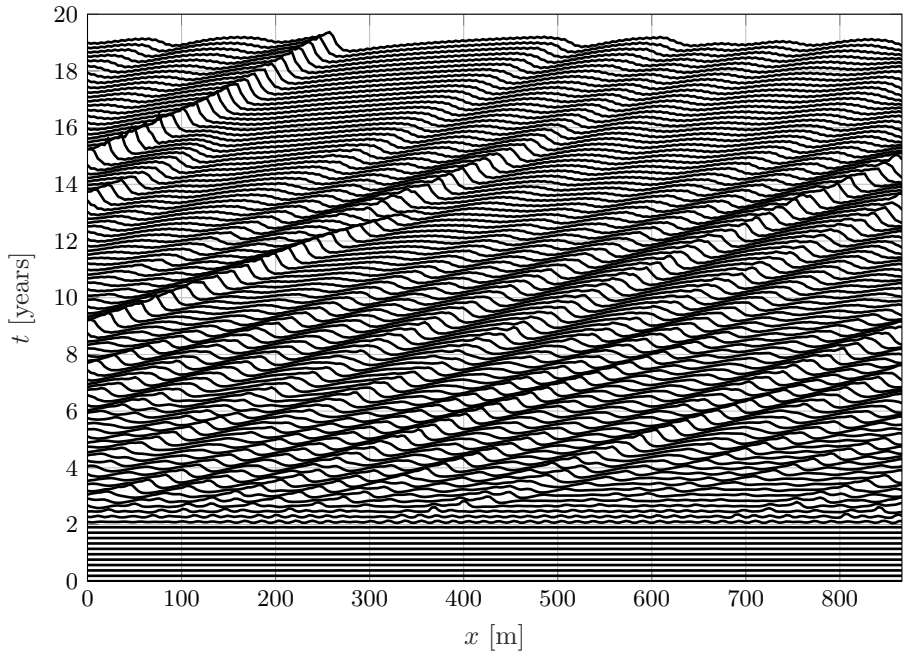

Figure 7.14: Sandwaves development in 3D from plane bed.

7.5 Sandwave - monopile interaction

In this last section, several full scale simulations of sandwave-monopile interaction are explored, with a detailed modeling of the monopile, rather than implementing it as additional roughness, like in the previous chapter. Such simulation would traditionally be conducted in detailed CFD models with downscaled domains. In this section, very basic and preliminary tests have been conducted in MIKE 3, from which results show great potential for further studies. The mean depth in all cases is $h_0 = 12$ m, the incoming flow velocity $U_0 = 1$ m/s and the bed roughness $C_{D0} = 0.0025$. Fig. 7.15 shows the probed lateral velocity v on the lee-side (where shed vortices pass through) of a cylinder with diameter $D_M = 6$ m. Below in the figure, the energy spectrum of the velocity is shown with peak frequency 0.035 Hz, which yields a Strouhal number $St = 0.21$, in line with the theory, Sumer and Fredsøe (1997).

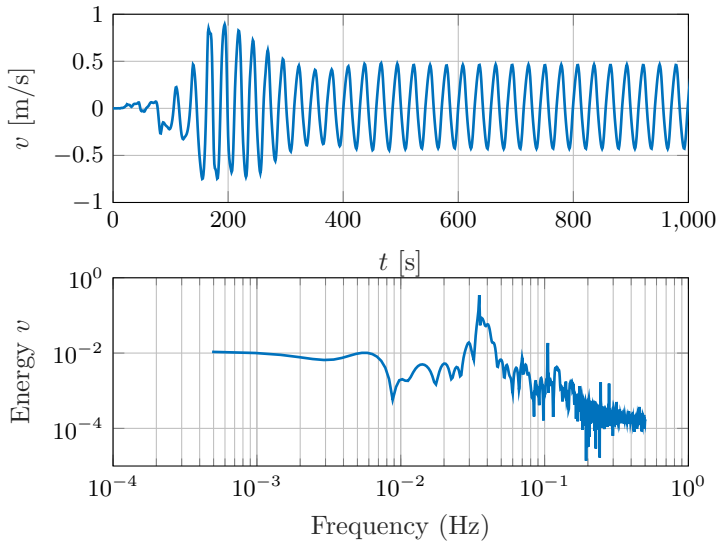

Figure 7.15: Lateral velocity v on the lee side of the monopile and energy spectrum.

The next case tested the progression of a scour hole around the monopile in the above-mentioned flow conditions. In this case the dynamic pressure was set to zero, since it was not possible to obtain a stable morphological simulation. Fig. 7.16 shows the period averaged bed shear stress amplification, relative to the free stream value. The maximum amplification occurs on the monopile sides and reaches a value slightly higher that six. The negative amplification

in the upstream side is due to the boundary layer separation zone where the horseshoe vortex is formed. From the center of the monopile, the extent of this zone is approximately $1.2D_M$ and the boundary layer height-to-pile diameter ratio is approximately 2. On Fig. 7.17 the scour progress is monitored on the upstream and downstream edges of the monopile. The downstream side suffers from the lack of dynamic pressure in the simulation, but both seem to be converging towards 1.3 and 0.6 upstream and downstream, respectively. A proper monopile scour validation is required, but overall it can be seen that these results are comparable to the data presented by Roulund et al. (2005). Fig. 7.18 illustrates the development of the scour hole, where it can be seen that the extracted sand forms a bedform that is being transported downstream. With this model the further development of that bedform could potentially be studied.

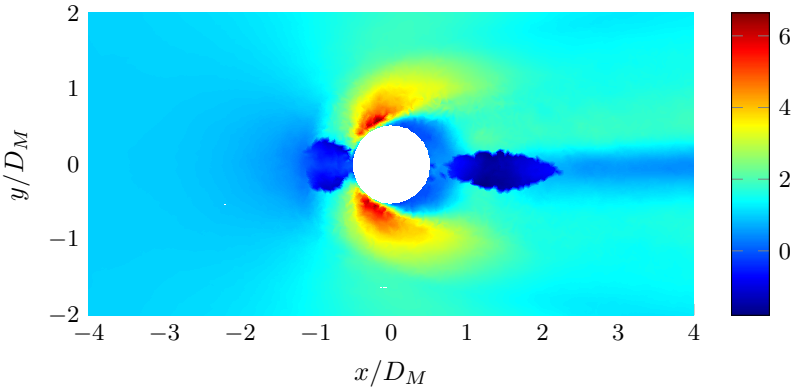

Figure 7.16: Bed shear stress amplification.

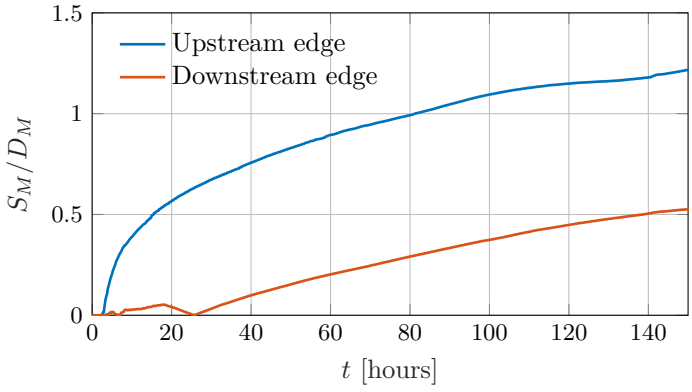

Figure 7.17: Scour hole development where S_M represent the scour depth.

The last simulation is shown in Fig. 7.19, which shows a full scale sandwave field migrating past a monopile, where a symbolic scour protection has been implemented by limiting the thickness of the bed surrounding the monopile. This demonstrates the models ability, here including the dynamic pressure, to combine the very different timescales of monopile scour and sandwave migration. From this figure it appears that the sandwave is mostly affected on the lee-side of the monopile by limiting the migration speed and blocking the sediment transport. A build up of sand can also be seen on the upstream side of the monopile. A detailed study could investigate the effect of a series of monopiles on sandwaves. This could answer some of the questions raised in this chapters introduction, about the monopiles slowing sandwaves down, breaking them up and changing orientation, or rather not affecting significantly. It could also be investigated whether a monopile field could initiate the growth of a bedform field that turns into sandwaves.

7.6 Closing remarks

While this chapter by no means show a finished work, it probes some of the possible options for extension of the study in this thesis. All of the results presented in this chapter were obtained over relatively short computation times on a quad cored desktop PC. The ability of the model to incorporate accurate calculations of suspended load and bed morphology, while maintaining some of the aspects that make it run faster than traditional CFD models, give hope that it can be used for some of the computations that are otherwise done in 2DH or 2DV.

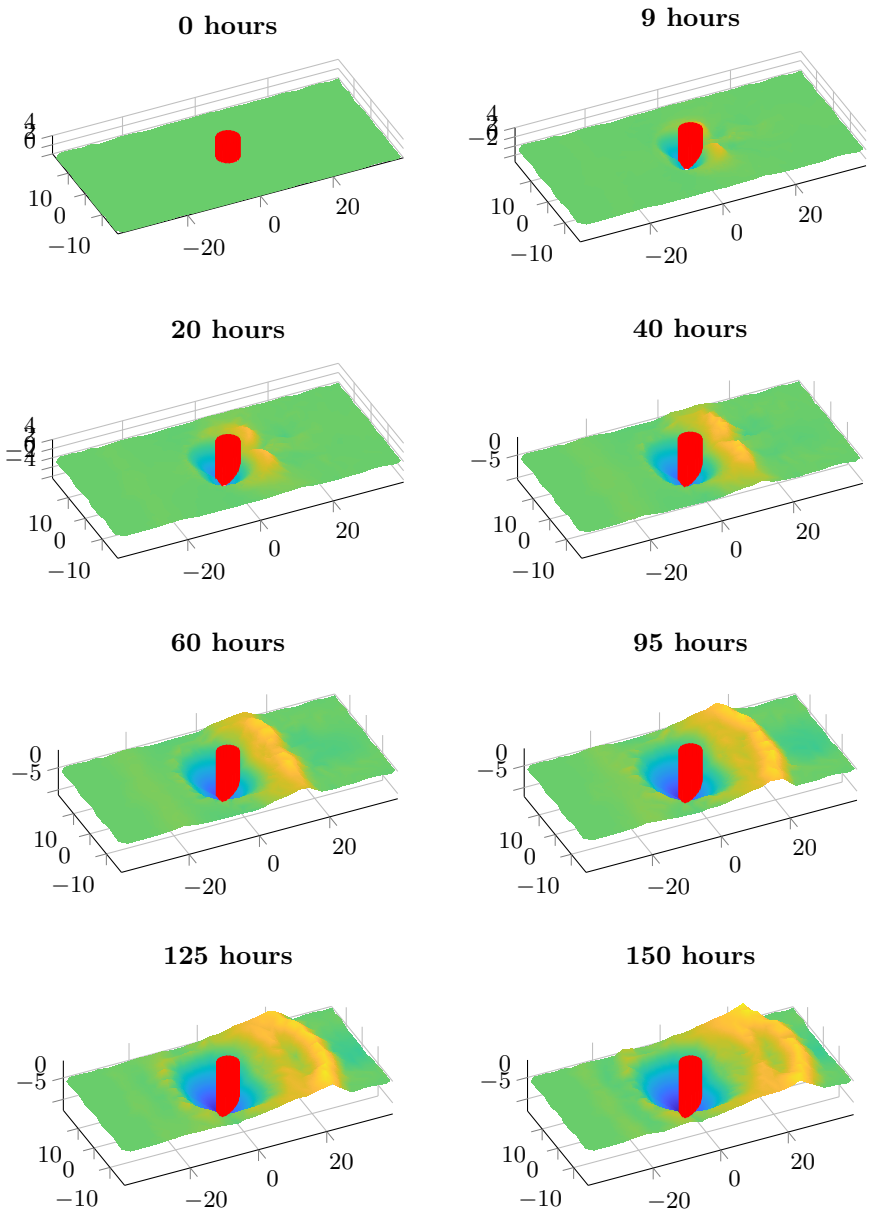

Figure 7.18: Scour hole development. Axes units in meters.

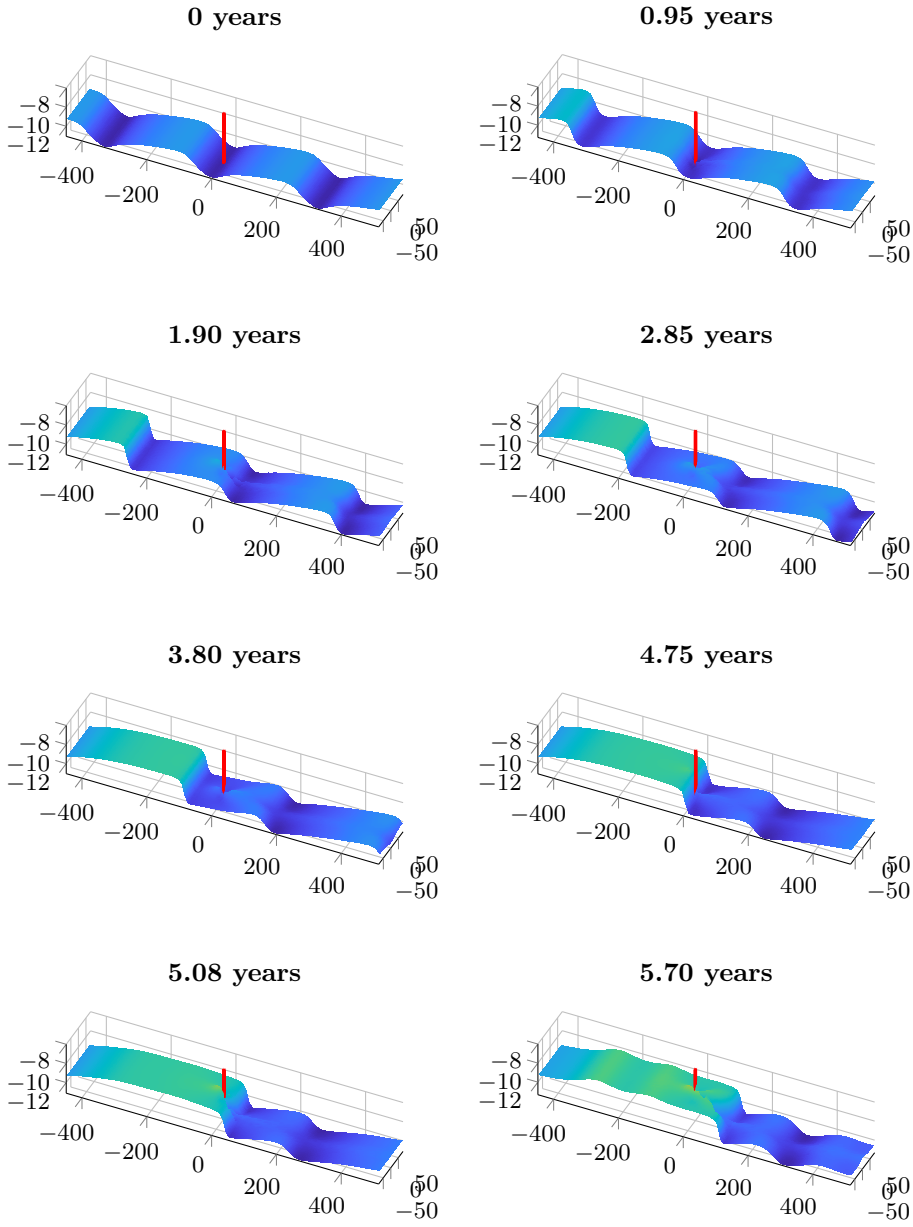

Figure 7.19: Sandwave migrating past a monopile. Axes units in meters.

Chapter 8

Conclusions

In this thesis a study on large-scale bedforms in the sea was conducted. The bedforms were modeled in a depth-averaged shallow water model (2DH) that was developed in Matlab. The model calculates horizontal gradients spectrally and includes sediment transport calculations featuring bed load, suspended load with lag effects and bed morphology. A validation was successfully conducted with measurements from a backfilling trench as well as a flume with alternate sandbar patterns. The model was then used to conduct a parametric numerical linear stability analysis of bedforms, for which more than 10,000 simulations were run on a HPC cluster. The stability analysis yielded results that were in line with the covered literature on the subject, showing the emergence of bedforms with characteristics of sandbanks which have wavelengths in the order of kilometers and century long migration periods. However, the suspended load contribution appears to have been downplayed in earlier findings. In previous research focus was on the instability mechanisms and the parameters were non-dimensionalized in a manner that made it more difficult to compare the results. These led the primary attention to bed load and many disregarded suspended load in their models. The findings here suggest that the magnitude of the suspended load and its phase difference from the bed shear stress, play and important role on the outcome of the sandbanks and should therefore be accounted for.

The results of the linear stability analysis were carried over to a morphological study on the bedforms in the same Matlab model. This study showed that the

finite bedforms in the periodic model are affected by the domain size. Thus, the useful findings of the stability analysis were in identifying the wavenumber space in which bedforms grow and estimating their initial growth rate. It was also shown that a tide-plus-current flow yields the same final bedform, as long as the tidal period-averaged flow was not zero. Wind farms were then added to the domain to study the interaction with the bedforms. These were implemented by estimating the drag from each monopile on the subgrid level. The wind farms were introduced on existing bedforms in one case, and on a flat bed in the second case. The results showed that the effects from the monopiles had a correlation with the spacing between monopiles. For realistic spacing values, the effect on the large-scale bedforms were limited, when considering that the bedform morphological changes occur over centuries, while wind farms are designed for a 25 year lifespan. Hence, there is reason to believe that at intermediate water depths of around 30 m, wind farms have practically no effect on the grand scale of the bed, and might in fact stabilize sandbanks.

Lastly, a three-dimensional model (Mike 3 Wave FM by DHI) with free surface was used to explore the possibility of simulating more active bedforms such as sandwaves, and their interactions with monopiles. The 3D model is an extension of the MIKE 3 FM model, to which dynamic pressure terms have been added and the momentum equations are solved in three dimensions. The model was successfully validated with the backfilling trench experiment previously used for the depth-averaged model. In this regard, excellent matches were found with measured suspended sediment concentration profile. Morphological simulations of bedforms yielded results similar to the characteristics of sandwaves in time- and length scales, i.e. years and hundreds of meters. The model was also tested with flow around a cylinder. Due to time restrictions the results are very preliminary, but vortex shedding on the lee side and a horseshoe vortex emerged around the cylinder as well as the development of a scour hole of comparable dimensions to similar scientific literature. This is traditionally conducted with detailed CFD models with downscaled domains, but was here achieved in full scale at computational times of hours to days. Lastly, a simulation of sandwaves migrating past a monopile was conducted in full scale. Here more study is necessary to conclude, but there were clear effects on the sandwave in the monopiles lee side.

8.1 Recommendations for further work

The results in this thesis were all outcomes of numerical simulations by models validated on laboratory scaled experiments. So in order to draw firmer conclusions, it would be necessary to compare the results with real bathymetric

data. Furthermore, a test of the depth-averaged model results with the three-dimensional model could greatly help providing confidence in whether the 2DH approach is sufficient, in light of the importance of correct suspended load modeling. However, the most promising direction for further study is laid out in Chapter 7. Sandwaves are of serious concern for engineering projects in the offshore environment. This concern can be addressed in the three-dimensional model, which have demonstrated its potential to combine different length- and timescales.

Bibliography

Storm Surge Barrier Oosterschelde: Computation of Siltation in Dredged Trenches. Technical report, Delft Hydraulics Laboratory, 1980.

Renewable energy - Moving towards a low carbon economy, 2017. URL `https://ec.europa.eu/energy/en/topics/renewable-energy`.

G. Besio, P. Blondeaux, and P. Frisina. A note on tidally generated sand waves. *Journal of Fluid Mechanics*, 485(2003):171–190, 2003. ISSN 00221120. doi: 10.1017/S0022112003004415.

G. Besio, P. Blondeaux, and G. Vittori. On the formation of sand waves and sand banks. *Journal of Fluid Mechanics*, 557:1, 2006. ISSN 0022-1120. doi: 10.1017/S0022112006009256.

G. Besio, P. Blondeaux, M. Brocchini, S. J M H Hulscher, D. Idier, M. a F Knaapen, a. a. Németh, P. C. Roos, and G. Vittori. The morphodynamics of tidal sand waves: A model overview. *Coastal Engineering*, 55(7-8):657–670, 2008. ISSN 03783839. doi: 10.1016/j.coastaleng.2007.11.004.

P. Blondeaux and G. Vittori. Flow and sediment transport induced by tide propagation: 1. The flat bottom case. *Journal of Geophysical Research C: Oceans*, 110(7):1–13, 2005a. ISSN 01480227. doi: 10.1029/2004JC002532.

P. Blondeaux and G. Vittori. Flow and sediment transport induced by tide propagation: 2. The wavy bottom case. *Journal of Geophysical Research C: Oceans*, 110(8):1–11, 2005b. ISSN 01480227. doi: 10.1029/2004JC002545.

Paolo Blondeaux and Giovanna Vittori. The formation of tidal sand waves: Fully three-dimensional versus shallow water approaches. *Continental Shelf Research*, 31(9):990–996, 2011. ISSN 02784343. doi: 10.1016/j.csr.2011.03.005.

B. W. Borsje, P. C. Roos, W. M. Kranenburg, and S. J M H Hulscher. Modeling tidal sand wave formation in a numerical shallow water model: The role of turbulence formulation. *Continental Shelf Research*, 60:17–27, 2013. ISSN 02784343. doi: 10.1016/j.csr.2013.04.023.

B. W. Borsje, W. M. Kranenburg, P. C. Roos, J. Matthieu, and S. J M H Hulscher. The role of suspended load transport in the occurrence of tidal sand waves. *Journal of Geophysical Research: Earth Surface*, 119(4):701–716, 2014. ISSN 21699011. doi: 10.1002/2013JF002828.

John P Boyd. Chebyshev and Fourier Spectral Methods. *New York*, page 688, 2000. ISSN 0486411834. doi: 10.1007/978-0-387-77674-3.

Noel Carbajal, Stephanie Piney, and Jorge Gómez Rivera. A numerical study on the influence of geometry on the formation of sandbanks. *Ocean Dynamics*, 55(5-6):559–568, 2005. ISSN 16167341. doi: 10.1007/s10236-005-0034-1.

H E de Swart and S J M H Hulscher. Dynamics of large-scale bedforms in coastal seas. In *Nonlinear Dynamics and Pattern Formation in the Natural Environment*, pages 315–331, 1995.

H J de Vriend. Steady flow in shallow channel bends. *Comm. on Hydr. Engrg, Dept. of Civil Engrg, Delft University of Technology, Report*, 81-3, 1981.

H. J. de Vriend. 2DH mathematical modelling of morphological evolutions in shallow water. *Coastal Engineering*, 11(1):1–27, 1987. ISSN 03783839. doi: 10.1016/0378-3839(87)90037-8.

H J de Vriend. Morphological processes in shallow tidal seas. *Residual Currents and Long-Term Transport, Coastal Estuarine Studies*, 38(June):276–301, 1990. doi: 10.1029/CE038p0276.

Huib J. de Vriend. 2DH computation of transient sea bed evolutions. In *20th Coastal Engineering Conference*, pages 1698–1712, 1986.

Der Spiegel. Offshore Wind Installations. URL `http://cdn2.spiegel.de/images/image-82451-galleryV9-mspj.jpg`.

DHI. MIKE 21 & MIKE 3 Flow Model FM - Hydrodynamic and Transport Module - Scientific Documentation, 2013a.

DHI. MIKE 21 & MIKE 3 Flow Model FM - Sand Transport Module - Scientific Documentation, 2013b.

Hans Albert Einstein. The Bed-Load Function for Sediment Transportation in Open Channel Flows. *Soil Conservation Service*, (1026):1–31, 1950.

Energinet.dk. The Danish Windcase, 2016. URL `http://www.energinet.dk/EN/KLIMA-OG-MILJOE/the-Danish-windcase/Sider/Den-danske-vindcase.aspx`.

F. Engelund. Flow and bed topography in channel bends. *Jounal of the Hydraulics Division*, 100(11):1631–1647, 1974. ISSN 0044-796X.

F Engelund and J Fredsøe. Sediment Ripples and Dunes. *Annual Review of Fluid Mechanics*, 14:13–37, 1982. ISSN 0066-4189. doi: 10.1146/annurev.fl.14.010182.000305.

Frank Engelund. Instability of erodible beds. *Journal of Fluid Mechanics*, 42 (02):225, 1970. ISSN 0022-1120. doi: 10.1017/S0022112070001210.

Frank Engelund and Jørgen Fredsøe. A Sediment Transport Model for Straight Alluvial Channels. *Nordic Hydrology*, 7(5):293–306, 1976. doi: 10.2166/nh.1976.019.

Frank Engelund and Eggert Hansen. A monograph on sediment transport in alluvial streams. *Teknisk Forlag*, page 65, 1967. ISSN 0717-6163. doi: 10.1007/s13398-014-0173-7.2.

EWEA. The European offshore wind industry key 2015 trends and statistics. ... *Documents/Publications/Reports/Statistics/ ...*, (January):31, 2015. ISSN 00051098. doi: 10.1109/CCA.1997.627749.

Luca Fianchisti. *The Stability of Large-Scale Bed Forms in the Sea*. Msc thesis, Technical University of Denmark (DTU), 2015.

Jørgen Fredsøe. On the development of dunes in erodible channels. *Journal of Fluid Mechanics*, 64(1974):1, 1974. ISSN 0022-1120. doi: 10.1017/S0022112074001960.

Jørgen Fredsøe. Meandering and braiding of rivers. *Journal of Fluid Mechanics*, 84(04):609, 1978. ISSN 0022-1120. doi: 10.1017/S0022112078000373.

Jørgen Fredsøe and Rolf Deigaard. *Mechanics of coastal sediment transport*, volume 3 of *Advanced Series on Ocean Engineering*. World Scientifc, 1992. ISBN 9810208405.

Y. Fujita and Y. Muramoto. Studies on the Process of Development of Alternate Bars. *Bulletin of the Disaster Prevention Research Institute*, 1985. ISSN 0454-7675.

R. Galappatti. A depth integrated model for suspended transport. Technical report, Department of Civil Engineering, Delft University of Technology., 1983.

Theo Gerkema. A linear stability analysis of tidally generated sand waves. *Journal of Fluid Mechanics*, 417:303–322, 2000. ISSN 00221120. doi: 10.1017/S0022112000001105.

William D. Grant and Ole Secher Madsen. Movable bed roughness in unsteady oscillatory flow. *Journal of Geophysical Research*, 1982. ISSN 0148-0227. doi: 10.1029/JC087iC01p00469.

Andreas Myrhøj Stengel Hansen. *The Influence of Offshore Windmill Foundations on the Stability of Large Scale Bedforms*. Msc thesis, Technical University of Denmark (DTU), 2015.

Suzanne J. M. H. Hulscher. Tidal-induced large-scale regular bed form patterns in a three-dimensional shallow water model. *Journal of Geophysical Research*, 101(C9):20727, 1996. ISSN 0148-0227. doi: 10.1029/96JC01662.

Suzanne J. M. H. Hulscher and G. Matthijs van den Brink. Comparison between predicted and observed sand waves and sand banks in the North Sea. *Journal of Geophysical Research*, 106(C5):9327, 2001. ISSN 0148-0227. doi: 10.1029/2001JC900003.

Suzanne J M H Hulscher, Huib E. de Swart, and Huib J. de Vriend. The generation of offshore tidal sand banks and sand waves. *Continental Shelf Research*, 13(11):1183–1204, 1993. ISSN 02784343. doi: 10.1016/0278-4343(93)90048-3.

John M. Huthnance. On one mechanism forming linear sand banks. *Estuarine, Coastal and Shelf Science*, 14(1):79–99, 1982. ISSN 02727714. doi: 10.1016/S0302-3524(82)80068-6.

Natalia L Komarova and Suzanne J M H Hulscher. Linear instability mechanisms for sand wave formation. *Journal of Fluid Mechanics*, 413:219–246, 2000. ISSN 00221120. doi: 10.1017/S0022112000008429.

Agnes Kovacs and Gary Parker. A new vectorial bedload formulation and its application to the time evolution of straight river channels. *J. Fluid Mech*, 261:153–183, 1994. ISSN 0022-1120. doi: 10.1017/S002211209400114X.

R.˜F. Luque. *Erosion and transport of bed-load sediment*. PhD thesis, Technische Hogeschool, Delft (Netherlands)., 1974.

Erik Østergaard Madsen. *Numerical simulation of the dynamics of large-scale bedforms*. Phd thesis, Technical University of Denmark (DTU), 2001.

Jonatan Margalit and David R. Fuhrman. DEVELOPMENT OF LARGE SCALE BED FORMS IN THE SEA 2DH NUMERICAL MODELING. In *Coastal Dynamics*, pages 1120–1130, 2017.

Jonatan Margalit, David R. Fuhrman, and Jacob H. Jensen. The morphing of sand banks: a numerical linear stability analysis. *In review in Coastal Engineering*, 2018.

Fenneke Van Der Meer, Suzanne J M H Hulscher, and Joris Van Den Berg. On the influence of suspended sediment transport on the generation of offshore sand. *Particle laden flows*, pages 29–41, 2007.

NASA. Thanet wind farms from space, 2015. URL `https://eoimages.gsfc.nasa.gov/images/imagerecords/89000/89063/thanet{_}oli{_}2015181.jpg`.

Jonathan M. Nelson. The initial instability and finite-amplitude stability of alternate bars in straight channels. *Earth Science Reviews*, 29(1-4):97–115, 1990. ISSN 00128252. doi: 10.1016/0012-8252(0)90030-Y.

A. A. Németh, S. J M H Hulscher, and R. M J Van Damme. Simulating offshore sand waves. *Coastal Engineering*, 53(2-3):265–275, 2006. ISSN 03783839. doi: 10.1016/j.coastaleng.2005.10.014.

Attila A. Németh, Suzanne J M H Hulscher, and Huib J. De Vriend. Modelling sand wave migration in shallow shelf seas. *Continental Shelf Research*, 22(18-19):2795–2806, 2002. ISSN 02784343. doi: 10.1016/S0278-4343(02)00127-9.

Peter Nielsen. *Some Basic Concepts of Wave Sediment Transport*. jan 1979.

Sanne Lina Niemann. *Modelling of sand dunes in steady and tidal flow*. Phd thesis, Technical University of Denmark (DTU), 2003.

K. W. Olesen. *Bed topography in shallow river bends*. PhD thesis, Delft University of Technology, 1987.

Steven A Orszag. On the Elimination of Aliasing in Finite-Difference Schemes by Filtering High-Wavenumber Components, 1971. ISSN 15200469.

Pieter C. Roos. Large-scale seabed dynamics in offshore morphology: Modeling human intervention. *Reviews of Geophysics*, 41(2), 2003. ISSN 8755-1209. doi: 10.1029/2002RG000120.

Pieter C Roos, Suzanne J M H Hulscher, Fenneke Van Der Meer, and Irene G M Wientjes. Grain size sorting over offshore sandwaves : Observations and modelling. *Built Environment*, (Hirano 1971):649–656, 2008.

Andreas Roulund, B. Mutlu Sumer, Jørgen Fredsøe, and Jess Michelsen. Numerical and experimental investigation of flow and scour around a circular pile. *Journal of Fluid Mechanics*, 2005. ISSN 0022-1120. doi: 10.1017/S0022112005004507.

I L Rozovskii. *Flow of water in bends of open channels.* Academy of Sciences of the Ukrainian SSR Israel Program for Scientific Translations];, Kiev; [Washington, D.C., available from the Office of Technical Services, U.S. Dept. of Commerce], 1961.

William Walden Rubey. Settling velocity of gravel, sand, and silt particles. *American Journal of Science*, Series 5 V(148):325–338, apr 1933. doi: 10.2475/ajs.s5-25.148.325.

James A. Schneider. Foundations of offshore wind turbine. URL `https://dosits.org/people-and-sound/examine-the-earth/how-is-sound-used-to-research-wind-energy/`.

Søren Løgstrup Sørensen. *Influence of offshore windfarms on the morphology of large scale bedforms.* Msc thesis, Technical University of Denmark (DTU), 2016.

R L Soulsby. *Dynamics of marine sands: a manual for practical applications.* Thomas Telford Ltd, 1997.

R.L. Soulsby and R.J.S Whitehouse. Threshold of sediment motion in coastal environments. *Proceedings Pacific Coasts and Ports 1997 Conference*, 1997.

A H Stride. *Offshore tidal sands: processes and deposits.* Routledge, Chapman & Hall, Incorporated, 1982. ISBN 9780412129704.

B Sumer and Jørgen Fredsøe. *The Mechanics of Scour in the Marine Environment*, volume 17. jan 2002. ISBN 981-02-4930-6. doi: 10.1142/4942.

B Mutlu Sumer and Jørgen Fredsøe. *Hydrodynamics Around Cylindrical Structures.* World Scientific Publishing Co Pte Ltd, 1997.

A.M. Talmon, N. Struiksma, and M.C.L.M. Van Mierlo. Laboratory measurements of the direction of sediment transport on transverse alluvial-bed slopes. *Journal of Hydraulic Research*, 33(4):495–517, 1995. ISSN 0022-1686. doi: 10.1080/00221689509498657.

S Tjerry. *Morphological calculation of dunes in alluvial rivers.* PhD thesis, Technical University of Denmark (DTU), 1995.

Marco Toffolon and Gianluca Vignoli. Suspended sediment concentration profiles in nonuniform flows: Is the classical perturbative approach suitable for depth-averaged closures? *Water Resources Research*, 43(4):1–19, 2007. ISSN 00431397. doi: 10.1029/2006WR005183.

Lloyd N Trefethen. Spectral Methods in Matlab. *Lloydia Cincinnati*, 10:184, 2000. ISSN 0586-7614. doi: 10.1137/1.9780898719598.

J. van den Berg, F. Sterlini, S. J M H Hulscher, and R. van Damme. Non-linear process based modelling of offshore sand waves. *Continental Shelf Research*, 37:26–35, 2012. ISSN 02784343. doi: 10.1016/j.csr.2012.01.012.

H. H. Van Der Veen, S. J M H Hulscher, and M. a F Knaapen. Grain size dependency in the occurrence of sand waves. *Ocean Dynamics*, 56(3-4):228–234, 2006. ISSN 16167341. doi: 10.1007/s10236-005-0049-7.

H. Henriët Van Der Veen and Suzanne M J H Hulscher. Predicting the occurrence of sand banks in the North Sea. *Ocean Dynamics*, 59(5):689–696, 2009. ISSN 16167341. doi: 10.1007/s10236-009-0204-7.

Henriëtte van der Veen, Suzanne J M H Hulscher, and Blanca Perez-Lapena. *Seabed morphodynamics due to offshore wind farms*, pages 1061–1066. Taylor & Francis, United Kingdom, 2007. ISBN 0-415-4536-3-1.

Leo C van Rijn. Sediment transport, part II: Suspended load transport. *Journal of Hydraulic Engineering*, 110(11):1613–1641, 1984a.

Leo C van Rijn. Sediment Transport, Part III: Bed forms and Alluvial Roughness, 1984b. ISSN 0733-9429.

Vattenfall. Horns Rev, a. URL `https://corporate.vattenfall.com/about-energy/renewable-energy-sources/wind-power/wind-power-at-vattenfall/horns-rev-3-offshore-wind-farm/`.

Vattenfall. Thanet wind farm airphoto, b. URL `https://corporate.vattenfall.co.uk/globalassets/uk/projects/thanet-ariel.jpg`.

M. Walgreen, D. Calvete, and H. E. De Swart. Growth of large-scale bed forms due to storm-driven and tidal currents: A model approach. *Continental Shelf Research*, 22(18-19):2777–2793, 2002. ISSN 02784343. doi: 10.1016/S0278-4343(02)00126-7.

J T F Zimmerman. Dynamics, diffusion and geomorphological significance of tidal residual eddies. *Nature*, 290(5807):549–555, apr 1981.

A. Julio Zyserman and Jørgen Fredsøe. Data analysis of bed concentration of suspended sediment. *Journal of Hydraulic Engineering*, 120(9):1021–1042, 1994.

DTU Mechanical Engineering
Section of Fluid Mechanics, Coastal and Maritime Engineering
Technical University of Denmark

Nils Koppels Allé, Bld. 403
DK-2800 Kgs. Lyngby
Denmark
Phone (+45) 4525 1360
Fax (+45) 4588 4325

www.mek.dtu.dk

DCAMM
Danish Center for Applied Mathematics and Mechanics

Nils Koppels Allé, Bld. 404
DK-2800 Kgs. Lyngby
Denmark
Phone (+45) 4525 4250
Fax (+45) 4593 1475
www.dcamm.dk
ISSN: 0903-1685